

AFIT/GAE/ENY/96D-8

EXPERIMENTAL INVESTIGATION  
OF TRANSVERSE SUPERSONIC  
GASEOUS INJECTION ENHANCEMENT  
INTO SUPERSONIC FLOW

THESIS

Mark P. Wilson, Captain, USAF

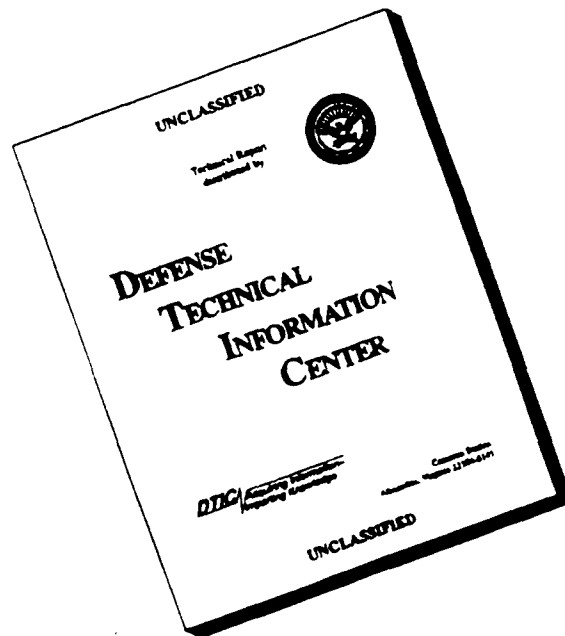
AFIT/GAE/ENY/96D-8

Approved for public release; distribution unlimited

19961203 024

DTIC QUALITY INSPECTED 4

# DISCLAIMER NOTICE



**THIS DOCUMENT IS BEST  
QUALITY AVAILABLE. THE  
COPY FURNISHED TO DTIC  
CONTAINED A SIGNIFICANT  
NUMBER OF PAGES WHICH DO  
NOT REPRODUCE LEGIBLY.**

Disclaimer Statement

The views expressed in this thesis are those of the author and do not reflect the official policy or position of the Department of Defense or the U.S. Government.

AFIT/GAE/ENY/96D-8

EXPERIMENTAL INVESTIGATION  
OF TRANSVERSE SUPERSONIC  
GASEOUS INJECTION ENHANCEMENT  
INTO SUPERSONIC FLOW

THESIS

Presented to the Faculty of the School of Engineering of the Air Force

Institute of Technology

Air University

In partial Fulfillment of the Requirements for the Degree of Master of

Science in Aeronautical Engineering

Mark P. Wilson, B.S.A.E.

Captain, USAF

December 1996

Approved for public release; distribution unlimited



### Acknowledgments

This work would not have been possible without the expert foresight and guidance of my thesis advisor, Dr. Rodney D. W. Bowersox. He provided ample expertise when needed, but also the freedom I required to conduct and arrive at my own conclusions during the course of this investigation.

The assistance of Dr. Sivram Gogeni and Dr. Diana Glawe in the setup and fine tune adjustment of the laser imaging system provided by WL/POPT was also indispensable. The science and art of laser flow visualization is non-trivial, yet the help of these two experts made realization of the images seem simple.

Considerable use of the expertise of the members of the newsgroup comp.sys.hp48 aided in the data reduction of this work. In particular the unparalleled programming knowledge of Mika Heiskanen, the file manipulation knowledge of John H. Meyers, and the excellent support of the other regular members enabled me to complete in hours what I would not have otherwise been able to do.

I would also like to thank the efforts of the reading committee. They suffered through the weighty drafts and the final copy; with their sage advice the readability of this document was substantially increased.

I dedicate this work to my family. My wife Michele bore the brunt of everything else that was not the thesis, and never failed to remind me when to work and when not to. My children, who saw more of the back of my head than the front, will hopefully benefit from the application of this research. Perhaps someday, they will recognize the term Mach Five as more than Speed Racer's car.

Mark Philipp Wilson

## Table of Contents

	Page
Acknowledgments .....	ii
List of Figures .....	vi
List of Tables .....	xi
List of Symbols .....	xii
Abstract .....	xiii
I. Introduction .....	1.1
1.1 Motivation .....	1.1
1.2 Background .....	1.2
1.3 Object and Scope of Present Study .....	1.2
1.4 PME Configuration and Rationale .....	1.3
1.5 Limitations of Present Study .....	1.6
1.6 Organization of Present Study .....	1.7
II. Background .....	2.1
2.1 Flow Fundamentals .....	2.1
2.2 Transverse Injection .....	2.3
2.3 Ramp and Aeroramp Injection .....	2.4
2.4 Vortex Mixing .....	2.6
2.5 Magnus Effect .....	2.8
2.6 Computational Investigations .....	2.8
2.7 Applications To Current Investigations .....	2.10
III. Facilities and Instrumentation .....	3.1
3.1 AFIT Mach Three Wind Tunnel .....	3.1
3.2 Transverse Injector Model .....	3.2
3.2.1 Tunnel coordinate System and Dimensions .....	3.2
3.2.2 Injector Model Modifications .....	3.3
3.2.3 Injection Parameters .....	3.4
3.3 PME Ramps .....	3.4
3.4 Measurement Locations .....	3.6
3.5 Mean Flow Probes .....	3.6
3.5.1 Pressure Probes .....	3.7
3.5.2 Probe Traverse System .....	3.7
3.6 Flow Visualization .....	3.7
3.6.1 Shadowgraph Photography Setup .....	3.7
3.6.2 Rayleigh-Mie Scattering Laser System .....	3.8
3.7 Data Acquisition System and Computational Resources .....	3.9
	Page
IV. Data Reduction and Processing .....	4.1

4.1	Mean Pressure Measurements	4.1
4.1.1	Determination of Flow Mach Number	4.1
4.1.2	Determination of Plume Static and Total Pressure	4.2
4.2	Total Pressure Loss	4.2
4.3	Plume Area and Penetration Determination	4.3
4.3.1	Freestream Mach Number Definition	4.4
4.3.1.1	Freestream Mach Number Definition I: Graphical Method	4.5
4.3.1.2	Freestream Mach Number Definition II: Box Method	4.7
4.3.1.3	Freestream Mach Number Definition II: Modified Box Method	4.8
4.3.2	Plume Area Determination	4.9
4.3.3	Plume Penetration Determination	4.10
4.4	Flow Visualization Techniques	4.10
4.4.1	Parallel Flow Orientation	4.10
4.4.1.1	Parallel Flow Orientation Analysis, Plume Trajectory Determination	4.12
4.4.1.2	Parallel Flow Orientation Analysis, Rate Of Centerline Decay	4.14
V.	PME Ramp Flow Field Results And Analysis	5.1
5.1	Simple Transverse Injector	5.2
5.1.1	Simple Transverse Injector Flow Visualization	5.2
5.1.1.1	Simple Transverse Injector Shadowgraph	5.2
5.1.1.2	Simple Transverse Injector Parallel Oriented Images	5.4
5.1.1.3	Simple Transverse Injector Cross Flow Images	5.6
5.1.2	Simple Transverse Injector Mach Contour Plots	5.8
5.1.3	Simple Transverse Injector Total Pressure Loss	5.10
5.1.4	Simple Transverse Injector Digital Image Quantitative Analysis	5.10
5.2	Injector Ramp Group #1: Symmetric Ramps	5.14
5.2.1	Symmetric Ramp Flow Visualization	5.14
5.2.1.1	Symmetric Ramp Shadowgraph Photography	5.14
5.2.1.2	Symmetric Ramp Parallel Oriented Images	5.17
5.2.1.3	Symmetric Ramp Cross Flow Oriented Images	5.22
5.2.2	Symmetric Ramp Mach Contour Plots	5.25
5.2.3	Symmetric Ramp Total Pressure Loss	5.33
5.2.4	Symmetric Ramp Digital Image Quantitative Analysis	5.34
5.3	Injector Ramp Group #2: Extended Ramps	5.40
5.3.1	Extended Ramp Flow Visualization	5.40
5.3.1.1	Extended Ramp Shadowgraph Photography	5.40
5.3.1.2	Extended Ramp Parallel Oriented Images	5.44
5.3.1.3	Extended Ramp Cross Flow Oriented Images	5.49
5.3.2	Extended Ramp Mach Contour Plots	5.52
5.3.3	Extended Ramp Total Pressure Loss	5.60
5.3.4	Extended Ramp Digital Image Quantitative Analysis	5.60
5.4	Injector Ramp Group #3: Asymmetric Ramps	5.65
5.4.1	Asymmetric Ramp Flow Visualization	5.65
5.4.1.1	Asymmetric Ramp Shadowgraph Photography	5.65
5.4.1.2	Asymmetric Ramp Parallel Oriented Images	5.67
5.4.1.3	Asymmetric Ramp Cross Flow Oriented Images	5.72
5.4.2	Asymmetric Ramp Mach Contour Plots	5.74
		Page
5.4.3	Asymmetric Ramp Total Pressure Loss	5.79
5.4.4	Asymmetric Ramp Digital Image Quantitative Analysis	5.80
5.5	Summary of Results	5.84
5.5.1	Total Pressure Loss Evaluations	5.84

5.5.2 Mean Flow Data Based Evaluations .....	5.84
5.5.3 Digital Image Data Based Evaluations.....	5.87
VI. Conclusions and Recommendations .....	6.1
6.1 Conclusions .....	6.1
6.2 Recommendations .....	6.1
Appendix A: Total Pressure Contour Plots.....	A.1
Appendix B: Instantaneous Cross Flow Oriented Images .....	B.1
Appendix C: Uncertainty Analysis .....	C.1
Bibliography.....	R.1
Vita .....	V.1

## List of Figures

Figure	Page
1.1. Symmetric Ramp Models SR 1, SR 2 and SR 3 . . . . .	1.4
1.2. Extended Ramp Models ER 1, ER 2 and ER 3 . . . . .	1.4
1.3. Asymmetric Ramp Models AR 1 And AR 2 . . . . .	1.4
2.1. Time-Averaged Example Injection Shadowgraph . . . . .	2.2
2.2. Typical Low Wedge Angle Swept Ramp . . . . .	2.5
3.1. Tunnel Coordinate System . . . . .	3.2
3.2. Side View of Test Section. . . . .	3.3
3.3. Symmetric PME Ramps . . . . .	3.5
3.4. Extended PME Ramps . . . . .	3.5
3.5. Asymmetric PME Ramps . . . . .	3.6
3.6. Rayleigh-Mie Scattering Laser and CCD System . . . . .	3.8
4.1. Simple Transverse Injector Mach Contour Plot With Plume Search Region . . . . .	4.4
4.2. Graphical Method Local Freestream Search Region . . . . .	4.6
4.3. Box Method Local Freestream Search Region . . . . .	4.7
4.4. Instantaneous Digital image, Model 1 . . . . .	4.11
4.5. Averaged Digital Image, Model 1 . . . . .	4.11
4.6. Plume Image Measurement Stations . . . . .	4.12
4.7. Seed Condensation On Ramp Injector Model . . . . .	4.13
5.1. Simple Transverse Injector Composite Shadowgraph . . . . .	5.2
5.2. Simple Transverse Injector, Instantaneous Parallel Oriented Laser Image . . . . .	5.4
5.3. Simple Transverse Injector, Time-Averaged Parallel Oriented Laser Image . . . . .	5.5
5.4. Simple Transverse Injector, Instantaneous Cross Flow Image . . . . .	5.6
5.5. Simple Transverse Injector, Time-Averaged Image Cross Flow Oriented Image . . . . .	5.7
	Page

5.6. Simple Transverse Injection Mach Contour Plot . . . . .	5.8
5.7. Simple Transverse Injection Area Contour Plot. . . . .	5.9
5.8. Simple Transverse Injector Plume Centerline Trajectory . . . . .	5.11
5.9. Simple Transverse Injector Plume Centerline Average Intensity Decay . . . . .	5.12
5.10. Double Diamond Ramp SR 1 Composite Shadowgraph. . . . .	5.14
5.11. Double Cone Ramp SR 2 Composite Shadowgraph. . . . .	5.15
5.12. Double Ramp SR 3 Composite Shadowgraph . . . . .	5.16
5.13. Double Diamond Ramp SR 1, Instantaneous Parallel Oriented Laser Image . . . . .	5.17
5.14. Double Diamond Ramp SR 1, Time-Averaged Parallel Oriented Laser Image . . . . .	5.18
5.15. Double Cone Ramp SR 2, Instantaneous Parallel Oriented Laser Image . . . . .	5.19
5.16. Double Cone Ramp SR 2, Time-Averaged Parallel Oriented Laser Image. . . . .	5.20
5.17. Double Ramp SR 3, Instantaneous Parallel Oriented Laser Image. . . . .	5.20
5.18. Double Ramp SR 3, Time-Averaged Parallel Oriented Laser Image . . . . .	5.21
5.19. Double Diamond Ramp SR 1, Time-Averaged Cross Flow Oriented Laser Image . . . . .	5.22
5.20. Double Cone Ramp SR 2, Time-Averaged Cross Flow Oriented Laser Image . . . . .	5.23
5.21. Double Ramp SR 3, Time-Averaged Cross Flow Oriented Laser Image . . . . .	5.24
5.22. Double Diamond Ramp SR 1 Mach Contour Plot . . . . .	5.25
5.23. Double Diamond Ramp SR 1 Area Contour Plot. . . . .	5.26
5.24. Double Cone Ramp SR 2 Mach Contour Plot . . . . .	5.28
5.25. Double Cone Ramp SR 2 Area Contour Plot. . . . .	5.29
5.26. Double Ramp SR 3 Mach Contour Plot . . . . .	5.31
5.27. Double Ramp SR 3 Area Contour Plot . . . . .	5.32
5.28. Double Diamond Ramp SR 1 Plume Centerline Trajectory . . . . .	5.34
5.29. Double Diamond Ramp SR 1 Plume Centerline Average Intensity Decay . . . . .	5.35

	Page
5.30. Double Cone Ramp SR 2 Plume Centerline Trajectory . . . . .	5.36
5.31. Double Cone Ramp SR 2 Plume Centerline Average Intensity Decay . . . . .	5.37
5.32. Double Ramp SR 3 Plume Centerline Trajectory. . . . .	5.38
5.33. Double Ramp SR 3 Plume Centerline Average Intensity Decay . . . . .	5.39
5.34. Extended Diamond Ramp ER 1 Composite Shadowgraph . . . . .	5.40
5.35. Truncated Extended Ramp ER 2 Composite Shadowgraph . . . . .	5.42
5.36. Tapered Extended Ramp ER 3 Composite Shadowgraph . . . . .	5.43
5.37. Extended Diamond Ramp ER 1, Instantaneous Parallel Oriented Laser Image . . . . .	5.44
5.38. Extended Diamond Ramp ER 1, Time-Averaged Parallel Oriented Laser Image . . . . .	5.44
5.39. Truncated Extended Ramp ER 2, Instantaneous Parallel Oriented Laser Image . . . . .	5.45
5.40. Truncated Extended Ramp ER 2, Time-Averaged Parallel Oriented Laser Image . . . . .	5.46
5.41. Tapered Extended Ramp ER 3, Instantaneous Parallel Oriented Laser Image . . . . .	5.47
5.42. Tapered Extended Ramp ER 3, Time-Averaged Parallel Oriented Laser Image . . . . .	5.48
5.43. Extended Diamond Ramp ER 1, Time-Averaged Cross Flow Oriented Laser Image . . . . .	5.49
5.44. Truncated Extended Ramp ER 2, Time-Averaged Cross Flow Oriented Laser Image . . . . .	5.50
5.45. Tapered Extended Ramp ER 3, Time-Averaged Cross Flow Oriented Laser Image . . . . .	5.51
5.46. Extended Diamond Ramp ER 1 Mach Contour Plot . . . . .	5.52
5.47. Truncated Extended Cone Ramp ER 2 Mach Contour Plot. . . . .	5.54
5.48. Truncated Extended Cone Ramp ER 2 Area Contour Plot . . . . .	5.55
5.49. Tapered Extended Ramp ER 3 Mach Contour Plot . . . . .	5.57
5.50. Tapered Extended Ramp ER 3 Area Contour Plot . . . . .	5.58
5.51. Truncated Extended Ramp ER 2 Plume Centerline Trajectory. . . . .	5.61
5.52. Truncated Extended Ramp ER 2 Plume Centerline Average Intensity Decay . . . . .	5.62
5.53. Tapered Extended Ramp ER 3 Plume Centerline Trajectory. . . . .	5.63

	Page
5.54. Tapered Extended Ramp ER 3 Plume Centerline Average Intensity Decay . . . . .	5.64
5.55. Wide Ramp AR 2 Composite Shadowgraph . . . . .	5.65
5.56. Narrow Ramp AR 3 Composite Shadowgraph . . . . .	5.66
5.57. Wide Ramp AR 2, Instantaneous Parallel Oriented Laser Image. . . . .	5.67
5.58. Wide Ramp AR 2, Time-Averaged Parallel Oriented Laser Image . . . . .	5.68
5.59. Narrow Ramp AR 3, Instantaneous Parallel Oriented Laser Image . . . . .	5.70
5.60. Narrow Ramp AR 3, Time-Averaged Parallel Oriented Laser Image . . . . .	5.70
5.61. Wide Ramp AR 2, Time-Averaged Cross Flow Oriented Laser Image . . . . .	5.72
5.62. Narrow Ramp AR 3, Time-Averaged Cross Flow Oriented Laser Image. . . . .	5.73
5.63. Wide Ramp AR 2 Mach Contour Plot . . . . .	5.74
5.64. Wide Ramp AR 2 Area Contour Plot . . . . .	5.76
5.65. Narrow Ramp AR 3 Mach Contour Plot. . . . .	5.77
5.66. Narrow Ramp AR 3 Area Contour Plot . . . . .	5.78
5.67. Wide Ramp AR 2 Plume Centerline Trajectory. . . . .	5.80
5.68. Wide Ramp AR 2 Plume Centerline Average Intensity Decay . . . . .	5.81
5.69. Narrow Ramp AR 3 Plume Centerline Trajectory . . . . .	5.82
5.70. Narrow Ramp AR 3 Plume Centerline Average Intensity Decay. . . . .	5.83
5.71. Normalized Average Plume Area vs. $\Pi$ . . . . .	5.85
5.72. Normalized Average Plume Centroid vs. $\Pi$ . . . . .	5.85
5.73. Normalized Average Plume Centerline Trajectory vs. $\Pi$ . . . . .	5.87
5.74. Normalized Average Plume Intensity Decay Rate vs. $\Pi$ . . . . .	5.88
A.1. Simple Transverse Injection . . . . .	A.1
A.2. Double Diamond Ramp SR 1 . . . . .	A.1
A.3. Double Cone Ramp SR 2 . . . . .	A.1



	Page
A.4. Double Ramp SR 3 .....	A.1
A.5. Truncated Extended Ramp ER 2.....	A.2
A.6. Tapered Extended Ramp ER 3 .....	A.2
A.7. Wide Ramp AR 1 .....	A.2
A.8. Narrow Ramp AR 2.....	A.2
A.9. Test Section, No Injection or PME Ramp .....	A.2
B.1. Simple Transverse Injection .....	B.1
B.2. Double Diamond Ramp SR 1 .....	B.1
B.3. Double Cone Ramp SR 2 .....	B.1
B.4. Double Ramp SR 3 .....	B.1
B.5. Extended Diamond Ramp ER 1 .....	B.2
B.6. Truncated Extended Ramp ER 2.....	B.2
B.7. Tapered Extended Ramp ER 3 .....	B.2
B.8. Wide Ramp AR 1 .....	B.2
B.9. Narrow Ramp AR 2.....	B.2

### List of Tables

Table	Page
3.1. Wind Tunnel and Injector Nozzle Exit Dimensions . . . . .	3.2
3.2. Freestream Flow Conditions . . . . .	3.3
3.3. Injector Jet Flow Conditions . . . . .	3.4
5.1. Simple Transverse Injector Area and Centroid Results . . . . .	5.10
5.2. Double Diamond Ramp Area and Centroid Results . . . . .	5.27
5.3. Double Cone Ramp Area and Centroid Results . . . . .	5.29
5.4. Double Ramp Area and Centroid Results . . . . .	5.33
5.5. Symmetric Ramp Group Total Pressure Loss . . . . .	5.33
5.6. Truncated Extended Ramp Area and Centroid Results . . . . .	5.56
5.7. Tapered Extended Ramp Area and Centroid Results . . . . .	5.59
5.8. Extended Ramp Group Total Pressure Loss . . . . .	5.60
5.9. Wide Ramp Area and Centroid Results . . . . .	5.76
5.10. Narrow Ramp Area and Centroid Results . . . . .	5.79
5.11. Asymmetric Ramp Group Total Pressure Loss . . . . .	5.79
5.12. Injector Total Pressure Loss Ratio, $\Pi$ . . . . .	5.84
C.1. Uncertainties in Calculations . . . . .	C.2

### List of Symbols

A	- Area, cm <sup>2</sup>
a	- Speed of sound, m/s
d	- Injector nozzle exit minor diameter, mm
M	- Mach number
P, p	- Pressure, Pa
$\bar{q}$	- Dynamic pressure ratio, $(\rho u^2)_j/(\rho u^2)_\infty$
q	- Turbulent transport variable
T	- Temperature, K
u, V	- Velocity, m/s
x	- Streamwise tunnel coordinate
y	- Vertical tunnel coordinate
z	- Horizontal tunnel coordinate

### Greek

$\delta$	- Boundary layer thickness, cm
$\varepsilon$	- Uncertainty
$\gamma$	- Ratio of specific heats
$\lambda$	- Mass Flux Ratio, $(\rho u)_j/(\rho u)_\infty$
$\Pi$	- Total pressure ratio
$\rho$	- Density, kg/m <sup>3</sup>
$\omega$	- Turbulent transport variable
$\chi$	- Species concentration, mole/m <sup>3</sup>

### Subscripts

0	- Upstream property
1	- Local property
2	- Pitot probe property
c	- Cone-static
eb	- Effective back
t	- Total property

Abstract

In pursuit of more efficient and effective fuel-air mixing for a SCRAMJET combustor, this study was conducted to investigate relative near field enhancements of penetration and mixing of a discrete low-angled ( $25^\circ$ ) injected air jet into a supersonic ( $M=2.9$ ) cross flow. The enhancements were achieved by injecting the transverse air jet parallel to the compression face of eight different ramp geometries. The jet-ramp interactions created collinear shock structures, baroclinic torque vorticity enhancement, ramp spillage enhanced vorticity, magnus effect penetration enhancement, and increased total pressure loss. Shadowgraph photography was used to identify the shock structures and interactions in the flow field. Measurements of mean flow properties were used to establish the jet plume size, jet plume penetration and to quantify the total pressure loss created by the ramps. Rayleigh-Mie scattering images were used for both qualitative flow field assessments and quantitative analysis of the plume trajectory and mixing rate. Results indicate that up to a 20% increase in penetration height and plume expansion can be achieved by injection over a ramp compared to simple transverse injection. This increase in penetration and mixing incurs up to a 15% loss in total pressure. The most critical geometric aspects that affect the flow are the ramp compression face shape and frontal aspect, and the location and strength of ramp generated expansion.

# ***I. Introduction***

## ***1.1 Motivation***

A plateau has been reached in the realm of air-breathing propulsion. Despite the explosive growth and technological progression seen during the last century<sup>1,2</sup>, the state of the art has been stalled for the last thirty years. The cause of this tailing off of the "higher and faster" progression is that current air-breathing propulsion systems have been pushed to the material and chemical limits they can withstand. This limit in speed is in the sub-hypersonic regime, or below Mach 6. Currently the fastest known air-breathing manned aircraft is the SR-71, capable of speeds in excess of Mach 3. The ramjet powered D-21 unmanned reconnaissance drone, which was launched from the SR-71, was capable of speeds in excess of Mach 5. Both of these designs are products of the late 1950s, and were the cutting edge of material and aerodynamic science for their time. As a result of the National Aerospace Plane program and other related projects, a renaissance of hypersonic research is now underway. The end of the hiatus in high speed research has again hit the same material and aerodynamic limits of the 1950's; in order to again reach "higher and faster" a different method of propulsion must be employed than the current turbojet or ramjet approach. This method will most likely involve combustion in flows at supersonic speeds as well as ram or body compression, or a SCRAMjet engine.

Issues preventing the realization of hypersonic air-breathing propulsion are as real now as the control and structure issues faced in the late 1940s, during the breaking of the sound barrier. The option of slowing the hypersonic freestream flow to subsonic speeds for combustion as in a turbojet or ramjet is not physically feasible. A simple example demonstrates this; at 30 km altitude and a relatively low hypersonic flight speed of Mach 8, the stagnation temperature will easily exceed 3100° K. The extremely high stagnation temperature for ambient air at the proposed flight conditions will incinerate all metals and most other materials suitable for airframe structures. Additionally, the fuel combustion products would dissociate at these high temperatures, thus offsetting most of the heat released during combustion. If the flow could be slowed by the vehicle's bow shock and inlet shocks to Mach 2 through the combustor, the still high but more manageable static temperature would be approximately 1900° K. The problem now becomes how to manage efficient and effective mixing and burning of fuel for the extremely short residence time the working fluid will have in the combustor.

## **1.2 Background**

Several schemes have been employed during the last thirty years to enhance the penetration and mixing of an injected plume into supersonic freestream conditions. Initial studies were conducted to examine the effect and governing conditions for normally injected underexpanded jets.<sup>3,4</sup> These earlier works provided fundamental analysis of the structures associated with transverse injection and laid the groundwork for the initial computational approaches. Vorticity generated by the pressure differential across the front to rear face of the emerging jet was identified as a major near-field mixing factor.<sup>5,6</sup> While work has continued in transverse injection,<sup>7,8,9</sup> later studies sought to produce greater vorticity while retaining the jet momentum in the direction of thrust through low angle injection from the rear face of injector ramps.<sup>2,10,11,13,14</sup> These ramp configurations were intended to generate vorticity from the spillage of high pressure air off and around the leading compression surface. A further refinement recently tested was the aero-ramp concept of Fuller et al. This concept employed multiple injection ports arranged in the planform of a physical ramp to create vorticity with lower shock losses than the physical ramp would cause.<sup>10</sup> Other investigations have explored the effects of a shock wave passing through a vortex plume and how the pressure differential of the shock across the plume cross section produces the baroclinic torque mechanism<sup>6</sup> which has been shown to enhance vorticity.

## **1.3 Object and Scope of Present Study**

The primary objective of this study is to increase the near-field penetration and mixing of a fuel plume into a SCRAMjet combustor. This is accomplished by examination of the relative near-field enhancement of penetration and mixing of a Mach 1.87 underexpanded supersonic air jet transversely injected at 25° into a nominally Mach 2.9 air freestream. The enhancement is achieved by placing a penetration and mixing enhancement (PME) ramp immediately downstream of the injection port; eight dissimilar geometries of PME ramps were investigated. This injection scheme was devised to capitalize on the better near-field mixing of transverse injection and the superior far-field mixing of ramp generated vorticity. Several additional benefits can be realized from this injection arrangement. Pressure losses of the PME ramp should be minimal since the compression face is parallel to the angle of injection. Any resulting shocks from the PME ramp should be relatively weak. Near field mixing could be increased without adversely affecting penetration by exploiting the baroclinic torque from the weak PME ramp

shock. The solid boundary of the PME ramp compression face should also delay the turning of the plume. This would enhance penetration, as well as increase the vertical height the freestream would be able to add vorticity to the plume. Additionally, the solid boundaries and the plume vortex pair should couple to increase penetration via the magnus effect. In high enthalpy flows, this injection scheme could also provide effective film cooling for injection ramps which otherwise might not survive the ambient conditions.<sup>15</sup>

The relative measure of penetration and mixing enhancement was attained by normalizing the results of the eight individual PME ramp models with the results of injection over a flat wall, or simple transverse injection. Measurements of mean flow properties were used to establish the extent of penetration and to indirectly determine the extent of mixing produced by the PME ramp models. Digital processing Rayleigh-Mie scattering images of the flow were used to directly measure the jet plume size and to establish a means of determining the rate of plume centerline concentration decay with downstream position based upon injectant seed concentrations.

#### ***1.4 PME Configurations and Rationale***

The eight PME ramp models, Figures 1.1 to 1.3, can be grouped into three distinct groups with similar geometric features. The ramp models are shown in top view, with the flow direction from bottom to top. See section 3.3 for complete dimensionality. The models were oriented with the leading 25° inclined face directly behind the rear lip of the injector nozzle exit port.

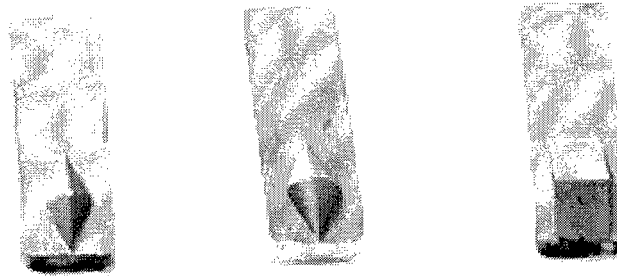


Figure 1.1: Symmetric Ramp Models SR 1, SR 2 and SR 3

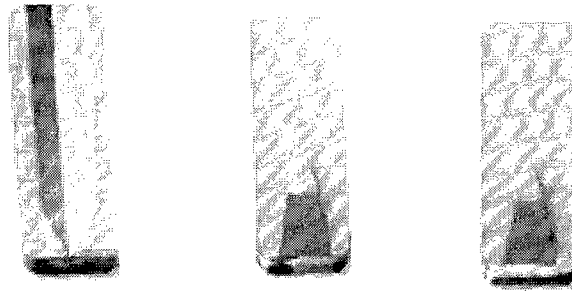


Figure 1.2: Extended Ramp Models ER 1, ER 2 and ER 3

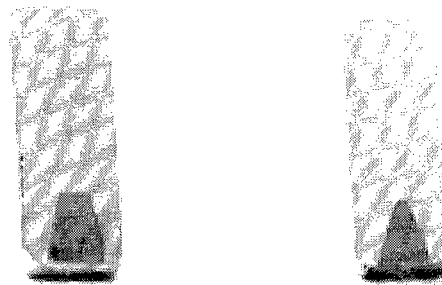


Figure 1.3: Asymmetric Ramp Models AR 1 And AR 2

The first group is the Symmetric Ramp (SR) injectors, which are symmetric about the y-z plane of the tunnel coordinate system. Models SR 1, SR 2 and SR 3 belong to this group. Each model in this group has a rising compression surface the plume is expected to interact and lift off from, and a trailing expansion surface to accelerate the flow behind the ramp. The models have varying degrees of three-dimensional relieving effects on the model induced shock wave.<sup>10</sup> For example, at one end of the spectrum is the model SR 3 compression surface which is a flat plate to induce a two-dimensional shock. At the other extreme the model SR 2 compression surface is a half cone extending from the tunnel ceiling, which in the near vicinity of the expanding plume should have a greater three-dimensional relieving effect on the model induced shock wave. Model SR 1 is a compromise between the two, having a three-dimensional but faceted compression surface.

The second group is the Extended Ramp models. Models ER 1, ER 2 and ER 3 belong to this group. These models have an extension that is parallel to the test section ceiling behind the rising compression surface. The purpose of the extension is twofold. It provides an additional surface for the magnus effect to lift the plume further into the freestream. Additionally, the extension decreases the



strength of the expansion around the top of the model to the rear face. There are four reasons to minimize the flow expansion. First, the expansion accelerates the plume which in turn reduces the residence time the fuel plume and freestream air have to mix and combust. Second, the extension provides a physical barrier that prevents the plume from turning back toward the tunnel ceiling. Third, minimizing the expansion reduces the pressure loss through the recompression shock. Fourth, strong expansions can stabilize the flow (i. e., decrease the magnitude of turbulent fluctuations) which would reduce the mixing. The extensions used were intended to test two additional mechanisms to enhance penetration and mixing. Model ER 3 is a tapered wedge that when extended to the end of the model meets at a point. The anticipated effect is that the flow traveling along the sides of the ramp will experience a smooth transition upon rejoining the freestream to minimize pressure losses. Strong shock waves are not expected, since the model is about the height of the boundary layer. Model ER 2 is slightly less tapered than model ER 3 but of the same length. This terminates the extension as a truncated triangle when viewed from above. This truncated geometry is expected to provide a recirculation region that would be suitable for either flame holding or additional jet injection. Model ER 1 is an exaggerated extended surface used to determine what effect if any longer extensions would have on the plume. Model ER 1 was included mainly for qualitative analysis, as the scaling is not representative of the other models.

The third group consists of models AR 1 and AR 2. These PME ramp models are simple asymmetric tapered wedges. The only difference between the two models is the taper ratio. Model AR 1 tapers from  $4d$  to  $2d$  at the top of the compression surface. Model AR 2 tapers from  $4d$  to  $1d$  at the top of the compression surface. The primary mixing mechanism associated with these types of ramps is vorticity generated by spillage from the high pressure compression surface to the lower pressure side and rear faces.<sup>10</sup> The degree of sweep in a ramp has been shown to affect mixing and combustion efficiency, with unswept ramps generally performing poorer than the swept ramps.<sup>16</sup> The freestream pressure-induced vorticity will be limited by the presence of the plume, which will deflect the freestream away from the compression surface. However, the plume itself will become the high pressure mechanism to induce additional vorticity and freestream entrainment for mixing.

### ***1.5 Limitations of Present Study***

Limitations of this study include availability of facilities, the use of similar, uncombusted gas injectant and freestream, number of downstream locations sampled and available data. A time constraint imposed on the use of shared experimental resources, as well as the number of PME ramp models investigated, limited the mean flow measurements to one axial station downstream of the injection site. The facilities used at the time of this study were incapable of either combustion or measuring the species concentration of a binary gas. This study is limited to pressure data and image data, and provides no direct measure of mixing enhancement features such as relative strengths of the vorticity the ramp models may produce. The limitation in downstream test locations is overcome in two manners. First, the laser plane imaging captures the plume development and interactions with the PME ramp models up to the mean flow measurement location. Second, the fuel plume under the proposed flight conditions of a hypersonic vehicle will most likely combust in the near-field due to the extreme high temperatures to be expected in the flow.<sup>17</sup> Once combustion occurs the mechanisms governing the plume size, shape and concentrations become drastically different from the mechanisms studied here. The similar gas injection limitation was partially overcome by normalizing the results; a comparable order enhancement of hydrogen fuel injection may be expected for injection over a similar geometry as investigated here. The limitations on the data collected affect the understanding of the detail mechanisms acting in the flow. However, this study is primarily an observation of macroscopic effects. A comparison of a diverse set of PME ramp model performance trends can establish what geometric features appear to enhance overall mixing. After such large scale observations, detailed investigations for further research and optimization will be merited.

## ***1.6 Organization of Present Study***

The remainder of this investigation is organized into five additional chapters. The second chapter provides a detailed review of previous research into supersonic injection schemes. Topics reviewed are presented in the following order. Basic mechanisms of transverse injection normal and to an angle with the main flow are explained. Other schemes, including ramp injection and aeroramp injections, are presented. The role of vorticity as a means of mixing an injectant plume and freestream are explored. An analysis of the current state of computational fluid dynamics and supersonic injection problems is given. The results of earlier works that are expected to be exploited in this investigation are analyzed. The third chapter describes the experimental setup used. The mean flow pressure probe and the laser imaging systems are

depicted. The fourth chapter explains the data reduction and analysis techniques employed to derive the results. This chapter includes the analytical methods used to determine the plume properties of area and penetration from both the pressure probe and laser imaging data. Chapter Five presents the results of this investigation. Analysis of the data and comparisons to previous research are given. A summary of the results concludes this chapter. Finally, the sixth chapter details conclusions as to the effectiveness of and penalties incurred by injection over a ramp in enhancing mixing and penetration into supersonic cross flow. Recommendations for future research are submitted.

## ***II. Background***

A considerable wealth of both experimental and computational research has been conducted in the study of transverse supersonic injection and supersonic injection behind a ramp. This chapter is a review of the fundamental concepts and results from past investigations, and development of how they are applied to the current investigation. The topics covered are flow and injection fundamentals, transverse injection, ramp and aeroramp investigations, vorticity generation, the magnus effect and computational efforts. The chapter concludes by relating the earlier works as a foundation for the desired results of this experiment.

### ***2.1 Flow Fundamentals***

In an effort to provide a basis of comparison between studies under diverse conditions, several injection parameters and flow variables have been established. The injection parameters include injector-to-freestream ratios such as the velocity ratio, mass flux ratio and expansion ratio.<sup>18</sup> An additional injector-to-freestream ratio to consider is the dynamic pressure ratio  $\bar{q}$ , also known as the momentum flux ratio. Where ramps are involved, a standard set of geometric parameters arise such as the ramp dimension to injector port diameter ratios, the ramp wedge angle and the degree of sweep of the ramp vertical sides. The primary flow variables of concern for this type of study are the injector diameter based Reynolds number, the boundary layer depth to injector diameter ratio  $\frac{\delta}{d}$ , and the flow total properties.

With the exception of expansion ratio, these injection parameters and flow properties are relatively straightforward. The expansion ratio is the ratio of the jet exit pressure and effective back pressure  $p_{eb}$  as put forth by Schetz and Billig.<sup>4</sup> Effective back pressure is a means of estimating the pressure to which a jet will expand from the similarities between cross flow injection and injection into a quiescent medium.<sup>3</sup> Effective back pressure was originally treated as a simple proportionality to either the pressure behind a the plume bow shock or the pressure in the separated zone ahead of the injection port depending on the  $\frac{\delta}{d}$  value, and was limited to normal injections.<sup>4</sup> This concept has evolved to more advanced models, including one for injection at an angle. The newer model for  $p_{eb}$  treats it as an average of the approach flow static pressure and the Newtonian impact theory for pressure on inclined bodies.<sup>19</sup>

The inclination angles used in this approach are based upon the injection geometry and injection Mach disk, described below.

Injection of an underexpanded sonic or supersonic jet into a supersonic freestream produces several flow structures. The first of these is a bow shock produced as the freestream impacts the injection streamtube; in this respect the injectant acts as a solid cylindrical body.<sup>5</sup> For injector geometries where  $\frac{\delta}{d}$  is on the order of one or more, a separation bubble can form slightly upstream of the injector port.<sup>4,5</sup> The separation bubble results in a lambda shock formation through the boundary layer.<sup>20</sup> After entering the freestream, the jet experiences a rapid Prandtl-Meyer expansion (usually assumed to be an isentropic process) surrounded by a barrel shock.<sup>9</sup> A normal shock (i.e., normal to the jet path) known as the Mach disk terminates the barrel shock, and recompresses the flow to  $p_{eb}$ . Before the Mach disk, the injectant and freestream are typically treated as separate entities; afterwards vorticity and other turbulent mechanisms induce large scale mixing. Figure 2.1 depicts a time-averaged shadowgraph of an injection at 25° with the generic injection related structures identified.

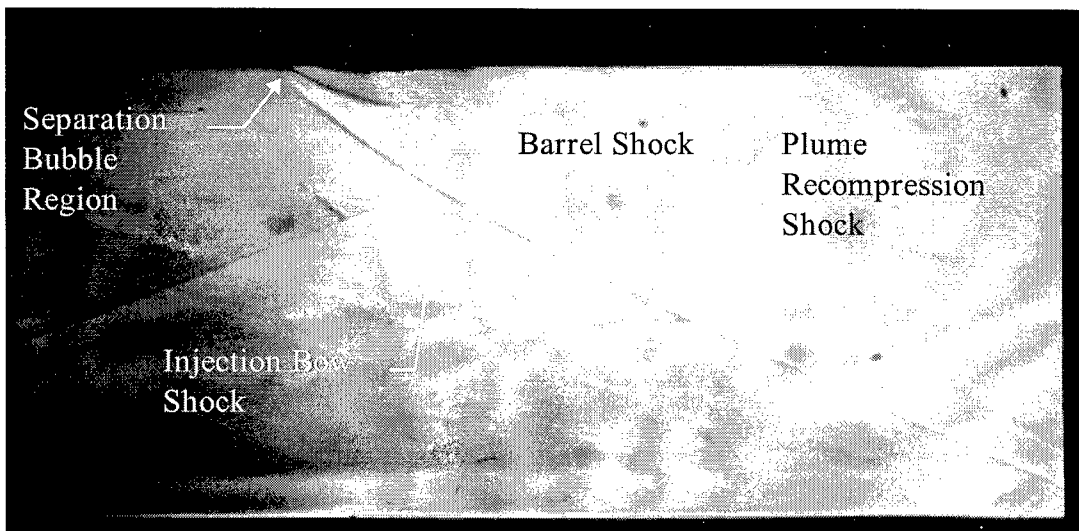


Figure 2.1: Time-Averaged Example Injection Shadowgraph

With the basic framework of underexpanded jet injection structures and terminology put forth, discussion of the various injection schemes can ensue. The mechanics and structures of each type of injection is discussed and related to the basic theory of injection described above. The relative strengths and weaknesses of each method are also presented.

## **2.2 Transverse Injection**

Transverse injection of an underexpanded jet into supersonic flow has been well documented over the last thirty years. Transverse injection is arguably the simplest injection configuration, requiring only an injection port (sonic or supersonic) at the desired injection angle, usually normal to the plane of the injection wall and parallel with the direction of flow. In either normal or angled injection, the entry of the injectant jet into the mainstream flow can be regarded as a two stage process.<sup>4</sup> The jet first enters the main flow and remains relatively intact as it expands to the height of the Mach disk. Beyond the Mach disk, the flow turns and accelerates with the main flow. In the second stage, the jet acts as a coaxial vortex mixing structure.

In the near field, the injection parameter  $\bar{q}$  has been shown to strongly impact mixing and affect penetration. For mixing, the initial rate of mixing is proportional to  $\frac{1}{\bar{q}}$ .<sup>18</sup> This can be interpreted from continuity and momentum principles. As the dynamic pressure of the injectant is increased, it would initially enter the freestream either faster ( $\rho_j$  constant) or denser ( $V_j$  constant). In the first case, the injectant jet itself would reduce the residence time it has to mix with the local freestream. In the second, the jet would present a more solid obstacle to the flow, requiring greater time and hence distance to disperse. In the far field,  $\bar{q}$  has been shown to have little impact on mixing rates.<sup>13,18</sup> A benefit from increasing  $\bar{q}$  for low injection angles is a decrease in total pressure loss from the added streamwise component of jet momentum.<sup>13</sup> Penetration is enhanced with increasing  $\bar{q}$  in that the Mach disk is pushed further out into the freestream; however, the plume then turns more sharply with the main flow.<sup>4</sup> This effect was seen to diminish with increasing  $\bar{q}$ .<sup>4</sup>

The effect of the injection angle on near field injectant jet penetration and mixing has received surprisingly little attention to date. However, the available far field results are insightful. In the far field, mixing rates are related by the injectant decay of maximum concentration proportionality

$$\chi_{\max} \propto \left(\frac{x}{d}\right)^{-n} \quad (2.1)$$

where the exponent  $n$  can be used for mixing comparisons.<sup>5</sup> On a Log-Log plot of maximum concentration decay with downstream location  $n$  is the slope of the maximum concentration decay line. As the angle of injection is increased, holding all other flow variables and injection parameters constant, far field mixing rates increase.<sup>18</sup> In conjunction with the far field mixing increase, there is an increased bow shock strength and total pressure loss.<sup>18</sup> A parametric mixing/total pressure loss trade-off study would be required to determine the optimum injection angle, which would most likely be Mach number dependent (due to decreased residence time with increased Mach number). Further, low angle injection has been shown to create a measurable increase in the overall combustion thrust potential<sup>6,21</sup> which intuitively would not be as great with normal or higher angle injection.

### ***2.3 Ramp and Aeroramp Injection***

Ramp injection has also received considerable attention in published research. Two benefits are realized by injecting through a ramp. First, the ramp provides significant vortex generation (described in detail in section 2.5) for mixing and penetration of the injectant jet. Second, the rear surface of a ramp is a relatively slow moving recirculation zone, which would be ideal as a flame holder in a combustor. The ramp geometries explored so far have relatively low wedge angles, ranging from 9.5° to 10.3°,<sup>10,11,12,13,16</sup> with a right triangle side profile, the 90° angle being opposite to the wall. The injectant jet usually exits normal to the rear face at the wedge angle. Figure 2.2 shows a typical ramp injection setup, with the direction of flow from top left to bottom right.

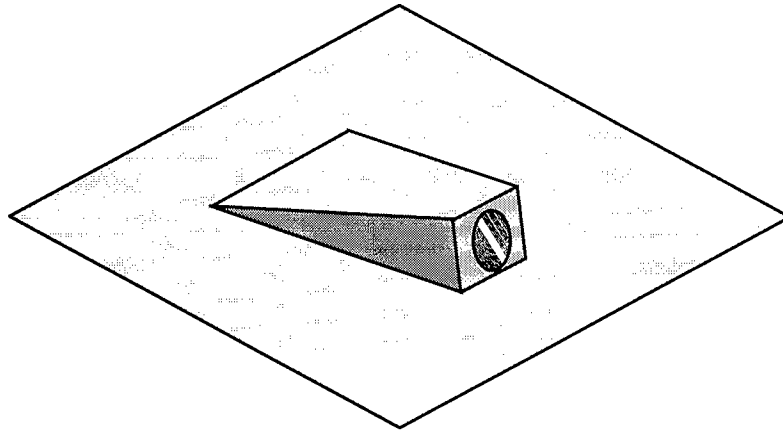


Figure 2.2: Typical Low Wedge Angle Swept Ramp

Once injected, the jet does not behave exactly as a transverse jet would. Though the generic underexpanded jet structures described in section 2.2 are present, there are additional ramp base effects, including multiple three-dimensional shocks and expansions, which impact the flow structure. Analytical results indicate dramatic decreases in circulation (based upon Stokes Law) from the base of the ramp and up to half a ramp length downstream due to ramp base effects and jet interactions.<sup>10</sup> This region of the flow is highly three-dimensional and turbulent; not all of the interactions and flow mechanics have been completely mapped or explained. Beyond the ramp base the plume becomes basically indistinguishable from a similar parameter low angle transverse injection (with the exception of the strength of the vortex rotation pair).

The aeroramp concept was put forth recently by Fuller et al.<sup>13</sup> The aeroramp is actually three rows and columns of staged and angled transverse injection ports in the planform of a swept ramp. The idea employed was that with proper multiaxis angling of the injector rows, a buildup of injectant would form in the profile of a ramp.<sup>13</sup> This concept has been demonstrated before, where the second jet in a tandem transverse arrangement was able to penetrate further into the freestream due to the partial shielding provided by the first transverse injectant plume.<sup>5</sup> By simulation of a solid ramp with gaseous injectant the total pressure losses in the flow field were noticeably reduced and increased at a slower rate with downstream location than the similar solid ramp.<sup>13</sup> Though penetration and mixing were reduced



with the aeroramp, a substantial gain in both measurands was obtained by doubling  $\bar{q}$  from 1.0 to 2.0<sup>8</sup>.

Full details of the injector geometries and similarity parameters can be found in reference 13.

## **2.4 Vortex Mixing**

Regardless of the injection scheme employed, vorticity is the driving mixing mechanism in the near field.<sup>5</sup> In transverse injection, streamwise vorticity is generated by two primary mechanisms. The first is the external pressure differential created across the front and rear faces of the emerging jet. The main flow must split around the injectant jet, creating high pressure regions on the front and partially on the side faces of the jet. The resulting low pressure on the rear or leeward side of the jet becomes an entrainment region for the local freestream. The flow bisection and downstream entrainment results in a counter-rotating vortex pair inside the largely circular injectant jet. A second source of vorticity is created as the plume is bent coaxially with the freestream. The bend accelerates the outer portion of the plume, decreasing the internal pressure. The inside region of the plume which is not as greatly accelerated is then drawn into the plume center, similar to the flow in a curved duct.<sup>22</sup>

For ramp injection, the primary vortex generation comes from the ramp not the injectant plume. Flow pressurization occurs in the shock layer between the ramp induced bow shock and the ramp compression face. This high pressure fluid then spills around the ramp causing a stream wise vorticity.<sup>10</sup> The vorticity causes large-scale convective mixing that forms a counter rotating vortex pair.<sup>6</sup> This mechanism is analogous to the vortex lift generated by a delta wing, except vortices are generated on both sides of the ramp. The relative strength of the vorticity generated is dependent on freestream Mach number, all other parameters and properties being equal. For a constant injector mass flux ratio, Hartfield et al. demonstrated indirectly through mole fraction contour plots that the vorticity created in a Mach 2.9 freestream "is much stronger than that generated at Mach 2".<sup>11</sup> Additional vorticity is imparted by the pressurized flow expanding over the rear face of the ramp and wrapping around the low pressure region encircling the underexpanded jet plume.<sup>12</sup> A final ramp induced vortex mechanism is baroclinic torque created by passing a shock through a jet, described by Waitz et al.<sup>6</sup> The shock is created by the recompression of the main flow. After expanding over the top to the rear face of a ramp, the flow must turn away from the wall behind the ramp, creating a shock. Waitz et al. reasoned the pressure gradient imposed by the shock across the density gradient of the freestream-injectant interface generates vorticity

along the interfacial density gradient.<sup>6</sup> This vorticity again forms a counter rotating pair, oriented additively with the other vortex generation systems.

The effect of side wall sweep on the ability of the ramp to generate vorticity has been established in previous works. Riggins and Vitt found that swept ramp similar to the one shown in Figure 2.2 produced a 30% increase in pressure over a straight sided wedge ramp of equal flow blockage.<sup>10</sup> The relatively stronger bow shock of the more three-dimensional swept ramp resulted in stronger spillage induced vorticity from three-dimensional relieving effects than the flatter, more two-dimensional unswept ramp.<sup>10</sup> In combusting flows, Northam and Capriotti found the swept ramp design increased combustion efficiency and had less total temperature sensitivity than the unswept ramp.<sup>16</sup>

Once the counter-rotating vortex pair is generated, it becomes the dominant mixing mechanism in the near field.<sup>5,6</sup> A cross section view of the developed plume remains circular, with "kidney bean"<sup>20</sup> structures forming around the vortex cores. The orientation of the vorticity is such that to an observer looking downstream at a bottom-injected jet cross section, the right side vortex would have a clockwise motion. The vorticity can be fairly intense; McCann and Bowersox measured 15,000 1/s rotation rate for 25° transverse injection into Mach 2.9 flow.<sup>22</sup> The strength of vorticity has been shown experimentally by Fuller et al. to decrease with increases in  $\bar{q}$ , resulting in reduced mixing.<sup>13</sup> At some point in the downstream flow, mixing becomes dominated by small scale turbulence as the vortex strength is dissipated. Hollo et al. found this length to be about ten  $d$  for tandem normal injectors in Mach two flow; this distance would increase for lower injection angles and faster freestreams.<sup>5</sup> Once the small scale turbulence has taken over mixing, equation (2.1) and the exponent  $n$  of section 2.3 can be used to compare mixing rates as the slope of the aforementioned Log-Log plots. However, the intercept of the maximum concentration decay line is decided in the near field by the effects of vorticity and the injector geometry. Therefore enhanced vortex mixing will be reflected throughout the flow field.

## ***2.5 Magnus Effect***

Vorticity also has an effect on penetration as well as mixing. For low angle ramp injections, the vortex pair provides a lift-off from the near wall due to a "magnus effect".<sup>6,11</sup> Consider a cross section view of a counter rotating vortex pair; the left side vortex rotating clockwise and the right side vortex rotating counterclockwise. The region directly above the vortex pair interface is an influx region due to the low pressure of the convergent vortical velocity components. Conversely, the region directly below the vortex pair interface is the outflux of the vortex pair. The resultant pressure differential along the vortex pair interface longitudinal axis results in the convection of the vortex pair towards the convergent spin side. The previously described baroclinic torque can adversely affect penetration through reversing the magnus effect. The vorticity imparted on a plume by a shock is oriented such that plume will migrate in the direction of the shock; a sufficiently strong shock reflection off of the opposing wall in a combustor could potentially negate or reverse the original vorticity. This action would either stop the outward magnus effect induced migration or create a movement back towards the near wall.<sup>6</sup>

## ***2.6 Computational Investigations***

The current state of computational fluid dynamics, or CFD, and numeric flow modeling applied to injection has advanced in pace with the explosive growth of computer power seen in the last decades. There are practical limits which CFD has proven unable to overcome. The first and most critical lacking of CFD is experimental results with which to validate CFD code. Numerous studies overcome this issue by co-opting existing experimental results and replicate them.<sup>12,13,23,24,25</sup> Code validation however is substantially separated from producing accurate results for complicated mixing schemes independently. Cost is another barrier to using CFD. For code employing the advanced full, thin layer or parabolized Navier-Stoke equations such as the SPARK code,<sup>12</sup> cost is on the order of \$10,000 per run.<sup>25</sup> The computational complexity associated with flow fields involving underexpanded injection, viscous boundary layers, solid objects in the flow and highly three-dimensional supersonic shock and expansion structures could be understated as non-trivial.

In spite of the limitations of CFD, progress has been achieved in several notable injection related test cases. An investigation into reacting parallel wall hydrogen injection was made by Brescianini and Morgan.<sup>23</sup> This computational effort was notable in that it included the previously ignored chemical

reactions and turbulent mixing in the solution of two-dimensional, steady parabolic Navier-Stokes equations for high enthalpy flows. Prior to this effort, the flow reactions and turbulent mixing was neglected because the computational power required for a solution was not available.<sup>23</sup> For this particular CFD-experimental comparison, the CFD code showed some agreement with the experimental data. However, considerable scatter and coarseness in the experimental data, which was generated in a pulsed facility, made exact determination of the source of data disparities impossible.<sup>23</sup>

Several investigations have been performed for two dimensional slot injection, which greatly reduces the difficulty in the numerical methods from three dimensional transverse injection. Gerlinger et al. conducted CFD analysis of a two-dimensional sonic slot injection into a supersonic freestream.<sup>24</sup> The intent of their investigation was to increase the robustness of near wall turbulence models by applying corrections to the standard  $q-\omega$  turbulence model. Comparison with similar experimental results revealed that two corrections, a limit to the turbulent length scale and a compressibility correction to the  $q-\omega$  turbulence model yielded the closest agreement.<sup>24</sup> A similar low Reynolds number effect comparison that compared favorably with experimental results was accomplished by Grasso and Magi.<sup>9</sup> They simulated transverse gas slot injection using Favre-averaged Navier-Stokes equation in an effort to accurately model the low Reynolds number effects encountered in the boundary layer, such as the separation bubble in front of a transverse jet slot.<sup>9</sup> Ramakrishnan and Singh conducted a simulation of normal slot  $N_2$  injection into a Mach 3.8 air freestream using the SPARK code which showed reasonable agreement with experimental data except in the upstream separation bubble region due to three-dimensional effects.<sup>8</sup>

Donohue et al. conducted a limited comparison of CFD and experimental results for 10° wedge angle swept ramp injection into Mach two flow.<sup>12</sup> The CFD approach employed the full three-dimensional Navier-Stokes SPARK code in comparison to experimental planar laser-induced iodine fluorescence (PLIIF) data. Results indicated the CFD analysis was generally within 5% of the experimental results, except for specific regions (the ramp base or the Mach disk region for example) where the agreement lessened.<sup>12</sup> The CFD code also underestimated the vortex strength due to insufficient grid resolution artificially enhancing viscous effects.<sup>12</sup> A later work by Donohue and McDaniel expanded the flow scope of the PLIIF measurement technique to cover the entire flow field.<sup>14</sup> Again, agreement on the order of 5% was found in the majority of the experimental-CFD comparisons, with exceptions as noted above.<sup>14</sup>

## ***2.7 Applications To Current Investigations***

This investigation combines elements of the previous injection systems in an as yet untried configuration. In this scheme, the injectant plume enters the freestream just upstream of a ramp designed to enhance penetration and mixing. The symmetric PME ramps were intended to test several effects. The first is the potential penetration enhancement from vortical lift-off of the compression face, or the magnus effect. The counter rotating vortices have been shown to create a lifting effect away from the injection wall. PME ramps SR 1, SR 2 and SR 3 (Figure 1.1) each present a progressively broader surface for this magnus effect lift-off to occur. Second, for each of the symmetric ramps, baroclinic torque generated by the ramp compression face has the potential to enhance fuel mixing. Each PME ramp in this group will generate a significantly different shaped conical shock, which should be reflected in the effect on vorticity. Ramp SR 2 has the most continuous and three-dimensional cross section, which should result in a stronger three-dimensional relieving effect. SR 3 has a broad, flat and straight sided wedge profile, which should create a very focused and strong bow shock. SR 1 has a faceted compression face to provide a step between the SR 2 and SR 3 ends of the dimensionality spectrum. Third, a uniform expansion over the model tops should occur. The expansion should have a detrimental effect on the vorticity cohesion, resulting in earlier vortex break down and greater mixing. Similar to the baroclinic torque effect, each model in the symmetric ramp group should produce a different focusing effect on the expansion. SR 1 has the narrowest profile at the peak of the ramp, which presents the smallest area for a strong expansion to occur. Ramps SR 2 and SR 3 have successively larger and broader cross sections for a strong expansion to occur. It is recognized that the second and third effects are contradictory. The measurement techniques available to this investigation are realistically capable of capturing vorticity enhancements and limited expansion effects only from flow visualization. If dispersion of the vortex is observed, then the third mechanism occurred. If not, then either the baroclinic torque enhancement exceeded the expansion dispersion, or the expansion dispersion did not occur as expected.

The second PME group, extended ramps, is similar to the previously explored injection ramps described in section 2.4 with the exception of a horizontal extension instead of the right triangle profile normally used (Figure 1.2 vs. Figure 2.2). These extensions are also the primary difference between this ramp group and the asymmetric ramp group, which allows a direct comparison of the effects, if any, they

yield. The extended ramps are expected to take advantage of several complementary effects. The first is an increase of near field vorticity. The injectant plume and freestream will both pressurize the upper surfaces of PME ramps ER 2 and ER 3, and induce spillage generated vorticity as well as baroclinic torque. This vorticity is expected entrain the freestream surrounding the ramps to enhance mixing, as well as provide a lift-off from the flat compression face of the wedge. Secondly, the ramps extension prevent an immediate expansion from disrupting the coalescing vortex pair. For both ER 2 and ER 3 the expansion over the top side to the rear face or edge should be minimal. Third, the extensions are a solid barrier to prevent any migration back towards the injection wall. Any impingement of the plume on the extensions should generate the magnus lift-off effect from the plume vortices. The fourth effect to examine is that of a trailing edge expansion on PME ramp ER 2 versus a trailing edge shock on ramp ER 3. Ramp ER 3 tapers to a sharp edge, whereas ER 2 tapers from  $2d$  to  $1/2d$ . Assuming supersonic flow around both ramp trailing edges, ER 2 should produce an expansion followed by a recompression shock, and ER 3 should produce only a recompression shock. These flow structures will be primarily oriented to spread outward horizontally, instead of the plume-intersecting vertical expansions produced by the symmetric ramp group. The only differences between the ramps ER 2 and ER 3 are the taper ratio and trailing edge configuration, therefore analysis of the available data can be tied directly to the geometry. PME ramp ER 1 was intended mainly for qualitative analysis. As such, and as a link between the symmetric ramps and extended ramps, it should prove insightful.

The final ramp group is the asymmetric ramps AR 1 and AR 2, Figure 1.3. These ramps were intended to provide a basis of comparison with the extended ramp group. Similar to the extended ramp group, spillage and baroclinic torque generated vorticity is expected to enhance the transverse injection vorticity. Both asymmetric PME ramps have a flat surface from which the vortex pair can generate a magnus effect and lift off. However, both AR 1 and AR 2 have vertical rear faces which should create a strong vertical expansions over the ramp peaks. The lower sweep angle of AR 1 should reduce the ramp generated vorticity from AR 2. Similarly, the larger expansion surface of AR 1 will create a stronger and more cohesive expansion. The combination of these two effects will weaken the vorticity generated by AR 1 when compared to AR 2, which should be reflected in the experimental results and flow visualization. Both asymmetric PME ramps will demonstrate the effect an expansion has on the vortex pair when

compared to the extended PME ramp results. Additionally, the recirculation zone just downstream of the ramp may prove useful as a flameholder for combustion.

For all of the above PME ramps, another prime consideration is total pressure loss. For each case the freestream and injection conditions are identical, therefore a direct macroscopic level comparison of total pressure loss is possible. Additionally, the total pressure losses incurred just by the transverse injection are available to normalize the PME ramp results. To minimize the total pressure loss, all PME ramp leading edges are parallel to the injection initial trajectory. Since the PME ramps are partially masked by the injectant plume, the total pressure loss increase from the blank transverse injection case should be reduced considerably. In other words, flow deflection caused by the ramps is approximately that of the injection, hence the strength of additional shock structures should be relatively small.

### ***III. Facilities and Instrumentation***

This chapter describes the facilities and instrumentation used to conduct this investigation. Descriptions of the hardware setup include the AFIT Mach three wind tunnel, the transverse injector and the eight PME ramps. A summary of the mean flow probes and the laser imaging system follow. The chapter concludes by detailing the data acquisition system and software.

#### ***3.1 AFIT Mach Three Wind Tunnel***

All tests for this investigation were conducted in the AFIT Mach Three wind tunnel. The AFIT Mach three wind tunnel is a blow-down design, employing a pressure-vacuum system. The pressurized air was supplied at 0.69 MPa by two Atlas Copco GAU 807 compressors at a 0.5 kg/s flow rate. The air was dried by two Pioneer R500A Refrigerant Air Dryers en route to the pressure side of the tunnel. Final drying and filtering is provided by a cyclone separator and multiple layers of Filtrite<sup>®</sup> filter paper.

The vacuum system consisted of 16 vacuum tanks of approximately 16 m<sup>3</sup> volume each. The evacuation was accomplished by three Stokes Micro Vac pumps, rated at 7.5 hp at 230 V. The vacuum tanks were evacuated to 8.0 mm Hg prior to each run. This level of vacuum provided approximately 25 seconds of acceptable tunnel run time

The tunnel consists of a plenum chamber upstream of a converging-diverging nozzle to create supersonic flow. The nominal Mach number of the nozzle is 2.8,  $\pm 1.8\%$ .<sup>27</sup> Flow straightening screens are placed between the tunnel air supply and the plenum chamber. An Endevco 0-690 kPag pressure transducer is mounted to the plenum chamber as the test total pressure measure. The total pressure fluctuations during tunnel test runs were no more than  $\pm 1.6\%$ . An Omega Engineering type K thermocouple provides plenum total temperature. The standard operating total temperature of the tunnel was 294 K during test runs. The total temperature fluctuations during tunnel test runs were no more than  $\pm 0.4\%$ .



### 3.2 Transverse Injector Model

The simple transverse injector model is described in full detail by McCann,<sup>26</sup> who originally used the injector setup to conduct a detailed turbulence study of low angle injection. Since a primary objective of this study is to measure enhancements to penetration and mixing of transverse injection, minimal modifications were made to the transverse injector.

#### 3.2.1 Tunnel Coordinate System and Dimensions

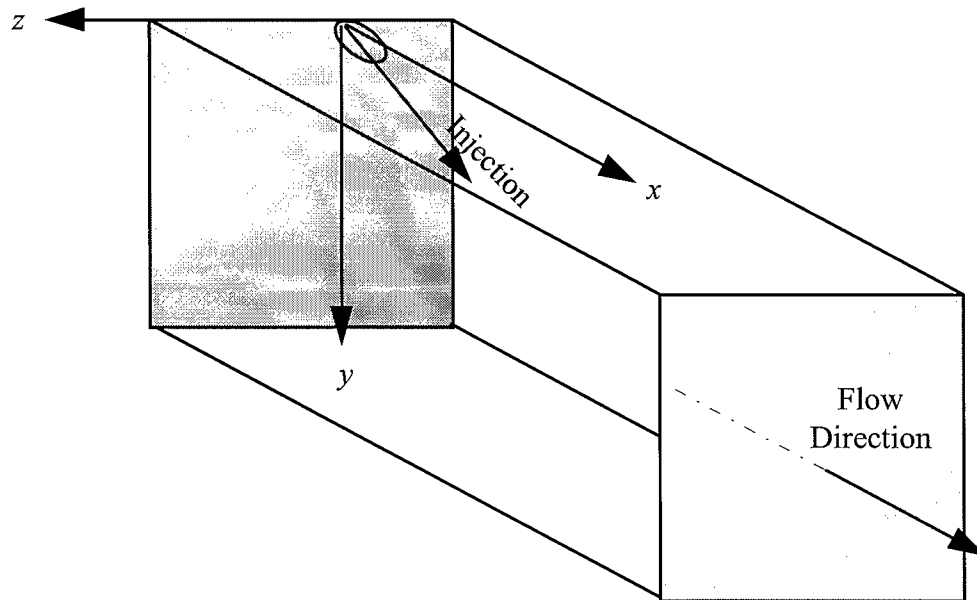


Figure 3.1: Tunnel Coordinate System

Figure 3.1 depicts the tunnel coordinate system relative to the injector nozzle exit. This figure is not drawn to scale. The physical dimensions of the tunnel and injector are summarized below.

TABLE 3.1  
WIND TUNNEL AND INJECTOR NOZZLE EXIT DIMENSIONS

Test Section Width	6.35 cm
Test Section Height	6.35 cm
Test Section Length	35 cm
Nozzle Exit Minor Axis Diameter, $d$	0.4 cm
Nozzle Exit Major Axis Diameter, $d_m$	0.92 cm
Distance From Tunnel Nozzle to Test Section	27.0 cm
Position of Injector Exit on Test Section	8.5 cm (from test section leading edge)

Table 3.2 summarizes the standard freestream conditions for a test run.

TABLE 3.2  
FREESTREAM FLOW CONDITIONS

Mach	2.9
$P_0$	217874 (Pa)
$T_0$	294 (K)
$P$	8028 (Pa)
$T$	114 (K)
$\gamma$	1.4
$U_0$	608 (m/s)

### 3.2.2 Injector Model Modifications

The primary physical modifications made to the injector model test section were the removal of a 1 cm deep 2.55 x 7.1 section of the tunnel ceiling directly behind (flow wise) and centered on the rear lip of the injector exit nozzle. The removed section enabled flush mounting of either the PME ramp models, or a blank section for simple transverse injection. A second modification was to bevel the settling chamber exit to smooth the flow transition into the injector nozzle. Figure 3.2, not to scale, shows the side view of the tunnel (negative  $z$  axis into page) with an example PME ramp in place.

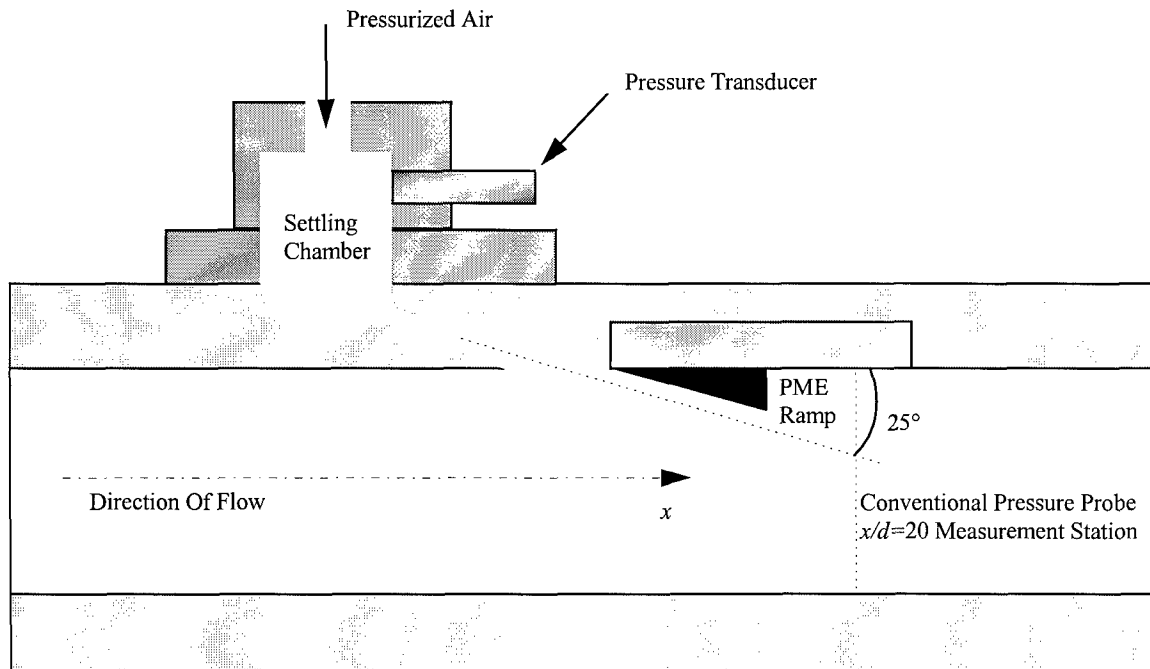


Figure 3.2: Side View of Test Section

The settling chamber consists of a 1.9 cm spherical bottom and a cylindrical top of the same diameter. The injector outlet from the spherical bottom shows the bevel described above. The throat diameter of the injector outlet is 0.3241 cm, expanding to 0.4 cm across the exit minor axis. The upper cylindrical portion of the settling chamber was tapped to accept an Endevco 0-690 kPag pressure transducer and a high pressure air line from the wind tunnel air supply. This arrangement ensures the total temperature of both the freestream and injectant are identical. For mean flow measurements, the settling chamber pressure was held constant at 30 psig.

### 3.2.3 Injection Parameters

Table 3.3 summarizes the relevant injector jet conditions. The variation in the following parameters is no more than 1.8%.

TABLE 3.3  
INJECTOR JET FLOW CONDITIONS

Mach	1.87
$P_{oi}$	304541 (Pa)
$T_{oi}$	294 (K)
$P_i$	47595 (Pa)
$T_i$	173 (K)
$\gamma$	1.4
$U_i$	493 (m/s)
$\lambda$	3.52
$\bar{q}$	2.85

### 3.3 PME Ramps

The dimensions of the PME ramps based upon the injector exit minor diameter  $d$  are shown in the following three-view drawings. Each ramp was machined to the front edge of an aluminum block that was fitted flush with the tunnel ceiling to reduce step shocks. The design philosophy of each ramp is detailed in section 2.7.

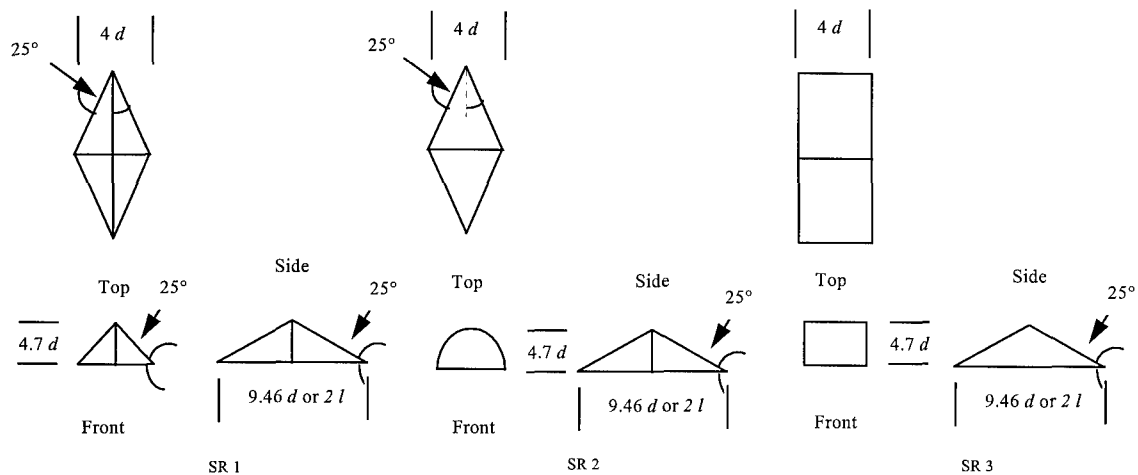


Figure 3.3: Symmetric PME Ramps

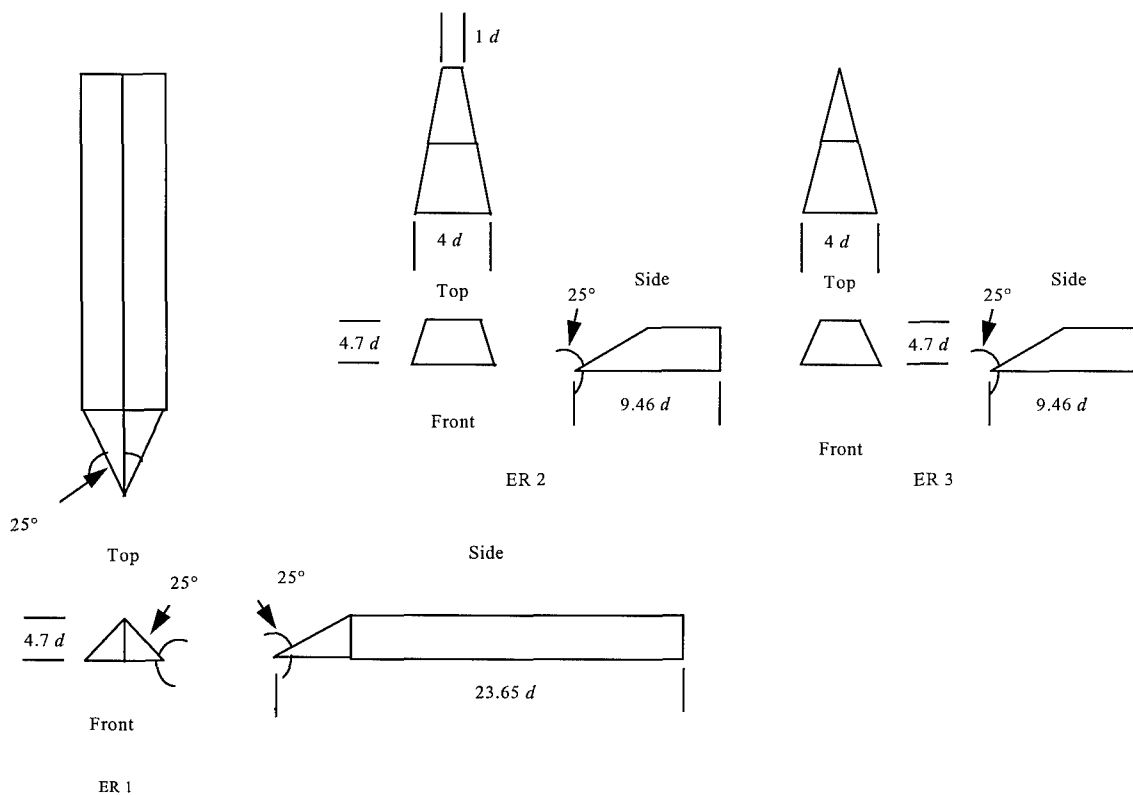


Figure 3.4: Extended PME Ramps

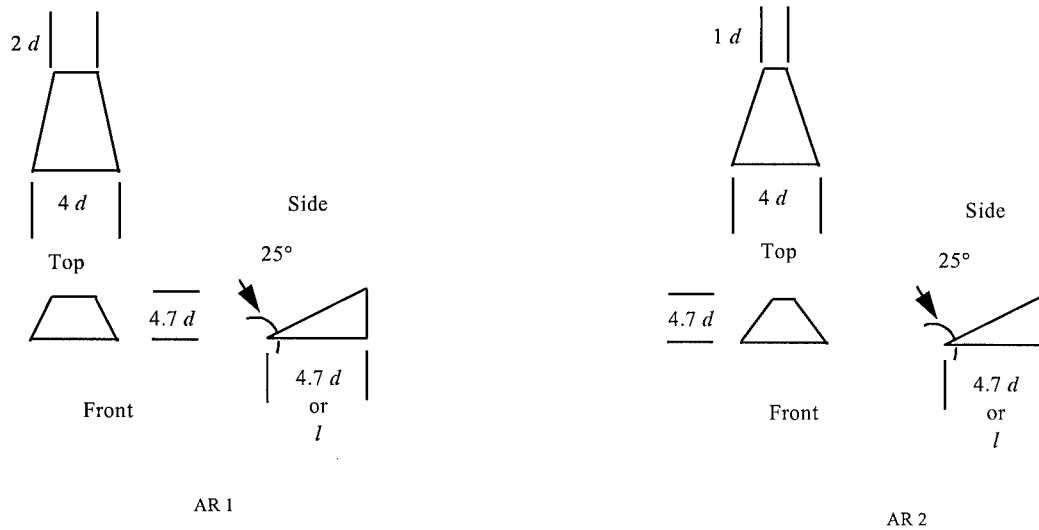


Figure 3.5: Asymmetric PME Ramps

### 3.4 Measurement Locations

The measurement location for the mean flow data occurred at  $x/d = 20$ . The  $z$  direction horizontal width of the tunnel consisted of 29 stations, each 0.1643 cm apart for a coverage of 4.60 cm. In the tunnel coordinate system, this is a range from -5.6 to +5.6  $z/d$ . This doubles the spatial resolution across a similar range used by McCann for mean flow measurements.<sup>26</sup> Vertically, the span covered was 5.08 cm, which translates to  $y/d$  from 0.4 to 11.5.

The cross flow oriented Rayleigh-Mie scattering laser sheet location is identical to the mean flow measurement plane. The laser sheet was sized to cover 5.08 cm of the tunnel cross section, and centered in the  $y$ - $z$  plane. The parallel oriented laser sheet was arranged along the tunnel centerline, parallel to the  $x$ - $y$  plane, and sized to cover 5.08 cm measured from the front lip of the injector nozzle exit. The useful coverage provided by the parallel oriented sheet ended approximately  $2d$  upstream of the mean flow measurement plane.

### 3.5 Mean Flow Probes

Mean flow data was acquired through a system consisting of pressure probes, transducers and a traversing mount.

### ***3.5.1 Pressure Probes***

Two types of pressure probes were used to collect the mean flow data. A Pitot probe constructed of 1.6 mm outer diameter stainless steel was fitted to a series of larger diameter tubes for structural support. The pressure sensed by the probe was fed by Tygon tubing to an Endevco 0-103 kPag transducer. The cone-static probe consisted of four evenly spaced circumferential 0.34 mm diameter taps that fed into a common chamber. This design is insensitive to misalignment errors up to 6° off centerline of the flow. The cone-static probe pressure was also fed into an Endevco 0-103 kPag transducer through Tygon tubing. For both probe types, the output of the pressure transducer was filtered by Endevco model 4225 signal conditioners. A specific signal conditioner was assigned and calibrated for each transducer used.

### ***3.5.2 Probe Traverse System***

The mean flow probes were swept through the vertically oriented  $y/d$  range for each of the 29  $z$  axis stations across the tunnel cross section. The traverse system used an Arrick Robotics MD-2 dual stepper motor driver and a Size 23 Stepper Motor.<sup>26</sup> The position of the traverse was recorded as a voltage by a TransTek Model 0217 linear voltage displacement transducer. For the range of motion the stepper motor traversed the probe through, the voltage-position relation was linear.

## ***3.6 Flow Visualization***

Two types of flow visualization were accomplished during this study. The first was shadowgraph photography. The second was digital imagery through Rayleigh-Mie scattering.

### ***3.6.1 Shadowgraph Photography Setup***

Shadowgraph images were taken for each injector configuration. Due to the limited coverage provided by the optical glass wind tunnel side walls, two images were needed to form a composite image to capture the flowfield around the injection and ramps. The light source used was a Cordin Model 5401 arc light with a 600 ns spark, and aligned by hand. The light was collimated by a 100 cm focal length mirror and passed through the test section. Polaroid Type 57 film was used for the images.

### 3.6.2 Rayleigh-Mie Scattering Laser System

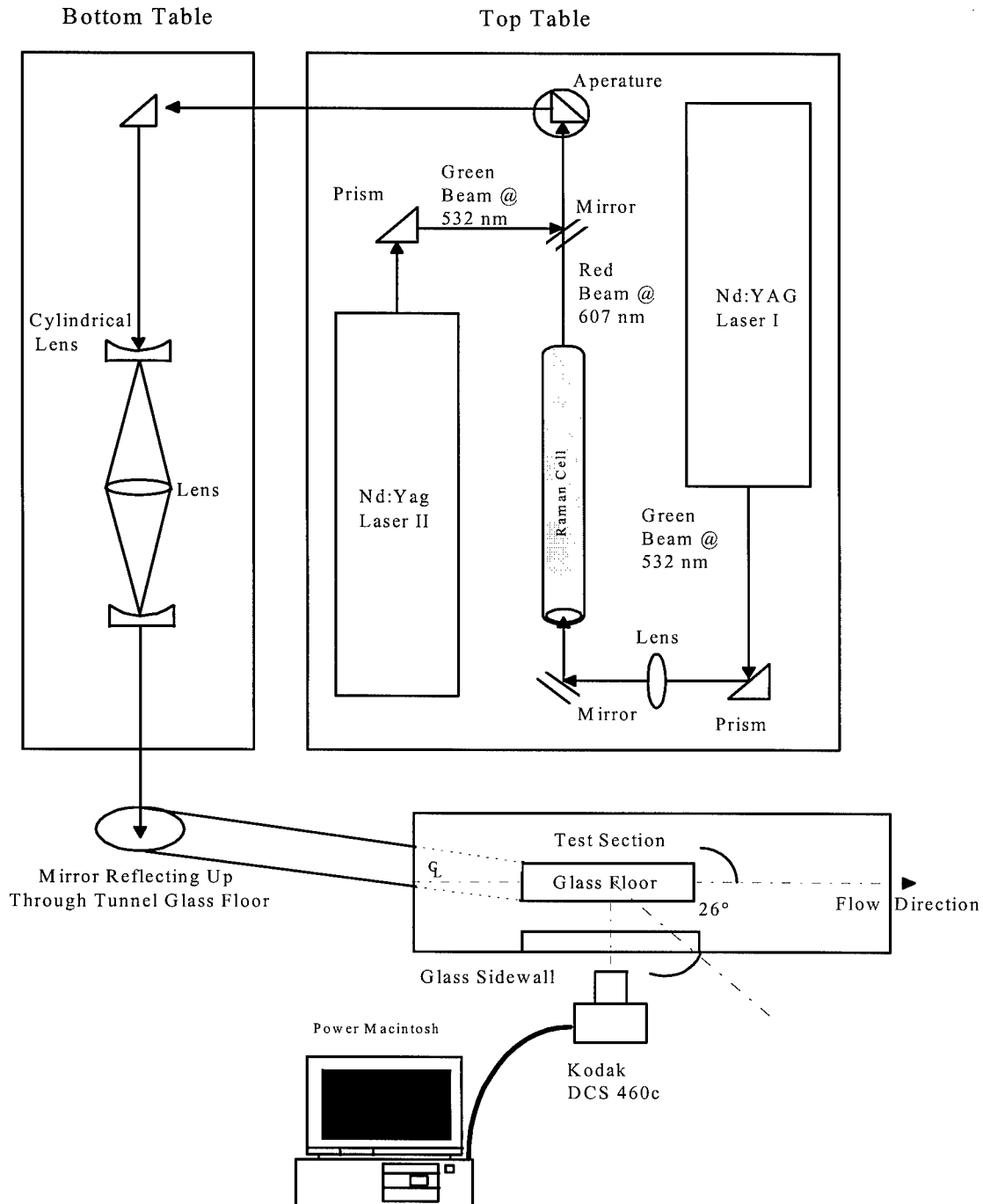


Figure 3.6: Rayleigh-Mie Scattering Laser and CCD System

The laser system depicted in Figure 3.6 was used to generate the digital images used in this investigation. The laser sheet was aligned through the cylindrical lens system on the lower table for either parallel or cross flow orientation. The view of the test section is a top view, looking down onto the glass

tunnel floor through which the laser passed. The CCD camera was mounted to a stable test support, and aligned either perpendicular or  $26^\circ$  off the tunnel centerline for the parallel and cross flow images, respectively.

The lasers used were two Surelite Nd:YAG lasers powered by two Continuum Model SLI-10 power supplies. The beams produced by each laser had wavelengths of 532 (green) and 1064 nm. The higher wavelength was filtered out with a series of beam splitters. The right side laser beam depicted in Figure 3.6 was passed through a Raman Cell to convert the 532 nm beam to 607 nm (red). The pulse duration of each laser was 10 ns, and the beam was pulsed 10 times per second (i.e., ten Hz).

The camera used was a Kodak Model 460C CCD camera, with a Nikon N90 lens. The exposure times used varied depending upon the type of image required. For instantaneous images, the exposure time was  $1/8$  seconds, with an f-stop setting of 5.6. Therefor, one 10 ns pulse was captured for each instantaneous image. The time-averaged images were exposed for four seconds at an f-stop of 16. The time averaging of the exposure captured 40 10 ns pulses.

### ***3.7 Data Acquisition System and Computational Resources***

Data acquisition was accomplished through the National MIO-16E PC based data acquisition board connected to an ACER Pentium computer. DANTEC Streamware<sup>®</sup> software was used to acquire the raw voltage readings collected by the MIO-16E board from the pressure probes. This board has a relative voltage response scale of 10 V. The sample rate used for data acquisition on all channels was 400 Hz. Once acquired, the data was converted to comma separated text files for processing by the data reduction routines.

The ACER Pentium PC provided data acquisition, traverse control and partial data reduction functions. Data reduction was also accomplished on a HP-48. AFIT Sun Sparc 2 and 10 workstations were used to generate all contour plots through TECPLOT. All other charts and plots were generated using Microsoft EXCEL. AFIT library scanners were used to convert the shadowgraph images to digital format. A Power PC 6100 was used to acquire and process the digital Rayleigh-Mie scattering images, which were converted from the raw Kodak digital format by Adobe Photoshop.



## ***IV. Data Reduction and Processing***

This chapter details the data reduction routines applied to the raw pressure probe data collected with the cone-static probe, the pitot probe, and the flow stagnation probe. The methods used to develop measures of the total pressure loss, plume penetration and plume area are detailed. The process of generating a mean flow image of the plume region and deriving quantitative relations from the images is also explained.

### ***4.1 Mean Pressure Measurements***

For both flow pressure probes the raw data were converted from gauge pressures to absolute pressures and reduced to mean pressure measurements. This was accomplished using a BASIC data reduction routine. The routine first scaled the probe voltages to psi by the appropriate factor depending on probe type. Second, the gauge psi values were converted to inHg and added to the atmospheric pressure in the wind tunnel room. Third, the converted pressures were averaged by groups of 41 points into a single point. The BASIC routine also determined the position of the probes by averaging the same range of traverse position voltages into a single point. At the 400 Hz sample rate, 41 samples comprised 0.1025 seconds of traverse movement. This span of movement covers 0.0323 cm for each mean datum and provides a spatial resolution of 142 mean datum over the 4.572 cm of traverse travel.

#### ***4.1.1 Determination of Flow Mach Number***

The Mach number at each mean point was determined through the ratio of the cone-static and pitot pressure data ( $P_c/P_{t2}$ ). The cone-static and pitot pressure data were collected on separate wind tunnel runs, and on separate days. The probe pressure ratios were normalized to each other with the recorded total pressure of the flow for the data run.

$$\frac{P_c}{P_{t2}} = \frac{P_c}{P_{t0}} / \frac{P_{t2}}{P_{t0}} \quad (4.1)$$

The Mach number relation to the pressure ratio  $P_c/P_{t2}$  was determined through a least squares fit developed by Bowersox<sup>29</sup> for a 10° cone-static probe.

$$\frac{1}{M} = -0.052976 + 4.6840x - 18.6786x^2 + 50.7006x^3 - 54.1577x^4 \quad (4.2)$$

Where  $x = P_c/P_{t2}$  and  $0.0805 \leq x \leq 0.358$ . Equation (4.2) is acceptable over the range of Mach numbers from 1.5 to 4.4, and has a standard deviation of 0.06%.

#### 4.1.2 Determination of Plume Static and Total Pressure

The static pressure of the flow within the plume was determined by application of the Rayleigh Pitot tube formula.<sup>30</sup>

$$\frac{P_1}{P_{t2}} = \frac{\left(\frac{2\gamma}{\gamma+1} M_1^2 - \frac{\gamma-1}{\gamma+1}\right)^{\frac{1}{\gamma-1}}}{\left(\frac{\gamma+1}{2} M_1^2\right)^{\frac{\gamma}{\gamma-1}}} \quad (4.3)$$

The total pressure in the injection plume,  $P_{t1}$ , differs from the tunnel freestream total pressure,  $P_{t0}$ .  $P_{t1}$  was determined from the Mach number relation of total pressure ratios. By multiplying equation (4.3) by the isentropic pressure relation<sup>28</sup>

$$\frac{P_{t1}}{P_1} = \left(1 + \frac{\gamma-1}{2} M_1^2\right)^{\frac{\gamma}{\gamma-1}} \quad (4.4)$$

of equation (4.4) to eliminate  $P_1$ , the ratio of  $P_{t1}$  to  $P_{t2}$  was determined.<sup>30</sup>

$$\frac{P_{t1}}{P_{t2}} = \left(\frac{2\gamma}{\gamma+1} M_1^2 - \frac{\gamma-1}{\gamma+1}\right)^{\frac{1}{(\gamma-1)}} \left(\frac{1 + \frac{\gamma-1}{2} M_1^2}{\frac{\gamma+1}{2} M_1^2}\right)^{\frac{\gamma}{(\gamma-1)}} \quad (4.5)$$

#### 4.2 Total Pressure Loss

Each injector ramp model produces a disturbance to the flow, and hence, a shock wave. The shock waves in turn reduce the flow total pressure. In addition turbulent mixing, which may be enhanced by the injector ramp, also causes total pressure loss. Since a primary objective of this research is to enhance injection penetration and mixing while minimizing the total pressure loss, a means to quantify the

injector ramp induced total pressure loss was required. A method was developed to determine the total pressure loss.

The method applied was to sum the total pressure ratio  $P_{t0}/P_{t1}$  across the test section of the simple transverse injection case and compare the results of similar integration for each injector ramp model. To normalize the results, the ratio of  $P_{t0}/P_{t1}$  of the simple transverse injection was divided by  $P_{t0}/P_{t1}$  for the injector ramp model. Therefore, the simple transverse injection has a loss parameter of unity, and the negative impact on total pressure of the injector ramp models would lower their respective loss parameters below one.

$$\Pi = \frac{(P_{t0} / P_{t1})_{\text{No Ramp}}}{(P_{t0} / P_{t1})_{\text{PME Ramp}}} \quad (4.6)$$

### ***4.3 Plume Area and Penetration Determination***

A definition of the plume was made to determine the possible enhancement by the various ramp injector models of plume penetration into the freestream. The plume is defined as the area within the search region where the Mach number was at 95% of the freestream value in the search region. This criteria is intended to capture plume and vortex structures, not necessarily the distribution of injectant or concentration information. The plume search region was initially constrained by  $y/d$  of 0.8 to 4, and  $z/d$  of  $\pm 2.4$ . A complication arose in establishing where the injectant plume ended and the boundary layer began due to using air for both the freestream and the injectant. There was apparent entrainment of the boundary layer by the plume's counter rotating vortices, as evinced in the thinner boundary layer in the area under the plume. Since the plume and boundary layer components are indistinguishable in these plots, flow visualization imagery was used to establish a cutoff between the plume and tunnel ceiling boundary layer. The demarcation between the plume and tunnel ceiling boundary layer was made at the point of greatest necking of the plume contours. The bottom, left and right side boundaries of the search region were selected to include the plume as well as freestream regions within the ramp injector model shock cone, without including the shock cone. Figure 4.1 shows the Mach contour plot of the simple transverse injector with the plume search region defined.

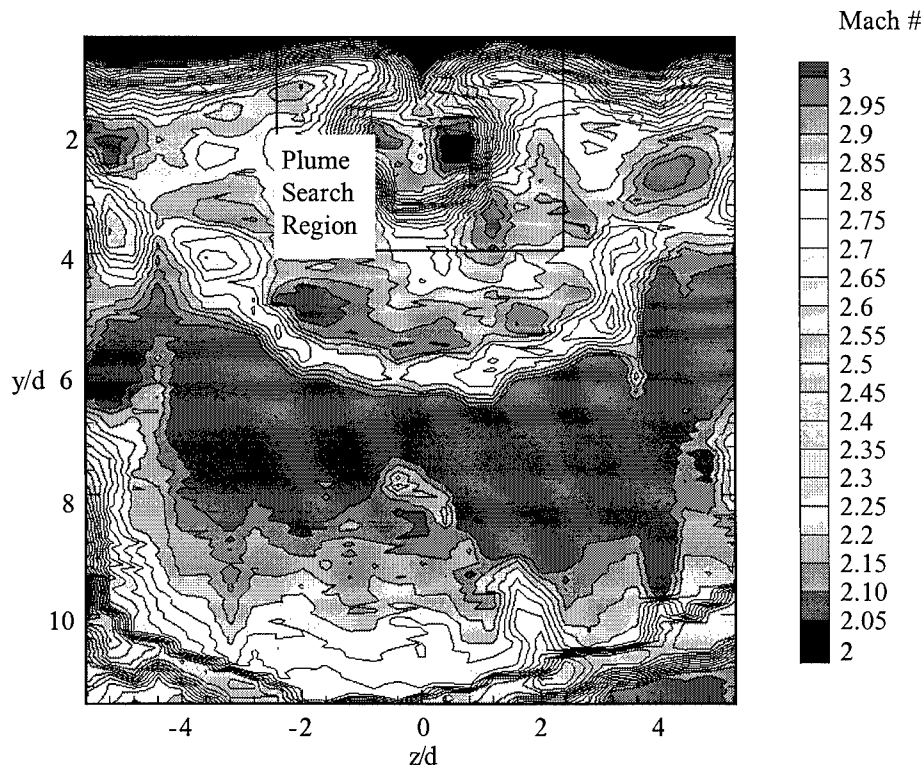


Figure 4.1: Simple Transverse Injector Mach Contour Plot With Plume Search Region

#### 4.3.1 Freestream Mach Number Definition

The region between the plume, the tunnel ceiling boundary layer, and the shock wave created by the ramp injector model and flow recompression around the plume is defined as the plume region local freestream. Two methods were used to establish the local freestream Mach number based upon quantitative assessments of Mach contour plots. These methods required first establishment of a rejection Mach number which was used to separate the data points associated with the plume, tunnel ceiling boundary layer and the recompression shock cone from the local freestream. The average of the local freestream Mach values were then used in the plume search region to determine the plume area as a percentage of the local freestream Mach number. The Mach contours were created with TECPLOT<sup>31</sup> at a contour separation of 0.05 Mach. A third method was developed to avoid use of the contours as a criteria. Each method has advantages and disadvantages depending upon the flow geometry around the plume.

#### **4.3.1.1 Freestream Mach Number Definition I: Graphical Method**

The first method defined the local freestream of the entire search region around the plume. At the 0.05 Mach contour resolution, the majority of plume contours were distinguishable from the freestream region due to the orderly, concentric, and proximate nature of the plume contours. The Mach number gradient,  $\partial M / \partial(\alpha) / d$  where  $\alpha$  is the tunnel coordinate direction, of the plot contours was used to establish the rejection Mach number of the freestream region. The search for a local freestream Mach contour that met this criteria had to be constrained to the upper half of the plume to avoid selecting an entrained boundary layer contour. The upper half of the plume was defined as the region above the  $y/d$  value where a tangent line to four or more concentric plume contours was vertical. In cases where there was asymmetry about the  $y/d$  axis in the plume, the average  $y/d$  value of both sides of the plume was used. The first contour, starting from the center of the plume, that was below a gradient of 0.25 was determined to be the freestream region. The Mach number of the contour defined as the freestream region was used in a SYSRPL data reduction routine to filter the entire plume search region data points by rejecting any points with a Mach number lower than the freestream contour. The average Mach number in the freestream was then determined as the average of the remaining data points. Figure 4.2 details the graphical method local freestream search region and the Mach number contour selected as the local freestream.

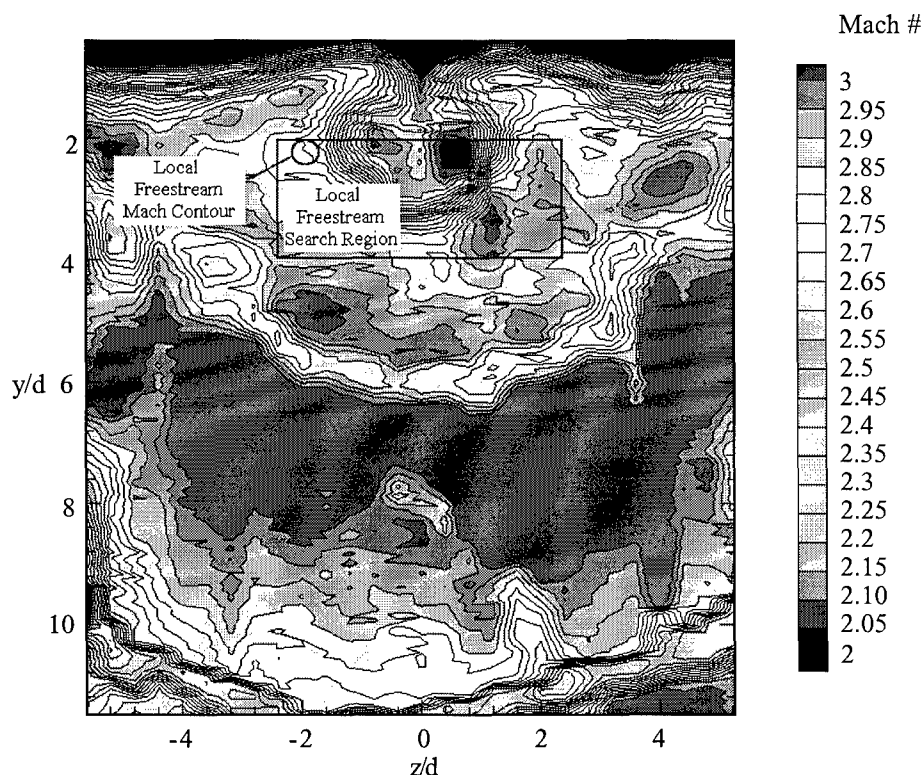


Figure 4.2: Graphical Method Local Freestream Search Region

For all ramp injector models, this method also eliminated the tunnel ceiling boundary layer and any included recompression shock cone data points. The advantages of this method are that it will reject low Mach numbers occurring in the freestream when there is a shock produced by the injector ramp intersecting the search region and plume. The disadvantage of this method is a criteria for the plume boundary that is consistent with each model and potential future configurations is dependent upon the resolution of the contour plots. It was found here that 0.05 Mach contours provide the highest resolution for the determination of flow structures; higher resolutions tend to collapse contour lines entirely into indistinguishable features, and are of dubious accuracy given the error of the probes used to measure and determine the Mach numbers.

#### 4.3.1.2 Freestream Mach Number Definition II: Box Method

The second method used to establish the freestream Mach number in the plume region applied a similar filtering method, using a modified version of the first method SYSRPL data reduction routine. The boundary of the plume search region along  $y/d$  of 4, and  $z/d$  of  $\pm 2.4$  was used to provide the data points. Instead of using the plume Mach contours to determine a rejection Mach number as in section 4.3.1.1, the tunnel ceiling boundary layer inside the recompression shock cone was used. The boundary layer Mach contours were distinguishable from the local freestream as relatively parallel and compacted in comparison.

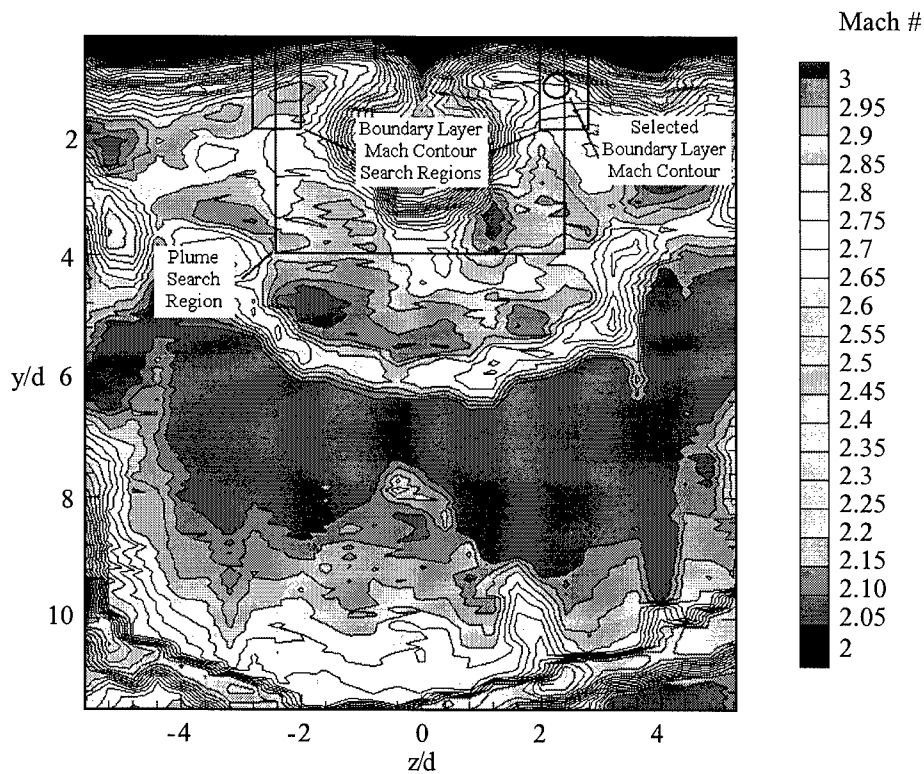


Figure 4.3: Box Method Local Freestream Search Region

The edge of the tunnel ceiling boundary layer was defined outward from the tunnel ceiling as the lowest Mach contour with a Mach number to injector diameter gradient less than 0.25 at any location from the next interior boundary layer contour. The boundary layer contours were tested along the  $z/d$  of

- 2.8 to - 2.0 and 2.0 to 2.8 on each side of the vertical boundaries of the plume search region for this condition. Figure 4.3 shows the boundary layer-local freestream search regions.

The  $\pm 0.4$  range around the vertical search region boundaries confined the boundary layer contours to those least affected by the injector ramp shock cone impingement or the plume entrainment region. Again, this rejection criteria proved suitable for elimination of the ramp injector model-recompression shock cone, which for all models had lower Mach numbers than the tunnel ceiling boundary layer. The advantages and disadvantages of this method are the same as the graphical method with one additional disadvantage. This method tends to be the most subjective of the methods used, as the intersection of the tunnel ceiling boundary layer and the recompression shock cone can occur in the horizontal search regions ( $z/d$  of - 2.8 to - 2.0 and 2.0 to 2.8). In such cases, the intersection area usually has a lower than 0.25 gradient. However, because of the spreading effect of cone-static probes on shock waves, these regions are not considered representative of the local tunnel ceiling boundary layer. Subjectivity becomes a factor when the experimenter must decide to use or not use a rejection Mach contour based upon proximity to a shock-boundary layer interaction. In this investigation this was not a problem because there were boundary layer contours that met the gradient criteria inside the plume search region vertical boundaries.

#### ***4.3.1.3 Freestream Mach Number Definition II: Modified Box Method***

A second use of the box method, with slightly different criteria, was also tested. In the second method, no contours were dropped from the average Mach number calculation based upon a rejection Mach number. The top of the vertical boundaries were selected at both  $y/d$  of 1.2 and 1.6. For most models,  $y/d$  of 1.2 was well outside the apparent boundary layer; those cases in which it was not is noted. The bottoms of the vertical boundaries and the sides of the top boundaries were also cropped to avoid including the recompression shock cone. The average Mach number was then the average of all points along the lines, with no filtering. The results of this method correlated well with those of the graphical and box method. The advantage of this method is an independence from determining a graphical based criteria to separate the plume. The major disadvantage, as seen with models ER 2 and ER 3, is that it will not reject the low Mach numbers of a shock wave passing through the plume. This lowers the computed value of the overall freestream speed, and reduces the plume area in turn.



#### **4.3.2 Plume Area Determination**

With the freestream Mach number established, the plume region was distinguished from the freestream using a SYSRPL filtering routine. To avoid counting the tunnel ceiling boundary layer as the plume area, the upper limit of each ramp injector model plume search region was lowered to the top of the plume. The effect of reducing the upper limit confines the search to the circular portion of the plume, which is consistent with previous researches<sup>3,12</sup> and the flow visualization accomplished in this investigation (see Figure 4.8). The routine counted all points in the plume region that had a Mach number of 95% or less of the freestream Mach number. The criteria of 95% of the freestream Mach was selected after comparison with the 99% and 90% criteria. The 99% criteria was rejected after review of the contour plots. Because of the varying freestream Mach number around the plume, the 99% criteria captured large areas of the freestream. The 90% criteria was rejected as being too low a resolution; at the 90% Mach contour the plume areas show little separation. Thus the contours below 90% are useful for confining the plume core, while the contours above 90% contain the plume outer layers. Since the outer layers of the plume have been identified as important mixing regions by Fuller<sup>13</sup> and McCann,<sup>26</sup> inclusion of this area is important. The 95% criteria provides ample separation from the freestream, but also includes the outermost mixing layers. To avoid capturing the ramp injector model shock cone, the search area of the plume region was further constrained to exclude any shock cone Mach number contours that were less than the freestream Mach number. Each datum represents a rectangular area of 0.1588 cm in the  $z$  direction, and 0.0323 cm in the  $y$  direction, for an area of  $0.005161 \text{ cm}^2$ .

### **4.3.3 Plume Penetration Determination**

A measure of plume penetration into the freestream was put forth by McCann and Bowersox.<sup>22</sup> This method of measurement was based on the distance from the tunnel ceiling to the plume center. An approach put forth by Fuller<sup>13</sup> used a threshold 0.5% mass fraction of helium injectant to define the outermost plume boundary, and hence the furthest penetration into the freestream. Since this technique is not available for this investigation, the definition of McCann and Bowersox was used. The centroid of the plume area was found based upon the integral relation

$$\overline{y/d} = \frac{\int (y/d) dA}{A} \quad (4.7)$$

which was computed by a SYSRPL routine.

## **4.4 Flow Visualization Techniques**

Flow visualization was accomplished through two methods. The first method is shadowgraph photography, which for this study is used for qualitative analysis. The second method employed a two inch wide Nd:YAG laser sheet and gaseous particle seeding through the injector nozzle. The laser sheet was oriented both parallel and perpendicular to the test section y-x plane for each model. Both orientations provide detail about the penetration and mixing of the flow.

### **4.4.1 Parallel Flow Orientation**

The parallel oriented laser sheet was adjusted to cover two inches of the test section starting at the forward edge of the injector port, and centered along the test section longitudinal axis. Two types of digital images were attained in this orientation for each injector ramp model. The first image type was an instantaneous image, which was taken with a digital camera with an f-stop setting of 5.6 and exposure time of 1/8 seconds. The laser was pulsed at ten Hz during the exposure, effectively freezing the flow in the image. Figure 4.4 is an example of an instantaneous image.

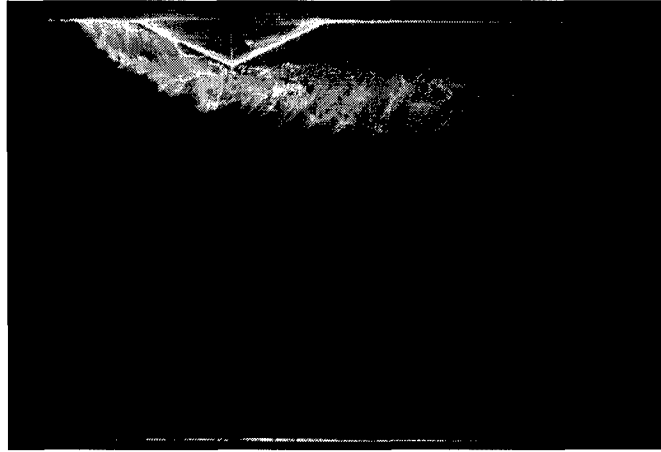


Figure 4.4: Instantaneous Digital image, Model 1

These images capture the extremely unsteady nature of the vorticity in the axial direction. The second image type is a time-averaged image acquired at an f-stop setting of 16 and an exposure time of four seconds (i.e., 40 laser pulses). This combination has the effect of averaging the image, Figure 4.5, which allows meaningful quantitative analysis.

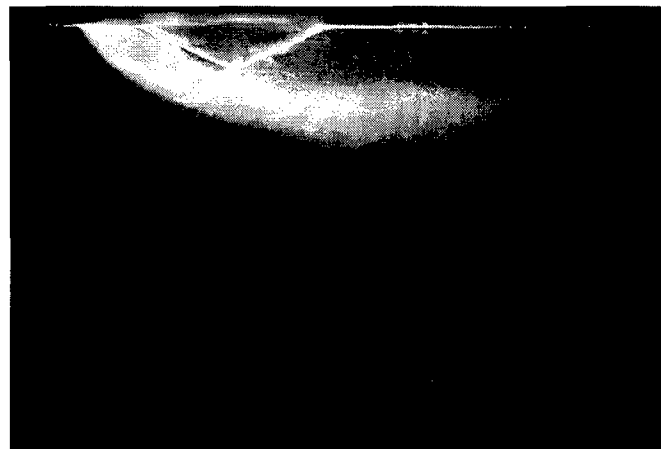


Figure 4.5: Averaged Digital Image, Model 1

Two types of analysis were applied to the parallel oriented average images. The centerline trajectory of the plume was determined. Also, a measure of the rate at which the image intensity decays in the axial direction was made.

#### ***4.4.1.1 Parallel Flow Orientation Analysis, Plume Trajectory Determination***

The method to establish the plume trajectory was based upon the grayscale intensity of each pixel in the digital image. The images were first converted from color bitmaps to 256 shade grayscale bitmaps. This process assigns ASCII characters 0 to 255 to each pixel depending upon intensity, where ASCII character number zero corresponds to black, and ASCII character number 255 corresponds to white. A SYSRPL routine was used to interrogate the numeric value of the ASCII character representing a pixel. The column and row position of the pixels above a threshold value of ASCII character number 75 were recorded for twenty axial stations, covering from the center of the injector exit to 17 diameters downstream, near the end of the laser sheet, as shown in Figure 4.6.

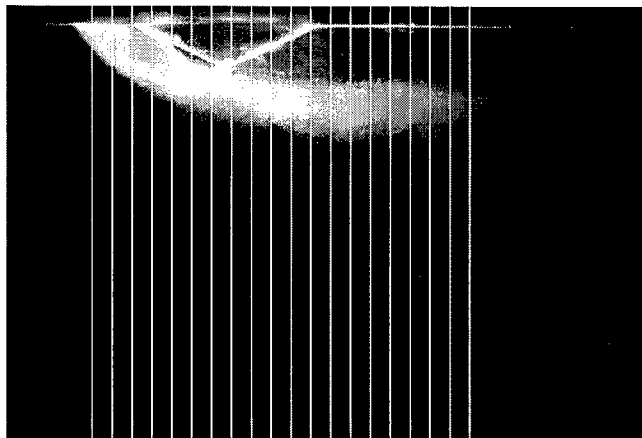


Figure 4.6: Plume Image Measurement Stations

Before the images could be processed two steps were taken to ensure reliable results. Despite coating the tunnel ceiling and the injector ramp models with flat black paint to reduce reflections, a noticeable glare can be seen in the photographs. To avoid detecting the glare as part of the seeded plume, all solid injector ramp model and test section boundaries were filled with black. Additionally, in several of the images large globules of seed can be seen, Figure 4.7.

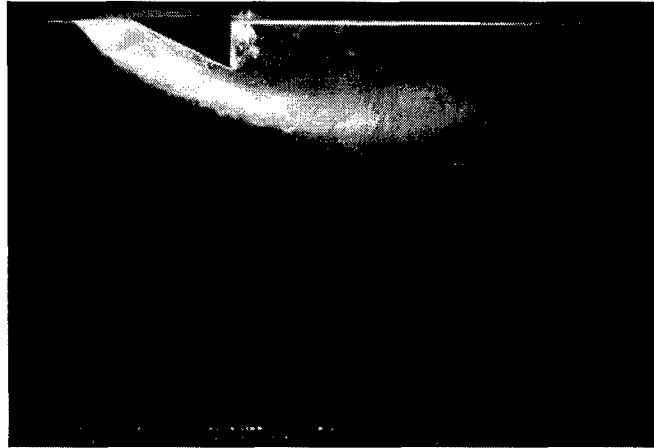


Figure 4.7: Seed Condensation On Ramp Injector Model

The liquefied globules are distinguished from the gaseous plume in the images by a higher intensity of laser reflections. The globules were observed during the test data acquisition to be caused by the vaporous seed condensing onto the injector ramp models and then shedding into the freestream. The long exposure times the average images required contributed to the seed build-up and shedding, which is not as present in the short duration instantaneous images. An additional factor in the seed liquefaction for either image type was whether the image was acquired early in the tunnel operation, or near the end of the run time. Liquefied seed build-up on the ramp injector model surfaces generally do no effect the trajectory determination, as the solid model boundary is a plume limit. Condensed seed in the freestream or boundary layer will tend to skew the trajectory from the observed plume. Where condensed liquid seed is present in the freestream or boundary layer of an image only the gaseous plume portion is used to determine the trajectory.

The images were processed with a SYSRPL routine which for each of the twenty axial locations found the upper and lower plume boundaries based upon pixel intensity. The upper and lower plume boundaries were used to quantify the extent of injectant dispersion and penetration. The average between the two boundaries was used to plot the trajectory of the plume centerline. A curve was fitted to the data points and the height of the center of the plume image was compared to the mean flow centroids.

#### ***4.4.1.2 Parallel Flow Orientation Analysis, Rate Of Centerline Decay***

Due to the limitations of this investigation, exact rates of concentration decay with downstream position are not possible. However, approximate and relative measures are possible. The laser illuminated sheet of seed particles can provide a measure of how quickly the concentrated center of the plume is dispersed by the injection generated vorticity. As the plume enters the freestream, it is largely a homogenous entity,<sup>19</sup> which can be seen in Figures 4.4 and 4.5. As the plume turns roughly parallel to the freestream the injection generated vorticity becomes the dominant mixing mechanism.<sup>4,13</sup> This mixing action spreads the injectant to the periphery of the plume which in turn reduces the concentration of the injectant at the centerline. The intensity of the plume digital image is seen to decay along the centerline as a result of this action, which is consistent with previous investigations.<sup>6,11</sup>

There are several caveats associated with this analysis. The plume seed is not ideal and cannot totally map the injectant locations. The laser sheet loses intensity along the fringes, which could contribute to a decay in the image. The quantity of seed injected in each test run varied slightly, which affects the level of intensity reflected. To compensate for this issue, the intensity of each image is scaled according to the intensity at the injector nozzle exit. This procedure will level the effect of variations in the quantity of injected seed. Additionally, though not ideal, the seed should map each injector ramp flowfield in a similar manner. A relative comparison was therefore possible. The loss of intensity in the laser sheet does not appear to have affected any of the images as the reflected intensity decays well upstream of the end of the laser sheet, Figure 4.7.

The process of determining the rate of centerline decay follows from the procedure for finding the plume trajectory. For the twenty axial stations outlined in Figure 4.6, the average of the plume pixel intensities was determined by a SYSRPL routine. The average intensity for each location was scaled by the average intensity of the injector nozzle exit plume pixels. An average intensity was then plotted against downstream axial location. The effect of liquefied seed artificially raising the average intensity value is recognized. To eliminate the effects of liquefied seed, an upper threshold was used to filter out points too intense to be gaseous plume.

## ***V. PME Ramp Flow Field Results And Analysis***

This chapter describes the flow field for each of the nine injector configurations (simple transverse injection and the eight ramp cases). The three basic qualitative and quantitative techniques, shadowgraph photography, mean flow pressure data and laser imaging are employed collectively for each model. This is necessary because together the available data provides a consistent and complete analysis of the injection flow field that the individual techniques alone can not. The PME ramp models with similar geometries are grouped and compared independently to simple transverse injection. Chapter five is organized into four subsections, one for the simple transverse injection analysis and the three PME ramp groups. The case of injection over a simple transverse tunnel ceiling is presented first to illustrate the salient flow features and to provide a basis of comparison. The first PME ramp group is those models which are symmetrical about the  $y$ - $z$  plane of the tunnel coordinate system, which includes models SR 1, SR 2 and SR 3. The second PME ramp group is the models with extended surfaces beyond the initial ramp, or models ER 1, ER 2, and ER 3. The final PME ramp group is the asymmetric swept ramps, models AR 1 and AR 2 which have geometries that have been the subject of extensive experimental and numerical investigations in the past.<sup>10,11,12,13,16</sup>

For all configurations studied, the following order of analysis is used. First, shadowgraph flow visualization images are used for qualitative analysis. The basic flow shock structures along the centerline  $x$ - $y$  plane are examined. Second, the laser sheet images are qualitatively analyzed in both parallel and cross flow orientations. Third, the mean flow field pressure data results are presented, from which Mach number contour plots were computed. Fourth, the four methods of determining the plume region local freestream Mach number as defined in section 4.3.1 and attendant injection plume area at the measurement station are tabulated, and contour plots comparing the results are presented. Fifth, the centroid based plume penetration values are analyzed. Sixth, the total pressure loss parameter for each injector ramp model is presented. Seventh, quantitative analysis of the digital images plume boundaries and centerline mean plume trajectory of the averaged digital images are plotted. The rate of decay of the

plume centerline digital image intensity is plotted and correlated with the cross flow image data and the pressure probe results.

### **5.1 Simple Transverse Injector**

Injection over a flat or simple transverse model provides a relative basis of comparison for the objects of this investigation: plume expansion, plume penetration and total pressure loss. The following sections provide a fundamental analysis of flow structures and observations common to all injector models. Basic injection induced flow structures are examined through flow visualization and quantitative techniques, and compared to previous researchers. Results for four quantitative methods of determining plume area and penetration are summarized in Table 5.1. Pressure losses in the form of the total pressure loss parameters  $\Pi$  is presented for use in normalizing the total pressure losses of the PME ramps.

#### **5.1.1 Simple Transverse Injector Flow Visualization**

This section includes all of the flow visualization accomplished for the simple transverse injector. The shadowgraph is used to determine basic flow shock structures. The parallel oriented laser sheet instantaneous and time averaged images are used to provide details of the plume structures observed. The cross flow oriented laser sheet instantaneous and time averaged images depict the plume shape and show the plume vortex mechanisms in action.

##### **5.1.1.1 Simple Transverse Injector Shadowgraph**

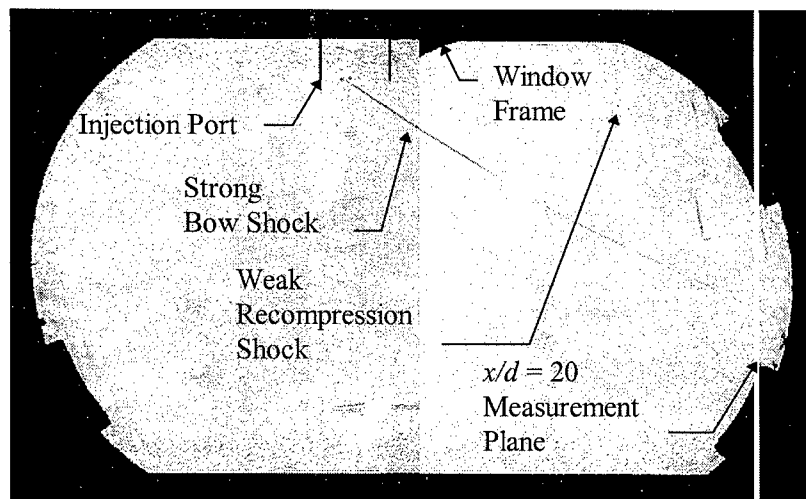


Figure 5.1: Simple Transverse Injector Composite Shadowgraph



Figure 5.1 shows a composite of two shadowgraphs for the simple transverse injector model. Boundary layer structures are visible in Figure 5.1 along the lower and upper surfaces up to the point of injection. After injection, the upper boundary layer is disturbed and does not appear as clearly as before. Just above the upper boundary layer and slightly behind the injection point is a strong bow shock created as the plume enters the freestream. For injection of an underexpanded jet into a supersonic freestream, the plume acts as a blunt body which results in the strong shock.<sup>4</sup> The plume main shock starts at an angle of approximately  $33^\circ$  then bends to approximately  $25^\circ$  by the middle of the test section. A weaker secondary shock can be seen above the main bow shock as a faint roughly parallel line towards the right side of the picture (the divergence is about  $5^\circ$ ). The origin of this shock is not visible in this image but it can be seen to exit the image at about the middle of the upper right window clamp. This shock is a recompression shock created as the main flow rejoins around the plume. This shock is limited by two mechanisms. First, there is only a relatively small height between the bottom of the plume and the tunnel ceiling boundary layer where recompression can occur. This height is created by the plume as it enters the freestream and rises to the height of the Mach disk, before turning in the direction of the main flow. Second, above and in the plume there is either no main flow expansion or the plume expansion prevents the main flow from recompressing. The secondary shock appears to form on the bottom side of the plume, though it most likely forms on the top side of the plume and passes through it.

The small black triangle at the top and center of the image is the side wall of the optical glass window. Due to the alignment of the images inclusion of part of the tunnel window side wall was necessary. A very weak shock is faintly visible crossing from left to right and top to bottom of the image at  $20^\circ$ . This weak shock is due to a small misalignment upstream of the test section. The vertical streaks throughout the image are due to the film used and are not part of the flow structure. The two bright patches near the bottom boundary layer are due to light reflection. The rectangular blocks along the glass periphery are window clamps. The measurement plane for the pressure probes is indicated in Figure 5.1.

The plume structures are visible in this shadowgraph, though not clearly due to obscuring effects of the boundary layer and the plume vorticity. Further analysis of the plume structure is made in the

following section with the parallel oriented laser sheet image. A much more illuminating analysis can be developed from the side laser sheet images.

#### ***5.1.1.2 Simple Transverse Injector Parallel Oriented Images***

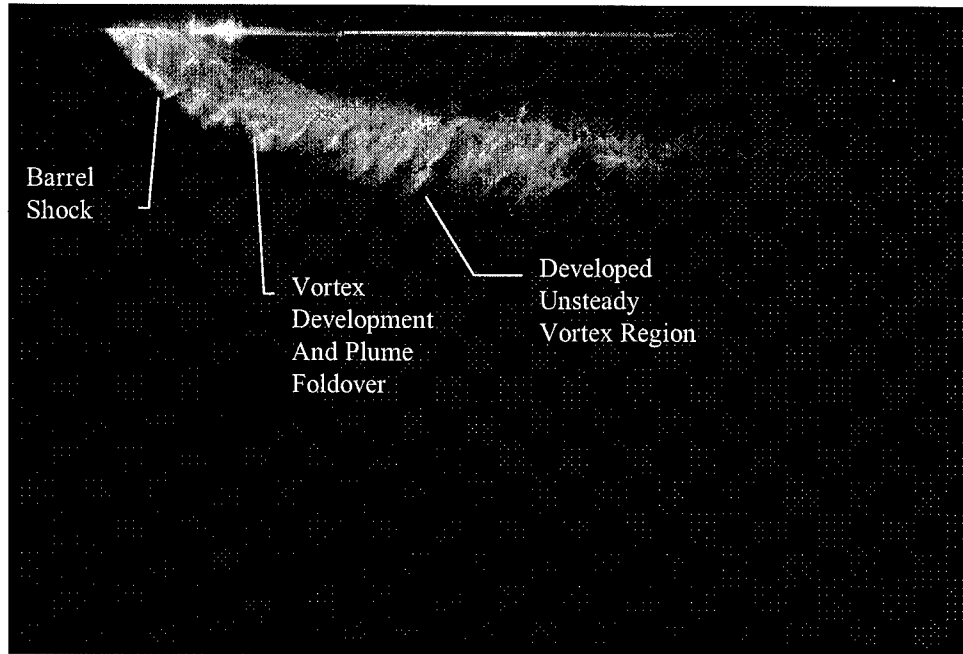


Figure 5.2: Simple Transverse Injector, Instantaneous Parallel Oriented Laser Image

Figures 5.2 and 5.3 show the plume seeded and illuminated as described in section 4.4.1. The barrel shock, outlined in Figure 5.2, created by the underexpanded plume isentropically expanding then compressing is visible, as well as the general area and orientation of the Mach disk that terminates the barrel shock. The barrel shock region provides the majority of the vorticity generation for the plume. As the plume protrudes out of the boundary layer, the high velocity freestream wraps around both side of higher pressure plume and imparts a rotation.<sup>4</sup> The rotation manifests itself as counter-rotating vortex pair, which has been identified as the major mixing mechanism for this type of injection.<sup>6</sup> In measurements under similar circumstances (i.e., in the same tunnel using the same injector but at a different injection pressure ratio) McCann and Bowersox<sup>22</sup> measured a maximum axial vorticity of approximately 15,000/s at the downstream  $x/d$  of 40 location.

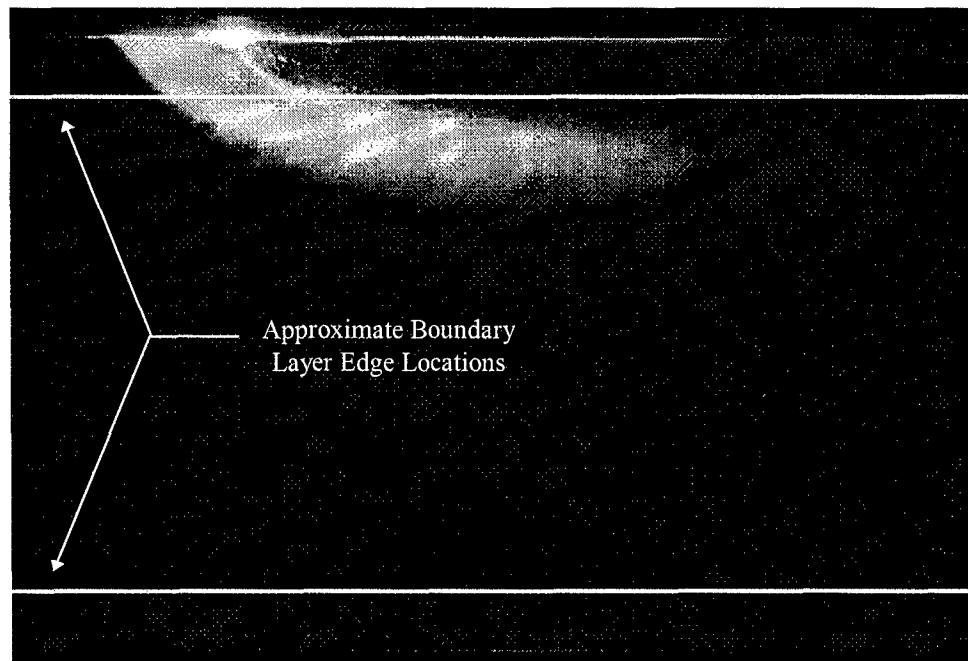


Figure 5.3: Simple Transverse Injector, Time-Averaged Parallel Oriented Laser Image

Beyond the barrel shock the plume turns sharply towards the downstream direction which in turn aligns the vortices roughly axially. In Figure 5.2 this is annotated as the "vortex development and plume foldover region." Directly above the barrel shock, the plume is seen to roll back up towards the tunnel ceiling. This foldover of the plume obscures the bottom right of the barrel shock. After the bend in the plume, no vorticity is imparted and the plume becomes a streamwise vortex mixing structure that decays and dissipates from viscous effects. The highly unsteady vortex structures visible in Figure 5.2 are due to the short exposure time used which effectively froze the helical structure of the plume. A rapid decrease in the plume intensity towards the right side of the image is apparent in Figure 5.3. This intensity drop-off is consistent with centerline planar injectant mole fractions measurements, which show a marked concentration drop in the 15-20  $d$  region for a Mach two freestream.<sup>5</sup> Noted on Figure 5.3 are the boundary layer edges as determined from the shadowgraph image, Figure 5.1. Finally, the extremely bright spots at the rear lip of the injector port in both images are the result of seed particles being drawn upstream by the two recirculation cells shown in the surface flow visualization of Bowersox.<sup>20</sup>

### 5.1.1.3 Simple Transverse Injector Cross Flow Images

Figures 5.4 and 5.5 show the cross flow oriented instantaneous and time-averaged images respectively for the simple transverse injection case.



Figure 5.4: Simple Transverse Injector, Instantaneous Cross Flow Image

Figure 5.4 is typical of the cross flow instantaneous images acquired in this investigation. As the helical vortex structure is convected downstream, only a portion it will be visible passing through a cross flow plane. Figure 5.4 shows the bottom of the counter rotating vortex pair passing through the laser plane while the remainder of the vortex loops are on either side (and hence not visible) of the laser plane. The instantaneous cross flow images for the remaining models are presented in Appendix B. In Figure 5.5, the effect of time-averaging to capture the cross-section of the vortex pair is apparent. The plume seed has been spread into a roughly crescent shaped area, and the unseeded tunnel ceiling boundary layer has been drawn into the central core of the plume. Starting at the bottom outside of the image and traveling up either of the side structures, the width of the seeded plume is seen to diminish. The crescent shape of the plume therefore indicates that the maximum concentration of seed remains in the centerline plane as it is being spread around the periphery. This and similar images confirm the seed is mapping the areas of high plume concentration.<sup>13</sup>

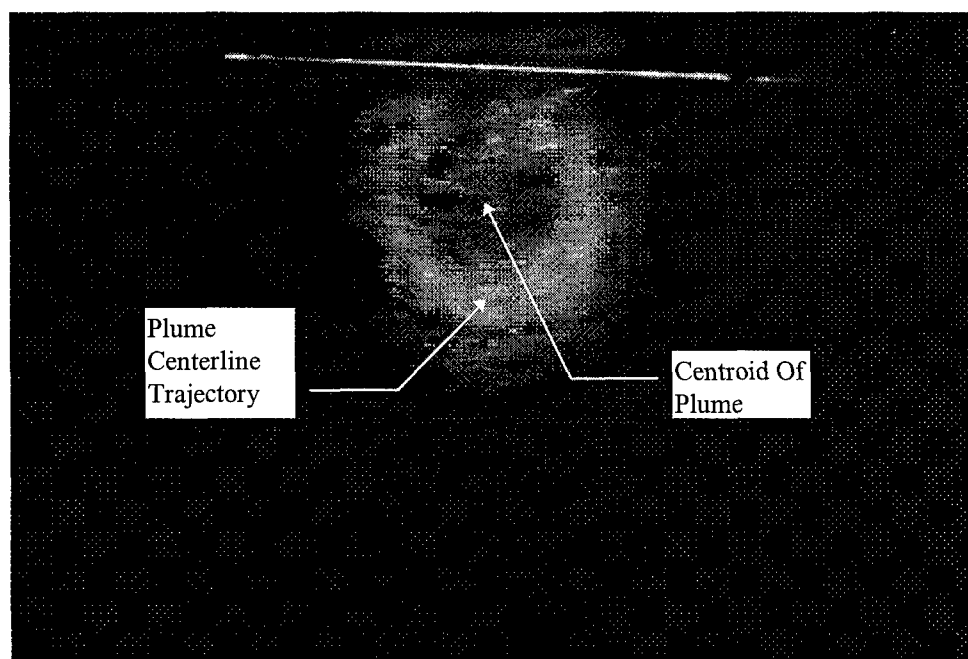


Figure 5.5: Simple Transverse Injector, Time-Averaged Image Cross Flow Oriented Image

The distinction between the plume centerline and plume centroid annotated in Figure 5.5 is important for the following quantitative analysis. The plume centroid is a measure of plume penetration into the freestream developed from the Mach contour plots as outlined in section 4.3.3. The plume centerline trajectory measures the height the maximum concentrated outer portion of the plume penetrates into the freestream, and will always be greater than the plume centroid.

It is also clear from these images that the plume is no longer a homogenous entity. To clarify the ensuing discussion, the term plume will refer to the entire mixing structure whereas injectant or seeded plume will refer only to the injected fluid. The counter-rotating vortex pair generated by the transverse injection have coalesced into separate structures, each pulling down and entraining the boundary layer above. The vorticity has also spread the seeded injectant along the boundary of the circular plume region, which increases mixing with the local freestream.

### 5.1.2 Simple Transverse Injector Mach Contour Plots

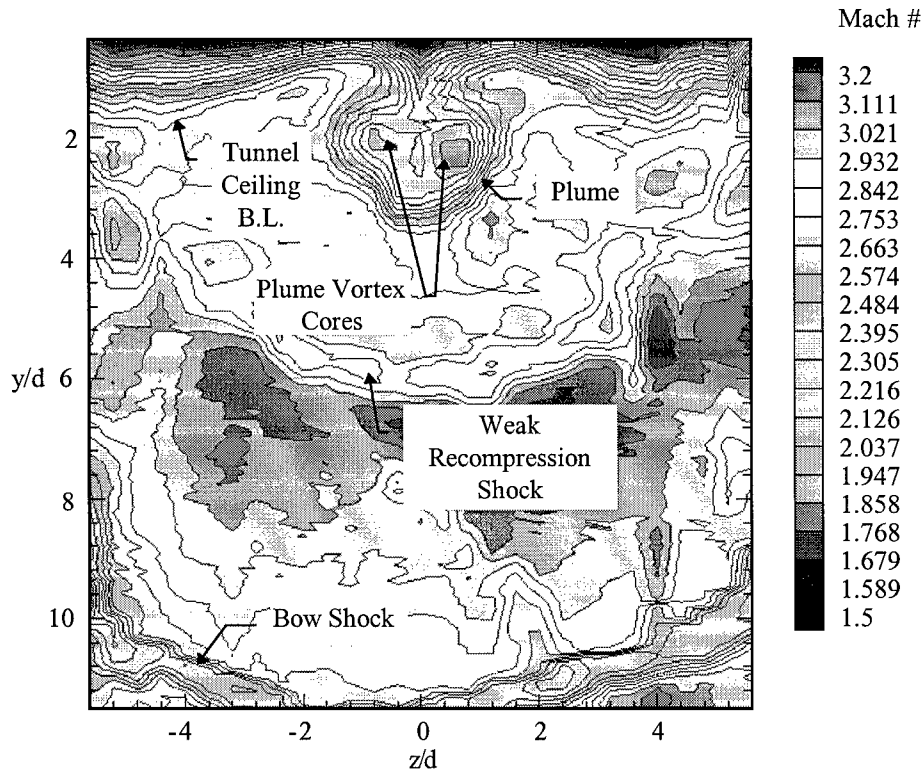


Figure 5.6: Simple Transverse Injection Mach Contour Plot

The  $x/d = 20$  Mach contour plot for the simple transverse injection case is shown in Figure 5.6. This contour plot is scaled to cover a broader range of Mach numbers than the plot used in data processing, section 4.3. The plot is oriented so that an observer would be upstream of the measurement plane and looking in the direction of the flow (i.e. the flow direction is into the page). Basic plume and flow structures are observable in the contour plots. The plume is readily discernible at the center and top of the plot. With the exception of the boundary layer entrainment at the top of the plot ( $y/d < 1.6$ ,  $z/d = \pm 0.8$ ) the plume has the roughly circular shape expected from the cross flow imagery, Figure 5.6. Inside the plume, the twin cores of the counter-rotating vortex pair is visible. The lower Mach number of the vortex cores is caused by the entrainment of the tunnel ceiling boundary layer, which is slower than the injected portion of the plume. Outside the plume, the secondary conical recompression shock is visible

encircling the plume as an arcing structure that peaks at about  $y/d = 6$ . For this particular injection scheme, the recompression shock is weak enough to disappear from the contour plot if the scaling is not selected to highlight it.<sup>26</sup> The large arcing structure seen starting at  $y/d$  of 10 is the edge of the conical shock created by the injection plume. The structure seen spreading from  $y/d$  of approximately 7 to 11 at  $z/d$  of  $\pm 5.6$  is the plume conical shock interacting with the tunnel side wall boundary layer. The tunnel ceiling boundary layer is seen ranging from approximately  $y/d = 1.6$  at the outside edges to  $y/d = 1$  in the plume area, depending upon the level of entrainment the boundary layer is subjected to by the plume.

The results of the plume area based upon the local freestream Mach contours as described in section 4.3.1 are shown in Figure 5.7. The lines at  $y/d = 1$  and  $y/d = 4$  are the respective top boundary and bottom boundaries for the plume area and centroid location search. The four contours collapse into essentially one contour for most of the area, with minor disagreement near the tunnel ceiling boundary layer. Table 5.1 summarizes the area and centroid location results based upon method.

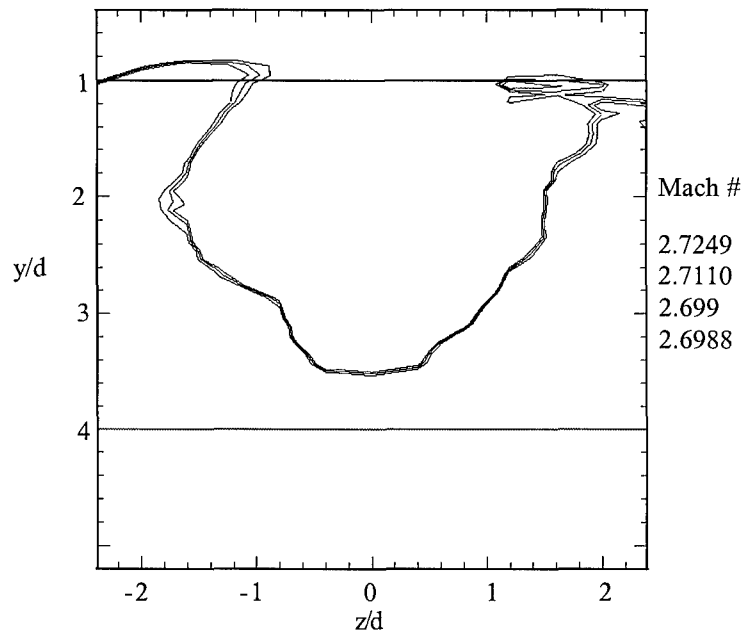


Figure 5.7: Simple Transverse Injection Area Contour Plot

TABLE 5.1  
SIMPLE TRANSVERSE AREA AND CENTROID RESULTS

Area Method	95% Freestream Mach	Area (cm <sup>2</sup> )	Centroid (y/d)
Graphical	2.72	1.058	2.04
Box	2.71	1.006	2.06
Modified Box, y/d=1.2	2.69	0.980	2.07
Modified Box, y/d=1.6	2.69	0.980	2.07
Average	2.70	1.006	2.06

The results for the areas and the centroids are within 7.5% and 1.2% of each other, respectively. This particular case shows excellent agreement between the box and modified box methods, which is consistent with the relatively benign local flow field around the plume. As will be seen for the PME ramps, the presence of the ramp can significantly increase the complexity and number of flow structures at the  $y/d = 20$  measurement location.

### ***5.1.3 Simple Transverse Injector Total Pressure Loss***

The total pressure loss incurred by each of the following PME ramps is based upon the average upstream to local total pressure ratio as detailed in section 4.2. The value of the total pressure ratio for the simple transverse injection is used to normalize the results for relative comparisons. As such the average upstream-to-local total pressure ratio for the simple transverse injection case is 1.24. The value of  $\Pi$  for the simple transverse case is defined as one. The total pressure contour plots for simple transverse injection and each PME ramp are presented in Appendix A.

### ***5.1.4 Simple Transverse Injector Digital Image Quantitative Analysis***

Two types of quantitative analysis were performed on the digital images. The first was the plume boundary and centerline trajectories, as described in section 4.4.1.1. Figure 5.8 is a plot the plume trajectories of the simple transverse injector.



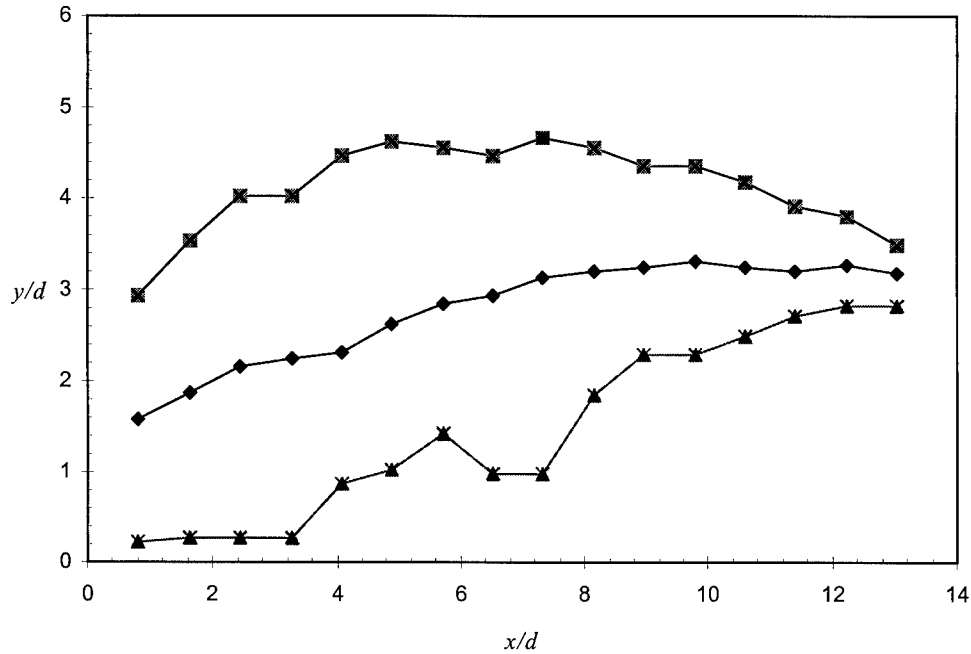


Figure 5.8: Simple Transverse Injector Plume Centerline Trajectory

Recall from section 4.4.1.1 that these traces represent the outer edge, inner edge and the plume centerline. The plume centerline is the average  $y/d$  value of the image pixels at the measurement location that met the plume intensity criteria. The outer and inner traces map the extremes of the data at the measurement location, and as such may reflect a single outlying point. This effect is illustrated at  $x/d$  of seven, where the plume inner boundary shows a sudden drop to  $y/d$  of one. At the eighth and ninth measurement locations, singular seed particles in the boundary layer were counted as part of the plume inner boundary. The plume centerline trajectory does not reflect this drop as the centerline locations at stations eight and nine are a fifty point average, which one outlying point does not significantly alter. Additionally, the first three measurement locations are at the injection port, so the inner boundary lies directly on the tunnel ceiling. Note the data represents only 16 of the 20 axial measurement locations; beyond the 16th location the plume image fades and becomes indiscernible from the background.

The centerline trajectory measures the deepest near-field penetration of the most concentrated portion of the plume. In other words, by  $x/d > 10$  the trajectory represents the center of the thick bottom

portion of the injectant crescent, not the centroid of the plume. For the simple transverse injector, this penetration is to  $y/d = 3.32$  at an  $x/d$  of 9.78. The slope of a best fit line passed through the first eight data points, which is one ramp length downstream of the injector exit, is 0.23. The one ramp length corresponds to the  $x/d$  length of the PME ramp compression faces. The trajectory of the plume centerline is relatively flat after  $x/d$  of 10. Also beyond  $x/d$  of 10, the plume outer and inner boundaries converge rapidly on the plume centerline trajectory. This tapering of the plume with downstream location is caused by the freestream-vortex interaction stripping away the outermost centerline concentration of injectant to the outer side portions of the crescent shaped seeded plume. At this point and further downstream the plume continues to expand and migrate further out into the freestream, as seen in a similar study by McCann and Bowersox.<sup>22</sup>

The second quantitative analysis performed on the digital images is the centerline rate of intensity decay. This provides the most direct measure of mixing between the various PME ramps since, as seen in Figures 5.5 and 5.6, the vortex driven mixing strips away the central core of injectant to the plume periphery. Figure 5.9 show the rate of centerline intensity decay with axial position for the simple transverse injector.

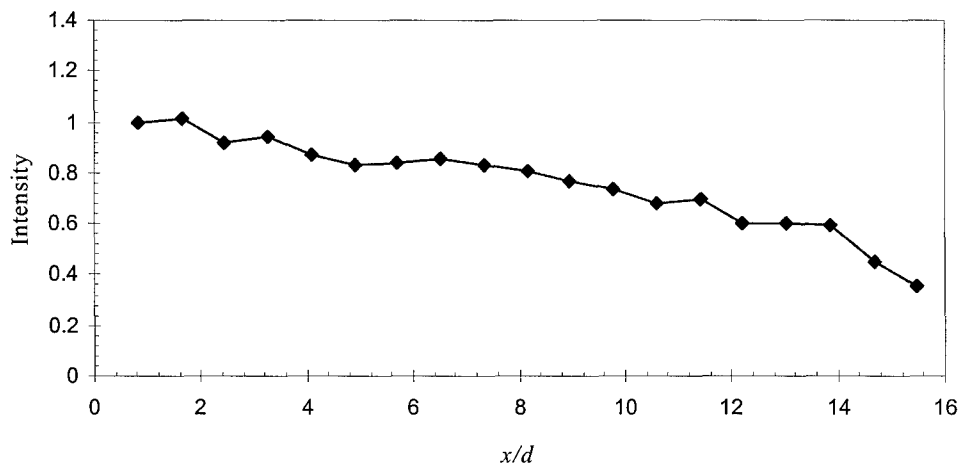


Figure 5.9: Simple Transverse Injector Plume Centerline Average Intensity Decay

The data shows a nearly linear decay of image intensity. A linear regression of this data provides a slope of -0.0372, with a 0.96 correlation. This analysis should not be confused with the far-field decay of

maximum concentration parameter which is frequently used when concentration data is available. The far-field decay of maximum concentration is usually fitted by a power law curve fit, and measure the decay of maximum concentration across the entire plume. This method only considers the centerline plume intensity decay as a measure of how quickly the injectant seed is spread around the plume periphery, with no consideration of overall concentration.

## 5.2 Injector Ramp Group #1: Symmetric Ramps

The injector ramp models in this group share symmetry about the  $y$ - $z$  plane of the tunnel coordinate system. Models SR 1 and SR 2 are of similar shape and have diverging-converging footprint on the tunnel ceiling (shown in Figure 1.1). Model SR 3 presents a straight ramp with a rectangular footprint. The results for the symmetric injector ramps are distinct and representative of the flow mechanics around each model. The height and shape of the shock cones generated by the plume and freestream passage over the PME models clearly reflect the respective geometry of each model.

### 5.2.1 Symmetric Ramp Flow Visualization

The flow visualization accomplished for the symmetric PME ramps is organized such that for a particular flow visualization technique the images corresponding to a specific ramp are grouped together; the discussion follows. In general, the shadowgraph images are of much higher resolution than the simple transverse injector shadowgraph. The parallel oriented laser images provide direct dimensionality of plume structures in reference to the model length and height.

#### 5.2.1.1 Symmetric Ramp Shadowgraph Photography

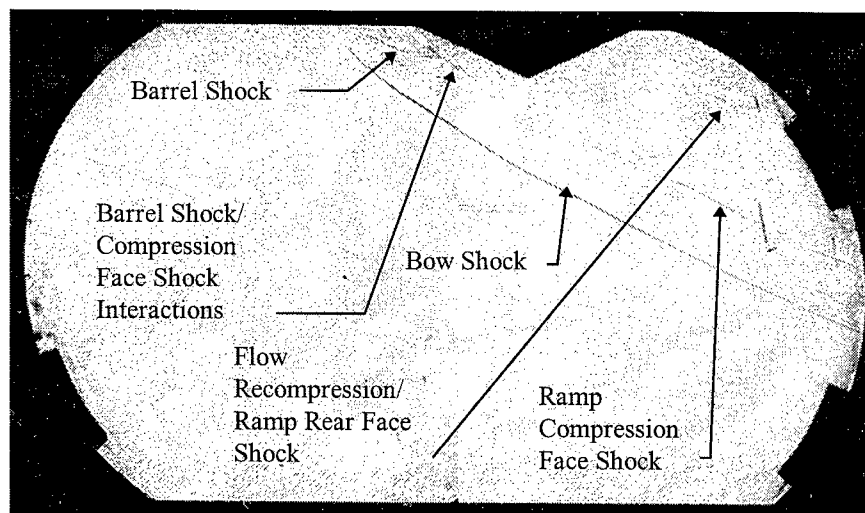


Figure 5.10: Double Diamond Ramp SR 1 Composite Shadowgraph

Figure 5.10 shows the shadowgraph of double diamond ramp SR 1. Several flow structures are present that did not exist for simple transverse injection. In this image, the barrel shock structure is clearly visible at the plume injection port. Also clearly traceable to the front of the compression surface is the secondary compression shock. This secondary shock is due to the local flow impacting on the ramp

compression face. Though not clearly visible in the scanned shadowgraphs, there is also a recompression shock as the main flow rejoins around the vertical portion of the plume. The recompression is faintly visible in the original shadowgraph. Therefore, this ramp configuration has produced three main shocks; a bow shock, a ramp compression shock, and a flow recompression shock. The bow shock initially enters the flow at  $31^\circ$ , then bends to  $25^\circ$  at one third of the image height from the tunnel ceiling. There appears to be an additional flow recompression shock where the ramp rear face meets the tunnel ceiling, which is visible as a faint line intersecting the top inside corner of the upper right window clamp. This shock unites with the main flow recompression shock outside of the boundary layer through a compression fan. The combination of the flow turn shock from transverse injection and the flow turn shock from the rear ramp face and tunnel ceiling strongly affects the shape of the recompression shock as seen in the Mach contour plots for each PME ramp. Finally, a weak series of shocks is faintly visible between the main bow shock and ramp shock.

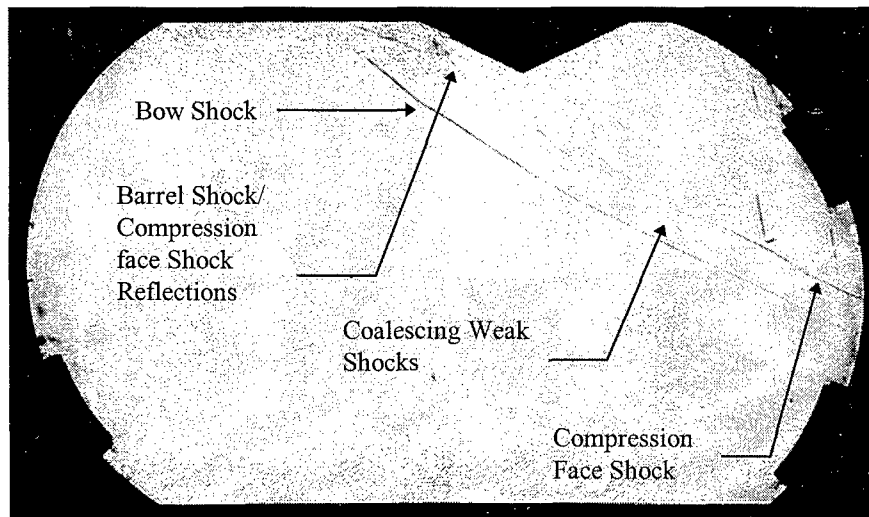


Figure 5.11: Double Cone Ramp SR 2 Composite Shadowgraph

Figure 5.11 shows the shadowgraph of the double cone ramp SR 2. This shadowgraph has many of the same features as Figure 5.10. The bow shock in this image exits the injector port at approximately  $30^\circ$ , then bends to  $25^\circ$  at one third of the image height from the image top. Also of interest, the weak series of shock reflections created by the barrel shock and compression face interactions appears to have coalesced into one shock. Another feature is the relatively closeness of the double cone ramp shock to the main bow shock, and runs parallel to it. The ramp rear face recompression shock is not clearly visible in this image due to the disturbances behind the ramp, but is present.

For both Figures 5.10 and 5.11, the three dimensional relieving effect is obvious. In two dimensional flow, two objects inclined at the same angle (here the plume and the ramp compression face) should produce different shock angles. In particular, the two-dimensional shock should be at a larger angle than the three-dimensional due to the local flow behind the two-dimensional shock being slower than the global freestream. For both the double diamond ramp and the double cone ramp, the ramp compression shock is nearly parallel to the bow shock of the plume. Thus the three dimensional relieving effect was achieved, which allows the compression face shock to lie at a lower angle than it would in a two dimensional situation. The closer position of the secondary shock for the double cone ramp confirms a slightly higher degree of three dimensional relieving than seen for the double diamond ramp.

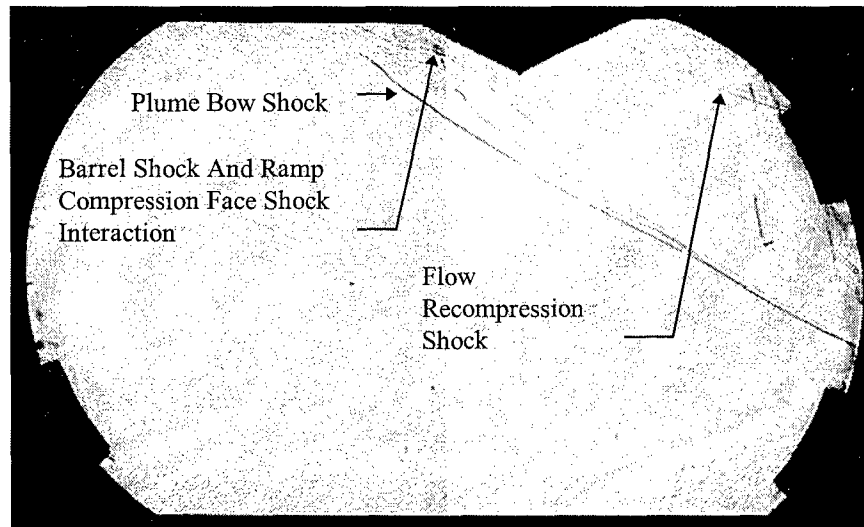


Figure 5.12: Double Ramp SR 3 Composite Shadowgraph

Figure 5.12 is the shadowgraph of the double ramp, SR 3. Here the plume bow shock and ramp compression shock coalesce into basically one structure by the vertical midpoint of the test section. The bow shock of the plume enters the flow at approximately  $33^\circ$ , then turns to  $25^\circ$ , similar to the simple transverse injection bow shock, Figure 5.1. The angle of the double ramp compression shock is approximately  $35^\circ$ . This indicates the desired two-dimensional effect was achieved with this ramp. The

ramp rear face recompression shock is more clearly visible in this image than the previous two as a dark line coalescing from a boundary layer Mach wave fan and passing slightly above the inner top corner of the upper right window clamp.

### 5.2.1.2 *Symmetric Ramp Parallel Oriented Images*

As previously noted, the instantaneous images are best for capturing the unsteady nature of the plume vortex structures. The time-averaged images are useful for describing the flow structures, but also can provide insight into the PME ramp-plume interactions. These images are scaled to 125% of actual size.

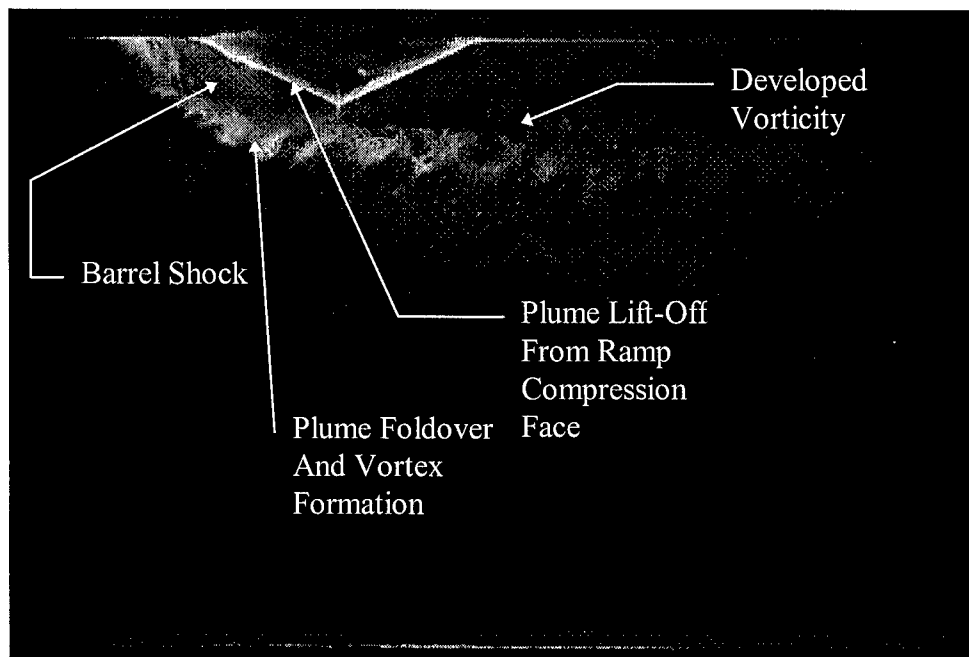


Figure 5.13: Double Diamond Ramp SR 1, Instantaneous Parallel Oriented Laser Image

Figures 5.13 and 5.14 are the instantaneous and time-averaged parallel oriented laser sheet images for the double diamond ramp. In Figure 5.13 the plume exit barrel shock structure is visible, as well as a lift-off from the magnus effect between the counter-rotating vortex cores and the ramp compression face. These features are visible in the time-averaged image, Figure 5.14, though the lift-off effect is partially obscured by accumulated surface flow of the injectant seed. Immediately below the barrel shock, the plume foldover region and axial vortex development are visible. Beyond the foldover region, the plume can be seen to form into a regular helical vortex pattern.

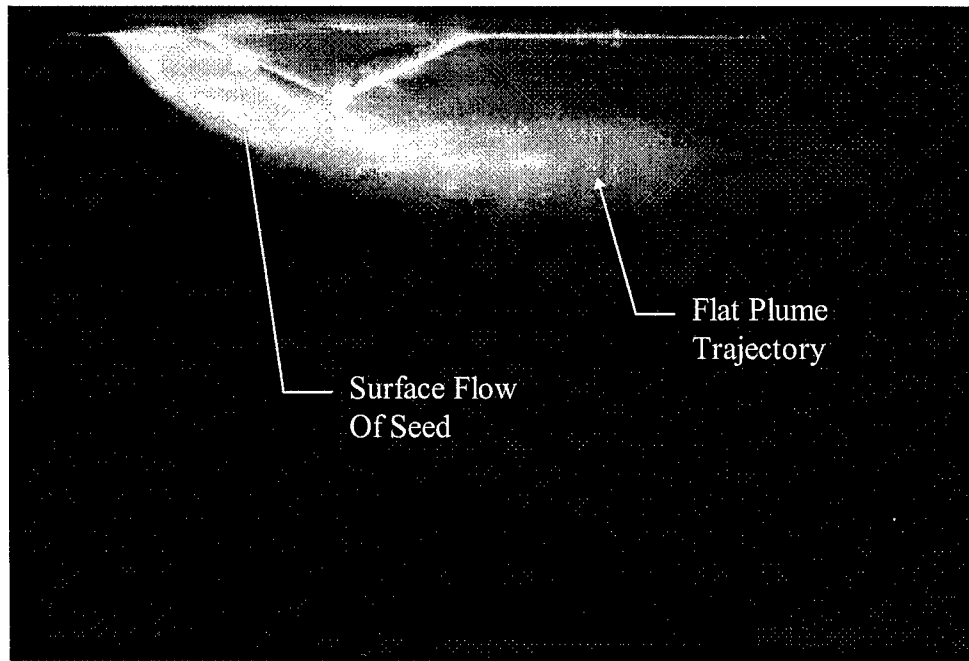


Figure 5.14: Double Diamond Ramp SR 1, Time-Averaged Parallel Oriented Laser Image

A significant difference between the two images is the width of the injectant plume. In Figure 5.13, the instantaneous image, the barrel shock appears to dwarf the plume vortex region in width. In Figure 5.14, the time-averaged image, the width of the plume is approximately the same as the barrel shock. These effects are a result of the exposure time used for each type of image, where the unsteady flow structures are effectively frozen in the instantaneous image, and smeared in the time-averaged image.

In comparison to the instantaneous and time-averaged parallel oriented images in section 5.1.1.2, the primary difference of the double diamond ramp images is the level of seed injected with the plume. The overall shape and tapering trend of the time averaged simple transverse injection and the double diamond ramp images are similar, with the exception of the slightly greater penetration achieved by the double diamond ramp plume.

Visible in Figure 5.14 is the general trajectory trend of the double diamond ramp plume. In particular, the plume can be seen to have a relatively flat trajectory downstream of the ramp rear face. The flat tail trajectory of the double diamond ramp is similar to the tail trajectory of simple transverse injection. The double diamond ramp plume also tapers evenly from the upper and lower boundaries due to the vortex stripping of the plume centerline injectant to the plume periphery.



Figures 5.15 and 5.16 show the instantaneous and time-averaged parallel oriented laser images for the double cone ramp, SR 2. In Figure 5.15, the plume was lightly seeded relative to the other images. The effect of the light seed concentration is a highlight of the flow structures edges. In particular, the flow injection barrel shock is clearly outlined, as well as the surface flow accumulation around the barrel shock.

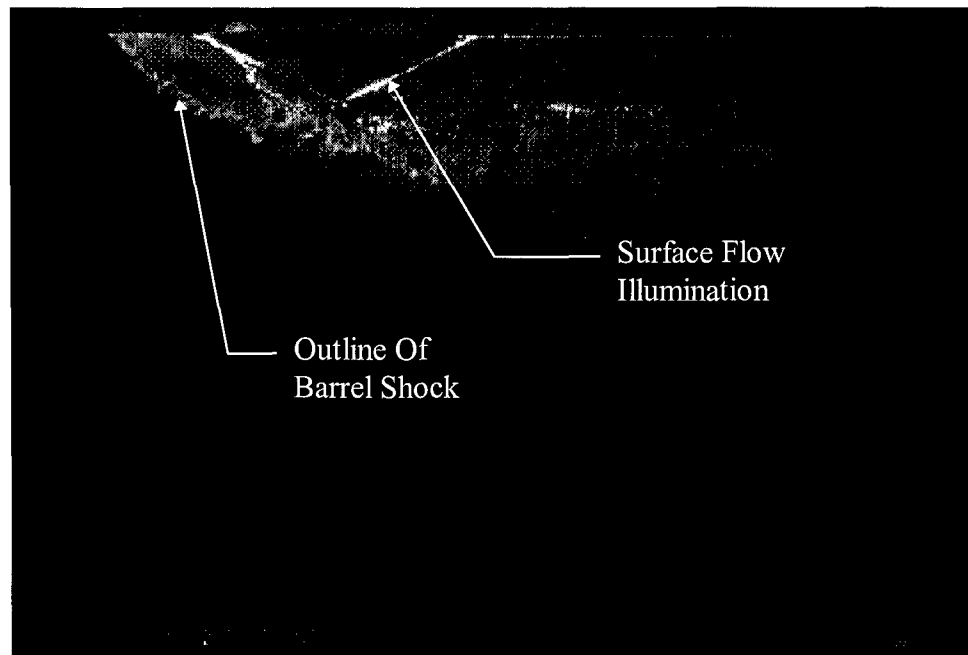


Figure 5.15: Double Cone Ramp SR 2, Instantaneous Parallel Oriented Laser Image

An additional feature visible in Figure 5.16 is surface flow particles exiting the double cone vertex and spreading behind the ramp towards the tunnel ceiling. The bright spot on the ramp rear surface immediately behind the ramp vertex indicates a small recirculation zone is present. In a combustor application, this location could potentially be used for a flameholder.

The plume trajectory visible in Figure 5.16 shows a slight trend back towards the tunnel ceiling. Overall, the plume trajectory from the injector exit to the right side edge of the laser sheet follows a parabolic path. The intensity decay observable towards the rear of the plume indicates the vortices are effectively dispersing the centerline seed particles to the plume periphery.

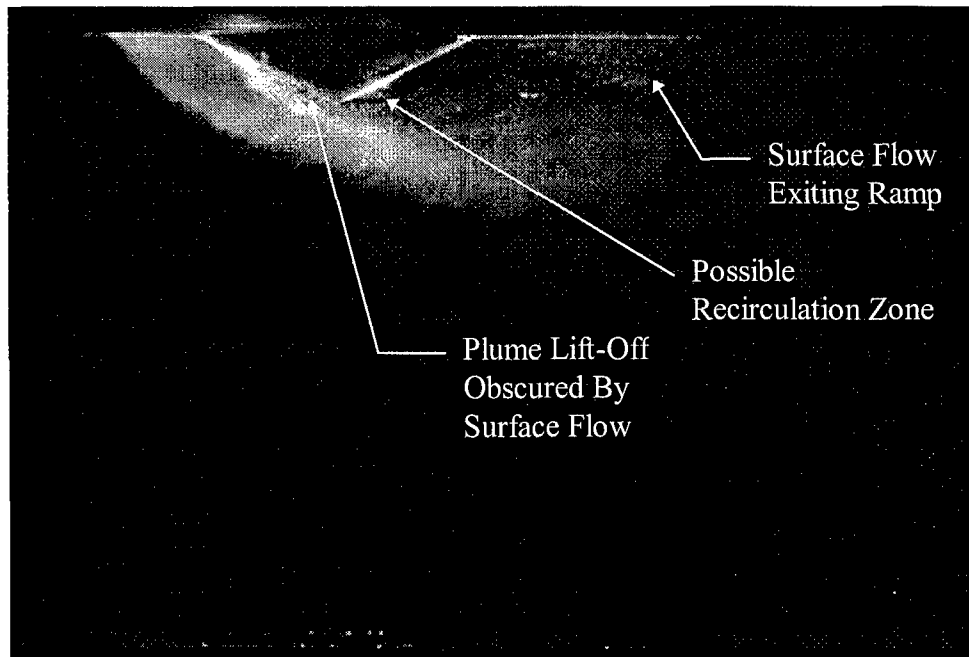


Figure 5.16: Double Cone Ramp SR 2, Time-Averaged Parallel Oriented Laser Image

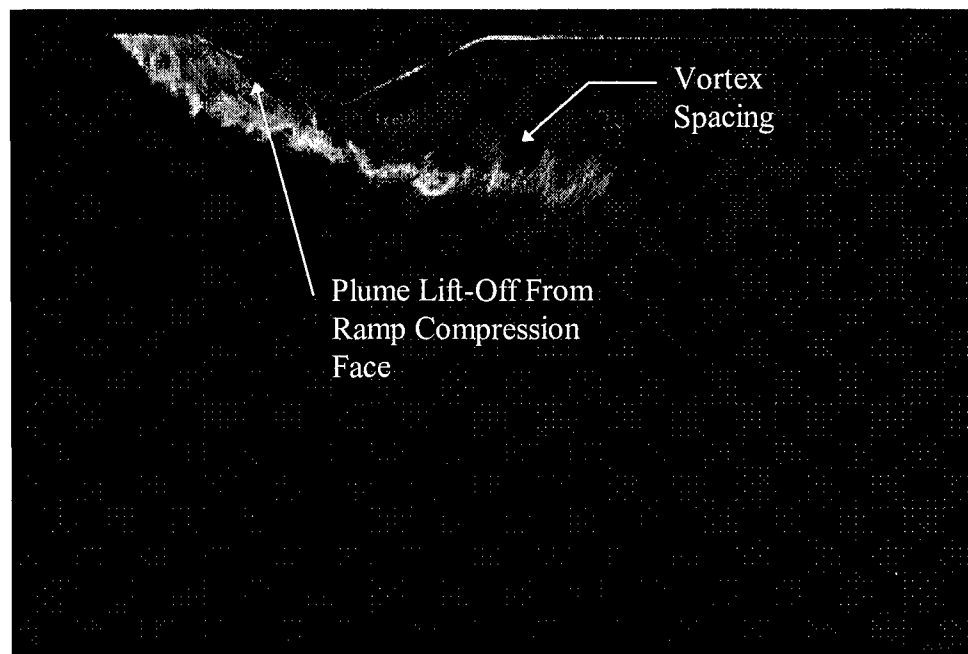


Figure 5.17: Double Ramp SR 3, Instantaneous Parallel Oriented Laser Image

Figures 5.17 and 5.18 show the instantaneous and time-averaged parallel oriented laser images for the double ramp, SR 3. Visible in Figure 5.17 is a clear separation between the plume and the double ramp compression face. This indicates the broad, flat compression face enabled a magnus effect lift-off from the

ramp to enhance local penetration. In Figure 5.18, the magnus effect separation is partially obscured by accumulated surface flow seed particles, but still visible in the bright central core of the plume.

A feature of interest captured in Figure 5.17 is the wider spacing of the vortex helical structure when compared to Figure 5.2 for simple transverse injection. For the same time scale in Figure 5.17 and 5.2, the increase in spacing for the double ramp is a direct decrease in vorticity and rotational velocity. The only vortex enhancing feature in the geometry of the double ramp is baroclinic torque from the ramp compression face. The decrease in vorticity from simple transverse injection for the double ramp is directly related to the strong two-dimensional expansion associated with the ramp vertex.

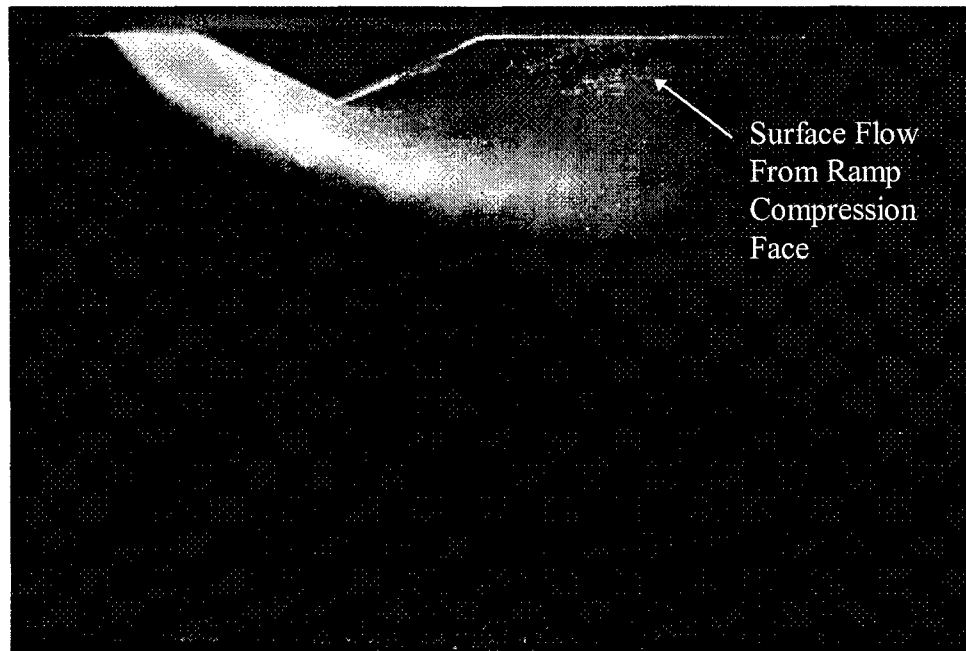


Figure 5.18: Double Ramp SR 3, Time-Averaged Parallel Oriented Laser Image

Figure 5.18 shows the overall plume trajectory trend. The double ramp plume closely follows the simple transverse injection plume, Figure 5.3. The centerline tail of the plume for the double ramp tapers evenly from the upper and lower plume boundaries, and has a relatively flat profile after the ramp vertex. Also visible in Figure 5.18 are large seed particles shed off of the ramp vertex and rear face, as a result of surface flow over the ramp faces accumulation.

### ***5.2.1.3 Symmetric Ramp Cross Flow Oriented Images***

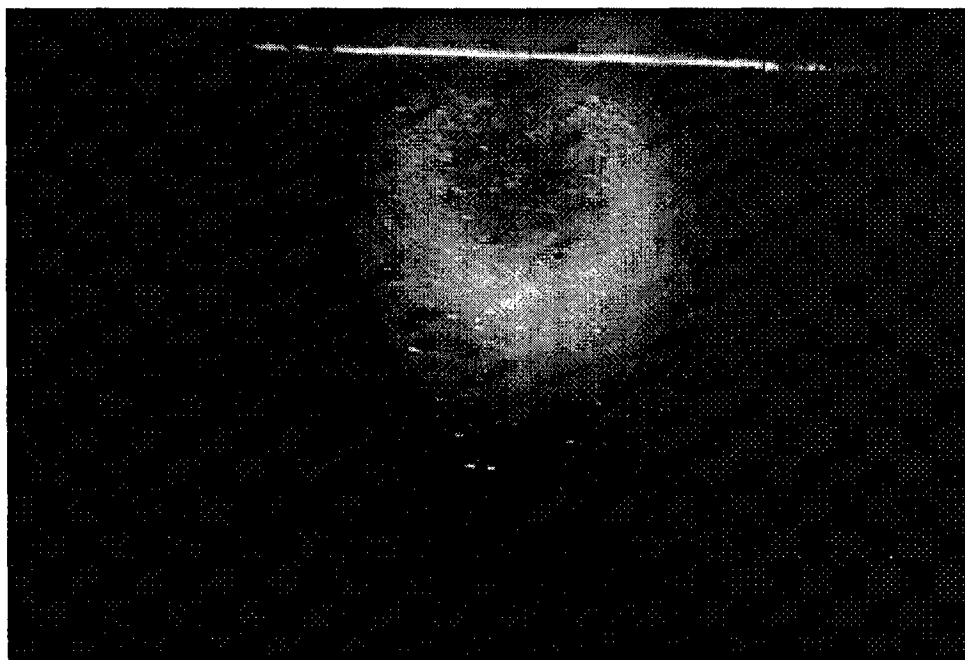


Figure 5.19: Double Diamond Ramp SR 1, Time-Averaged Cross Flow Oriented Laser Image

Figure 5.19 shows the double diamond ramp SR 1 time-averaged cross flow oriented laser image. This image clearly depicts the crescent shaped injected seed plume similar to Figure 5.5 for the simple transverse injection. The action of the plume vorticity on the plume centerline concentration of seed particles has resulted in a fairly even distribution of the image intensity, indicating even mixing throughout the crescent structure.

Figure 5.20 shows the double cone ramp SR 2 time-averaged cross flow oriented laser image. The crescent profile observed in Figure 5.5 for simple transverse injection is visible, though two differences are apparent for the double cone ramp image. The first is the approximately  $15^\circ$  rotation of the plume in the counterclockwise direction. There is no defect or asymmetry in the double cone injector ramp to have induced this rotation, which was observed during two separate test runs.

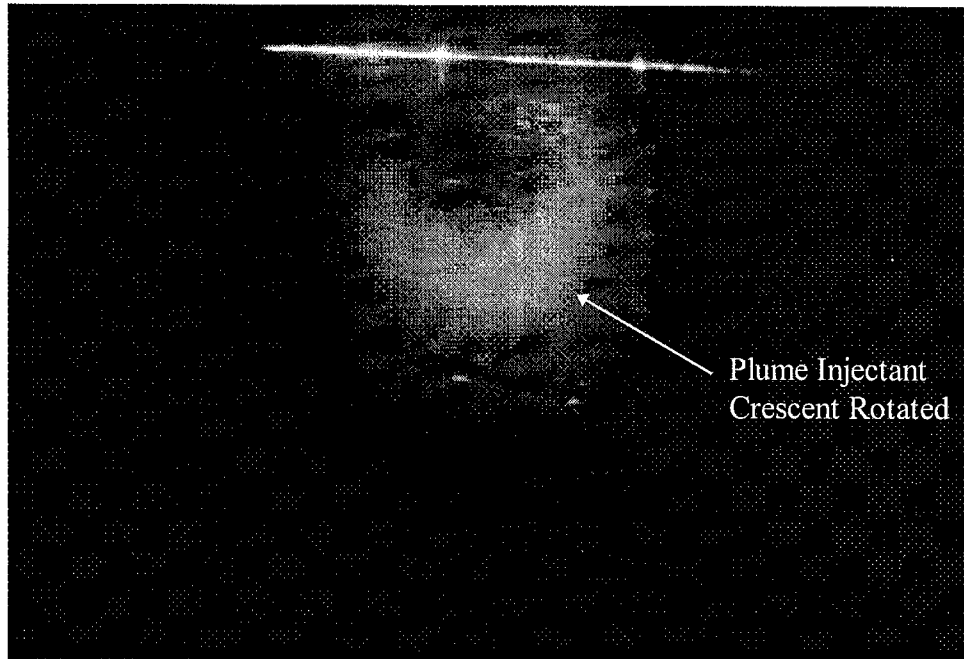


Figure 5.20: Double Cone Ramp SR 2, Time-Averaged Cross Flow Oriented Laser Image

The second difference between the double cone ramp cross flow image and the simple transverse injection is the degree of particles concentration in the plume center. The double ramp plume center is relatively clouded with seed particles compared to simple transverse injection, while the bottom of the crescent is noticeably thicker than the crescent bottom of simple transverse injection. The clouding of the plume center is most likely due to the surface flow particles that have spread off the double cone vertex, seen in Figure 5.16.

Figure 5.21 shows the double ramp SR 3 time-averaged cross flow oriented laser image. Similar to the double cone, the crescent profile observed in Figure 5.5 for simple transverse injection is still visible. However, the differences for the double ramp from the simple transverse injection are increased. The double ramp cross flow image has a greater degree of particle concentration in the plume center than the simple transverse injection. The bottom of the crescent is also noticeably thicker than the crescent bottom of simple transverse injection. Thickening of the crescent bottom is a result of the ramp expansion reduction of vorticity, which lessens the amount of tunnel ceiling boundary layer drawn into the plume core. Without the vortical action drawing the boundary layer into the plume core and distributing the injected seed around the plume boundary, the injected seed remains concentrated in the plume center.

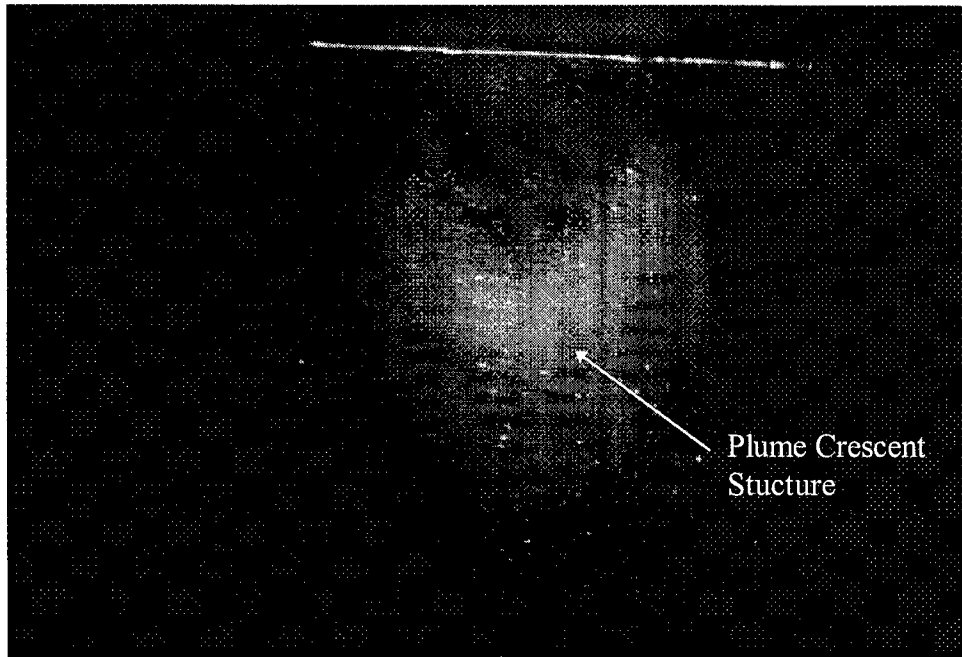


Figure 5.21: Double Ramp SR 3, Time-Averaged Cross Flow Oriented Laser Image

Also visible in this image is a greater separation from the tunnel ceiling for the double ramp plume than the simple transverse injection cross flow image, Figure 5.5. The separation of the plume bottom and the laser reflection from the tunnel ceiling for the double ramp is approximately twice the separation of the simple transverse injection.

### 5.2.2 Symmetric Ramp Mach Contour Plots

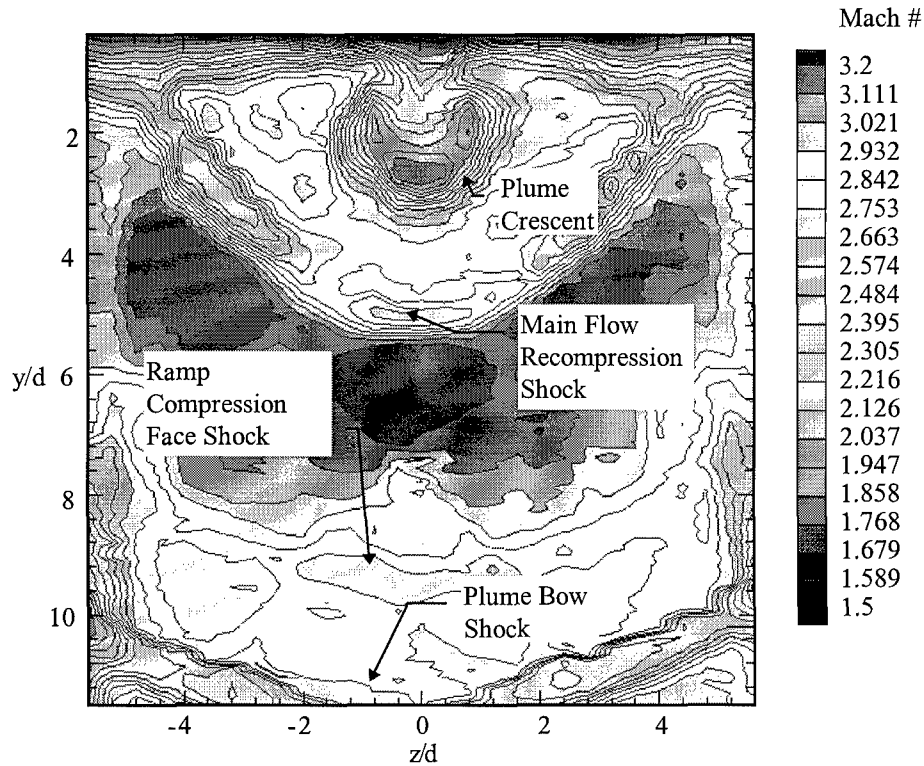


Figure 5.22: Double Diamond Ramp SR 1 Mach Contour Plot

The Mach contour plot for the double diamond ramp SR 1 is shown in Figure 5.22. The structures observed in this plot correlate exactly with the observations made in the flow visualization. Aside from the usual shock and flow structures observed in figure 5.6 for simple transverse injection, there are several unique features of this plot. First, the main flow recompression shock is clearer than observed for the bank injection. The recompression shock has taken on a distinctively triangular appearance as opposed to the more rounded profile of the simple transverse injector. Through the turn combination described in section 5.2.1.1, the main flow recompression shock is strengthened from that seen for the simple transverse injector and the shape of the PME ramp is reflected. The main flow recompression shock also does not penetrate as far into the freestream at  $y/d$  of 5.4 as the simple

transverse flow recompression shock, at  $y/d$  of six. All of these effects described on the flow recompression shock are a result of the ramp geometry, which creates a three dimensional relieving effect as the flow turns away from the ramp rear faces and the tunnel ceiling. Second, the plume core has the previously observed crescent shape, which is nearly identical to the seeded portion of the plume in Figure 5.19. However, the vortex cores are not as obvious as those in the simple transverse injection. The vortex structures appear to have been weakened by the expansion created as the plume passes from the rising front face to the declining rear face. Third, there is an additional shock that is barely distinguishable from the plume bow shock at the image bottom. This is the ramp compression shock, which is almost coincidental with the injection plume bow shock. The lack of resolution between the two shocks is due to the spreading effect the  $10^\circ$  cone-static probe has when passing through shock waves. The ramp compression face shock is relatively weak due to the masking effect of the plume bow shock, which meets one of the objectives for this model.

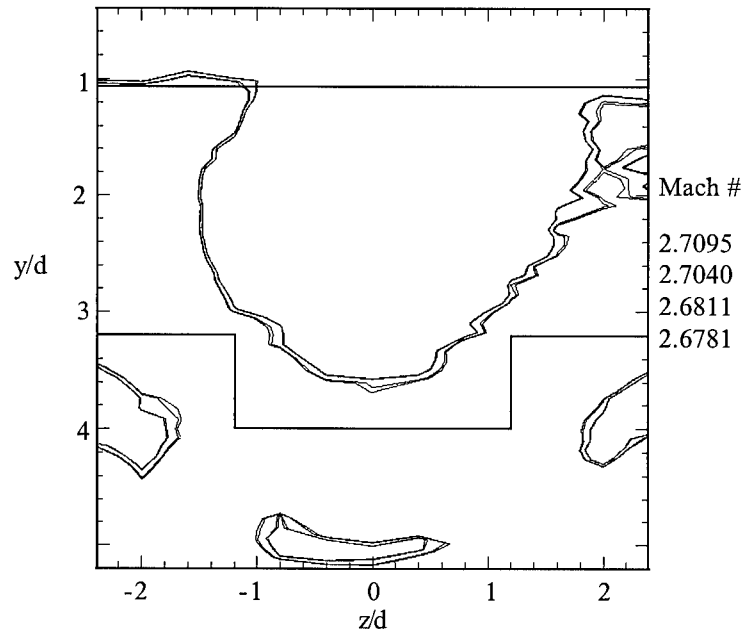


Figure 5.23: Double Diamond Ramp SR 1 Area Contour Plot

Figure 5.23 depicts the Mach contours representing the plume area as determined by the four methods outlined in section 4.3. The top and bottom lines represent the modified search boundaries to avoid counting shock and boundary layer structures as part of the plume. In general, the freestream local



Mach numbers and the Mach contours for the plume area are lower than the simple transverse injection, Figure 5.7. The area contours show relatively close agreement with the exception of the positive  $z/d$  side of the plot. The plume areas and centroids determined by the four methods is summarized in Table 5.2

TABLE 5.2  
DOUBLE DIAMOND RAMP AREA AND CENTROID RESULTS

Area Method	95% Freestream Mach	Area (cm <sup>2</sup> )	Centroid ( $y/d$ )
Graphical	2.70	1.09	2.20
Box	2.71	1.10	2.19
Modified Box, $y/d=1.2$	2.68	1.01	2.17
Modified Box, $y/d=1.6$	2.68	0.99	2.16
Average	2.69	1.05	2.18

The results for the double diamond ramp plume area vary by 9% from highest to lowest. The agreement in the double diamond ramp area results is 2.5% worse than the plume area agreement for simple transverse injection. Comparing Figures 5.22 and 5.23, the four area determination methods appear to have used too high a Mach number in determining the plume boundary, which results in capturing part of the tunnel ceiling boundary layer and the local freestream as part of the double diamond ramp plume. The double diamond ramp plume centroid results are in better agreement, varying less than 2% from highest to lowest. In comparison to Table 5.1, the average double diamond ramp plume area is 9% larger than the simple transverse injection plume area. Also, the average double diamond ramp plume centroid is 6% further into the freestream than the simple transverse injection plume centroid. Depending upon the method used, the double diamond ramp plume area may be artificially enlarged by inclusion of non-plume structures. The double diamond ramp plume centroid results are consistent enough to show greater independence from the method used than the plume area.

Figure 5.24 shows the Mach contour plot for the double cone ramp SR 2. The flow patterns observed in the double cone ramp Mach contour plot are similar to those observed for the simple transverse injection, Figure 5.6. There are several interesting exceptions. The first is the plume vortex core, which differs by having one large elliptical core as opposed to separate vortex cores observed for

simple transverse injection. This may be the result of vortex degeneration due to the strong expansion the plume passes through from the ramp front to rear faces.

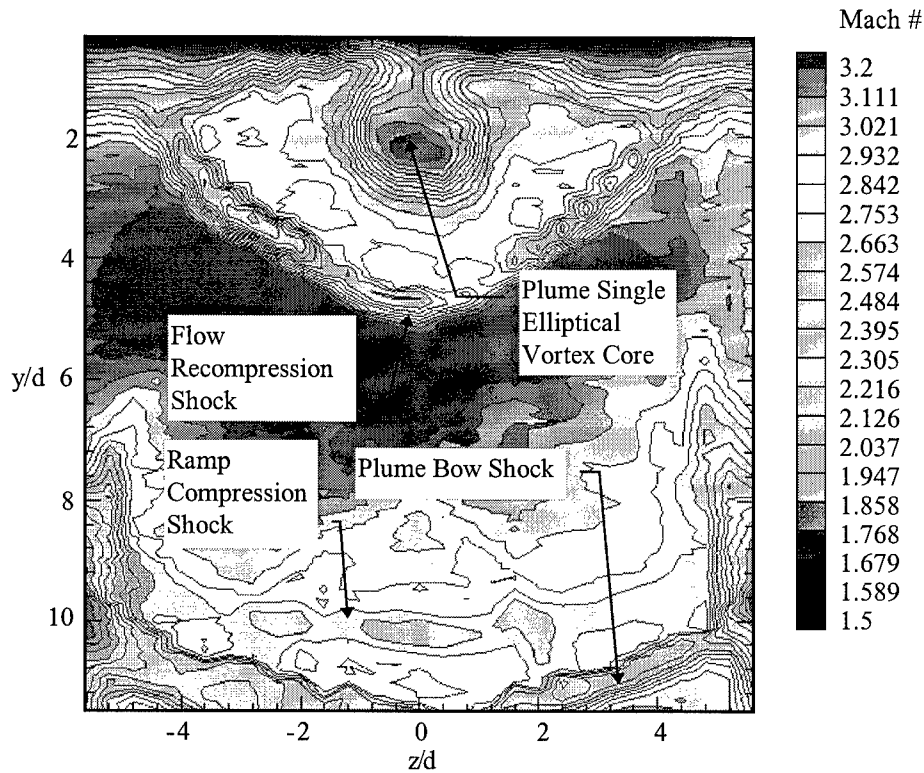


Figure 5.24: Double Cone Ramp SR 2 Mach Contour Plot

A second feature that distinguishes the double cone ramp Mach contour plot from that of simple transverse injection is the ramp face compression shock. This shock was observed lying nearly parallel to the plume bow shock in the double cone ramp shadowgraph, Figure 5.11, indicative of the three-dimensional relieving effect achieved with the conical compression face. Third, the double cone ramp flow recompression shock is more coherent but penetrates less than the simple transverse injection flow recompression shock. The double cone ramp flow recompression shock reaches its maximum height at  $y/d$  of 5.2, compared to six for simple transverse injection.

Figure 5.25 shows the plume area Mach contours of each area determination method for the double cone ramp. The modified search boundaries to exclude the tunnel ceiling boundary layer and

shock structures are indicated. The double cone ramp area contours show close agreement, similar to simple transverse injection. Table 5.3 summarizes the double cone ramp plume area and centroid results by method.

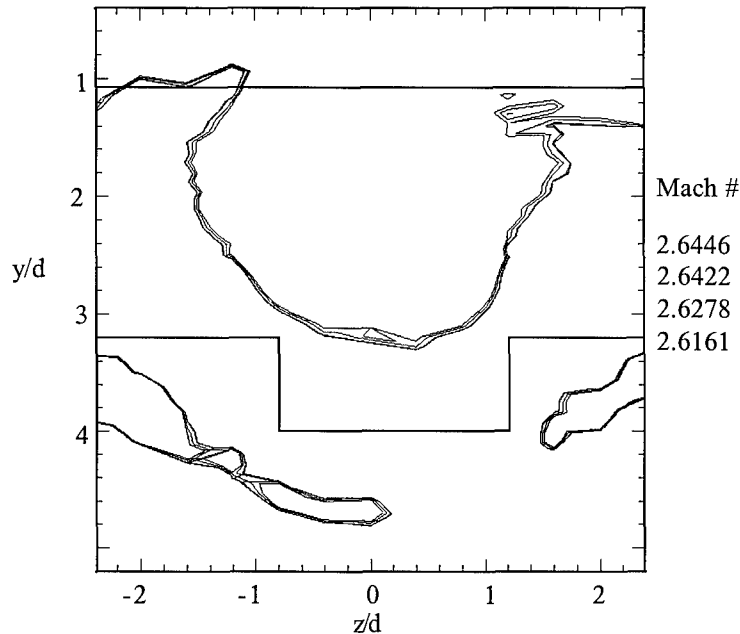


Figure 5.25: Double Cone Ramp SR 2 Area Contour Plot

TABLE 5.3  
DOUBLE CONE RAMP AREA AND CENTROID RESULTS

Area Method	95% Freestream Mach	Area (cm <sup>2</sup> )	Centroid (y/d)
Graphical	2.64	0.99	2.09
Box	2.64	0.98	2.10
Modified Box, y/d=1.2	2.61	0.90	2.11
Modified Box, y/d=1.6	2.63	0.94	2.10
Average	2.63	0.95	2.10

The results for the double cone ramp plume areas and centroids vary by 6% and less than 1% respectively from highest to lowest. Both modified box methods result in lower area Mach number contours due to inclusion of some tunnel boundary layer regions in the local freestream calculation (recall the modified box methods do not use a rejection criteria). The centroids are in excellent agreement, which indicates the double cone ramp plume contours are highly concentric. The different Mach contours

selected by the four area determination methods therefore are simply different depths of the same plume structure, analogous to peeling an onion.

A comparison to Table 5.1 reveals the double cone ramp plume average area is 5% smaller than the simple transverse injection plume average area. The average double cone ramp plume centroid is 2% further into the freestream than the simple transverse injection plume average centroid. The lower area and approximately same centroid penetration between the double cone ramp and simple transverse injection indicates that whatever magnus effect lift-off from the ramp surface occurs is negated by the plume expansion around the front to rear faces of the double cone ramp. The double cone ramp design was also not intended to enhance vorticity, so the negative effect of expansion on the vortex structures results in vortex core breakdown.

Figure 5.26 shows the Mach contour plot for the double ramp SR 3. The vortex core of the double ramp differs substantially from the simple transverse injection vortices. The vortex core region is nearly circular, and appears more as a streamtube into the page than a twin vortex core system. The strong two-dimensional expansion from front to rear of the double ramp has resulted in significant vortex structure breakdown. A similar indication of the vortex breakdown was observed in section 5.2.1.3, Figure 5.17.

The flow recompression for the double ramp shock reflects the frontal profile of the double ramp. The double ramp flow recompression shock has a relatively flat midsection, and steeper sloped sides. This pattern, the flow shock reflecting the frontal profile of the PME ramp, is observable in all of the PME ramp Mach contour plots.

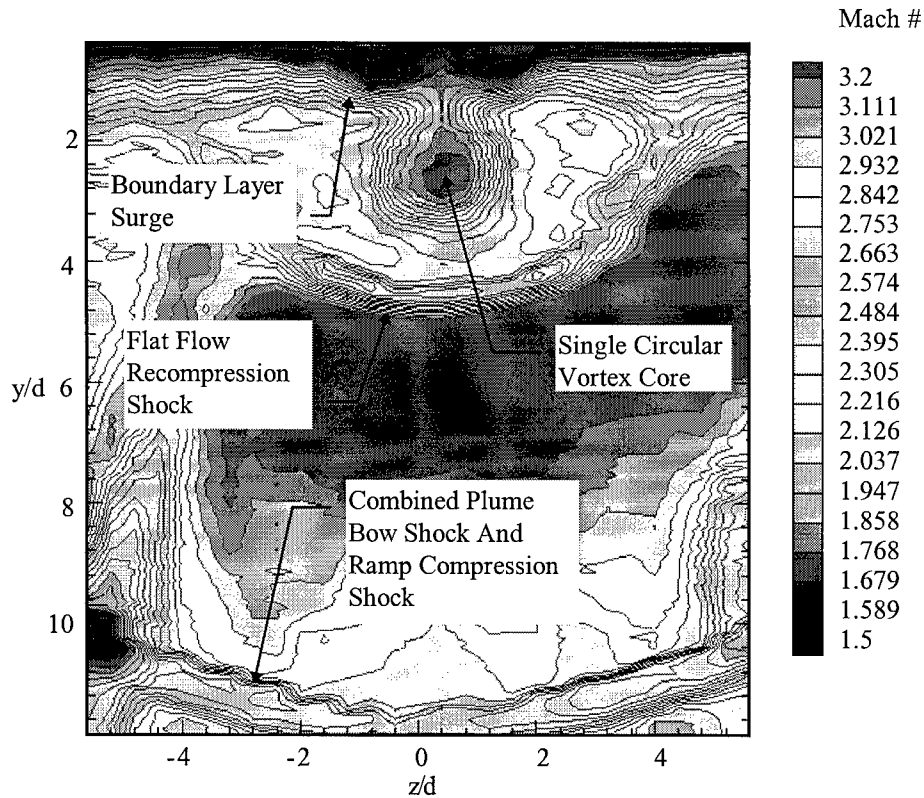


Figure 5.26: Double Ramp SR 3 Mach Contour Plot

The two-dimensional aspect of the double ramp is observed in the combined bow shock and ramp compression face shock. The masking effect achieved by the plume bow shock for the double ramp compression face is substantially greater than the effect achieved for the previous two symmetric ramps. At the mean flow measurement location of  $x/d = 20$ , the two shocks have become collinear. The strength of the combined bow plume and compression face shocks, indicated by the Mach contour levels, is stronger than the simple transverse injection, Figure 5.6.

Annotated in Figure 5.26 is a unique structure identified as the boundary layer surge. This flow structure appears to be ramp generated vorticity from the double ramp. Since the double ramp at  $4d$  is relatively wide compared to the developing plume, a magnus effect lift-off was expected from the broad compression face. The double ramp compression face also acts as a ramp spillage vortex generation device with the main flow passing around the plume and along the ramp side. Due to the width of the

double ramp, the vortices generated by ramp spillage are separated far enough apart to prevent a magnus effect lift-off from developing. Ramp spillage vorticity essentially forms in the tunnel ceiling boundary layer, where the separation of the vortex cores prevents migration away from the wall. The boundary layer surge created by the ramp spillage vorticity does not appear to enhance mixing.

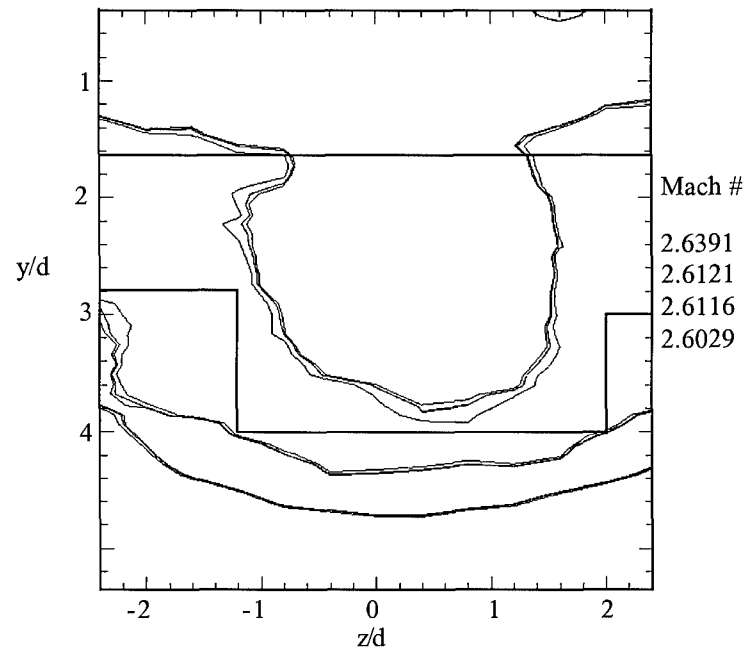


Figure 5.27: Double Ramp SR 3 Area Contour Plot

Figure 5.27 shows the results of the area determinations for the double ramp. These contours are on average 0.9 Mach lower than the contours for simple transverse injection, Figure 5.7. Three of the methods are in excellent agreement. The fourth, the box method, selected a higher Mach contour for area based upon the tunnel ceiling boundary layer rejection Mach criteria detailed in section 4.3.1.2. Despite the difference in the plume boundary Mach contour, the four methods all capture the same basic plume shape. Table 5.4 summarizes the area and centroid results by method for the double ramp.

TABLE 5.4  
DOUBLE RAMP AREA AND CENTROID RESULTS

Area Method	95% Freestream Mach	Area (cm <sup>2</sup> )	Centroid (y/d)
Graphical	2.60	0.68	2.61
Box	2.64	0.77	2.65
Modified Box, y/d=1.2	2.61	0.71	2.63
Modified Box, y/d=1.6	2.61	0.69	2.62
Average	2.62	0.72	2.63

The variation between methods from highest to lowest is 12% for the areas and 1.5% for the centroids. The disparity in the area computations is a result of the higher plume boundary Mach number of the box method. The centroid results are in good agreement, indicating again that the area results have found different concentric layers of the same flow structure.

The average plume area for the double ramp is 30% lower than the simple transverse injection average area. The average centroid height for the double ramp is 28% greater than the average centroid of the simple transverse injection. These results are not necessarily contradictory. The plume area defined from the Mach contours measures the size of the plume vortex structures, not concentration or injectant dispersion. Compared to simple transverse injection, the double ramp area results indicate the vorticity of the plume has been diminished substantially. However, penetration was clearly enhanced by a magnus effect lift-off from the ramp face.

### 5.2.3 Symmetric Ramp Total Pressure Loss

TABLE 5.5  
SYMMETRIC RAMP GROUP TOTAL PRESSURE LOSS

PME Ramp	Average Total Pressure Ratio	$\Pi$
Double Diamond Ramp, SR 1	1.29	0.95
Double Cone Ramp, SR 2	1.36	0.91
Double Ramp, SR 3	1.49	0.83

Table 5.9 describes the total pressure losses for the extended ramp group based upon the average total pressure loss ratio. The results reflect the frontal profiles of the respective ramps. The double

diamond ramp, SR 1, has the lowest frontal area presented to the flow, resulting in less obstruction and relatively weaker shocks than the progressively larger aspect double cone ramp and double ramp.

#### 5.2.4 Symmetric Ramp Digital Image Quantitative Analysis

Figures 5.28 to 5.33 are plots of the plume centerline trajectories and centerline intensity decay for symmetric ramps SR 1, SR 2 and SR 3. These plots are oriented as horizontal mirror images of the original plume images, where  $y/d$  of zero is the tunnel ceiling.

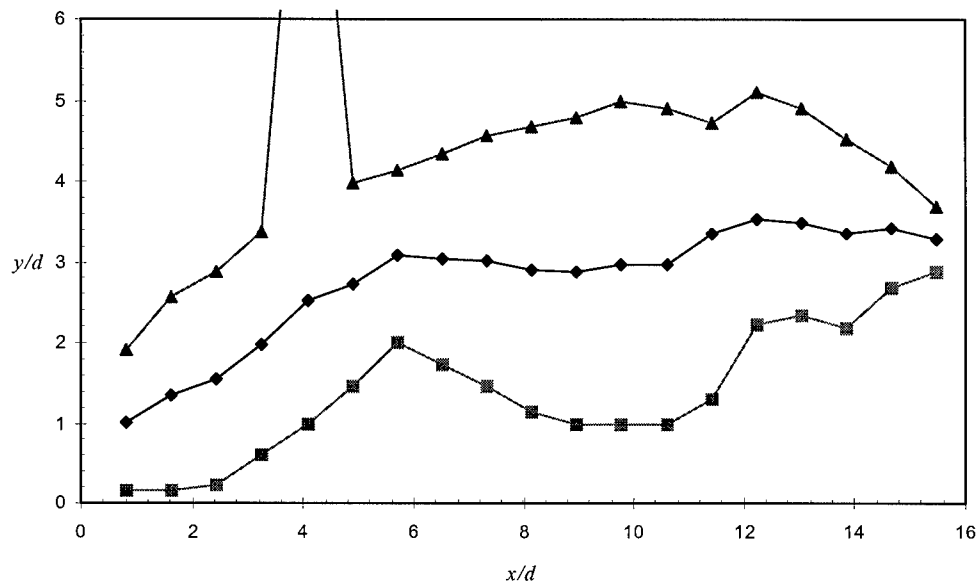


Figure 5.28: Double Diamond Ramp SR 1 Plume Centerline Trajectory

Figure 5.28 is the centerline trajectory plot of the double diamond ramp, SR 1. The lower trace represents the inner plume boundary on the tunnel ceiling side and the higher trace is the plume outer boundary penetration into the freestream. At  $x/d$  of 4.07 a large spike is visible, resulting from a single seed particle approximately  $10 d$  into the freestream. This single seed particle has a negligible effect on the centerline trajectory, which is an average of all points at the measurement plane above the threshold intensity level described in section 4.4.1.1.

The slope of the first eight centerline data points tracks the trajectory of the plume in contact with or directly below the compression ramp face, and provides a measure of the lift-off effect achieved



from the compression face. For the double diamond ramp, the slope of the first eight data points is 0.34. This slope is a 48% increase over the first eight point slope for simple transverse injection. The maximum  $y/d$  penetration of the plume centerline is 3.53 at  $x/d$  of 12.2, compared to  $y/d$  of 3.32 at  $x/d$  of 9.78 for the simple transverse injection centerline maximum penetration. An enhancement in penetration was achieved with the faceted face

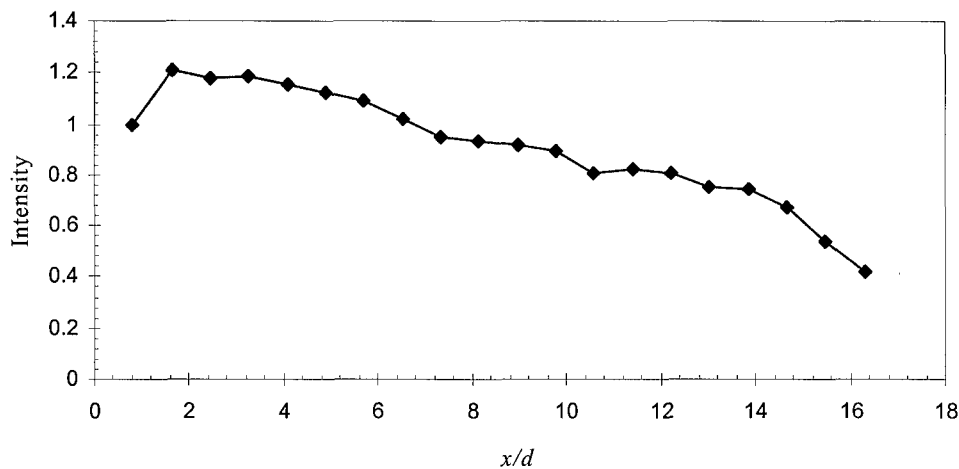


Figure 5.29: Double Diamond Ramp SR 1 Plume Centerline Average Intensity Decay

Figure 5.29 is the centerline average intensity decay plot of the double diamond ramp, SR 1. This plot is similar in profile to the simple transverse injection centerline average intensity decay plot. The overall slope of the double ramp intensity decay plot is -0.043, which is an 11% increase to the simple transverse injection decay rate, -0.037. The higher decay rate indicates the injectant spreading to the plume periphery is enhanced by the presence of the ramp.

Figure 5.30 is the centerline trajectory plot of the double cone ramp, SR 2. The variations of the plume inner boundary represented by the plot bottom trace are due to the surface flow seed particles shed by the ramp. The slope of the first eight data points of the double cone ramp centerline trace is 0.38, a 65% increase over the simple transverse injection initial slope. The maximum centerline  $y/d$  penetration for the double cone ramp occurs at  $x/d$  of 4.9, with a  $y/d$  value of 3.34. This maximum penetration height is essentially the same as the simple transverse injection. However, for the double ramp the maximum

now occurs a ramp length upstream of the simple transverse injection maximum  $y/d$ . After the maximum  $y/d$  is achieved for the double cone ramp, the centerline trace shows a decline at a slope of -0.04 for the remaining two thirds of the plot. In contrast, the simple transverse injection centerline has a gradual rise up to the maximum  $y/d$  penetration of the plume centerline.

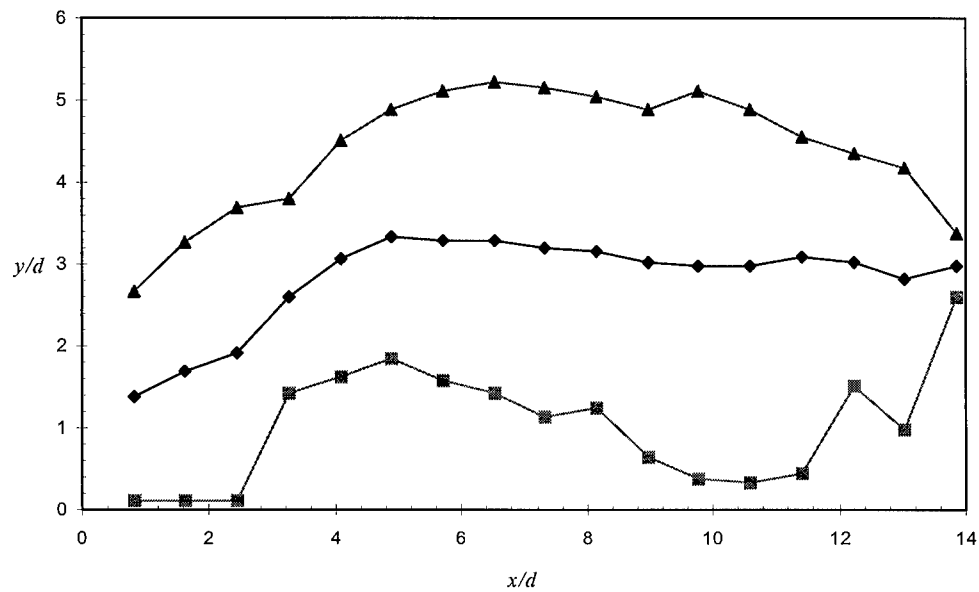


Figure 5.30: Double Cone Ramp SR 2 Plume Centerline Trajectory

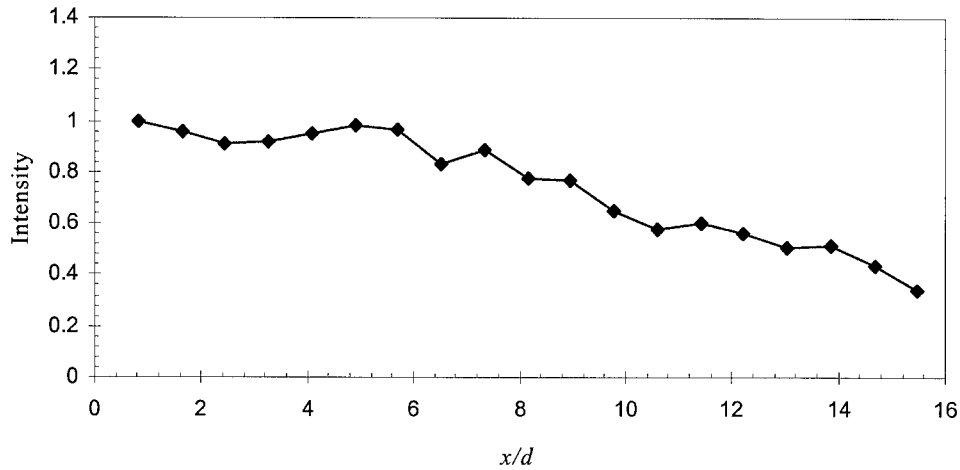


Figure 5.31: Double Cone Ramp SR 2 Plume Centerline Average Intensity Decay

Figure 5.31 is the plume centerline average intensity decay for the double cone ramp, SR 2. The overall slope of the trace is -0.044. The double cone ramp slope is an 18% increase in decay over the simple transverse injection decay. The increase in decay rate is attributable to the core vortex action on the plume centerline seed particle concentration. An increase in decay rate may also be attributable to the surface flow shedding observed in Figure 5.16. Since each image was normalized by the intensity of the image at the injector exit, any decrease of injected seed concentration is reflected as intensity decay. Figure 5.16 shows an increase in illuminated image area over the last few quantitative measurement stations from the spread of ejected ramp vertex surface flow particles along the tunnel ceiling boundary layer. By spreading the available seed across a larger area, the overall average intensity of the image is decreased.

Figure 5.32 is the centerline trajectory plot of the double ramp, SR 3. The slope of the centerline trace first eight points is 0.45, which is double the initial slope of the simple transverse centerline plot. The significant enhancement to plume penetration is a result of the ramp compression face inducing a magnus effect lift-off in the plume vortices. The general shape of the double ramp centerline trace is similar to the simple transverse injection in that the maximum  $y/d$  of the plume centerline occurs within the last few measurement stations of the image. The maximum  $y/d$  of 3.80 for the double ramp occurs at

$x/d$  of 13, compared to  $y/d$  of 3.32 at  $x/d$  9.78 for simple transverse injection. The inner and outer plume boundary traces show a similar convergence on the plume centerline trace as the simple transverse injection, however, the plume inner and outer boundaries are slightly larger for the double ramp.

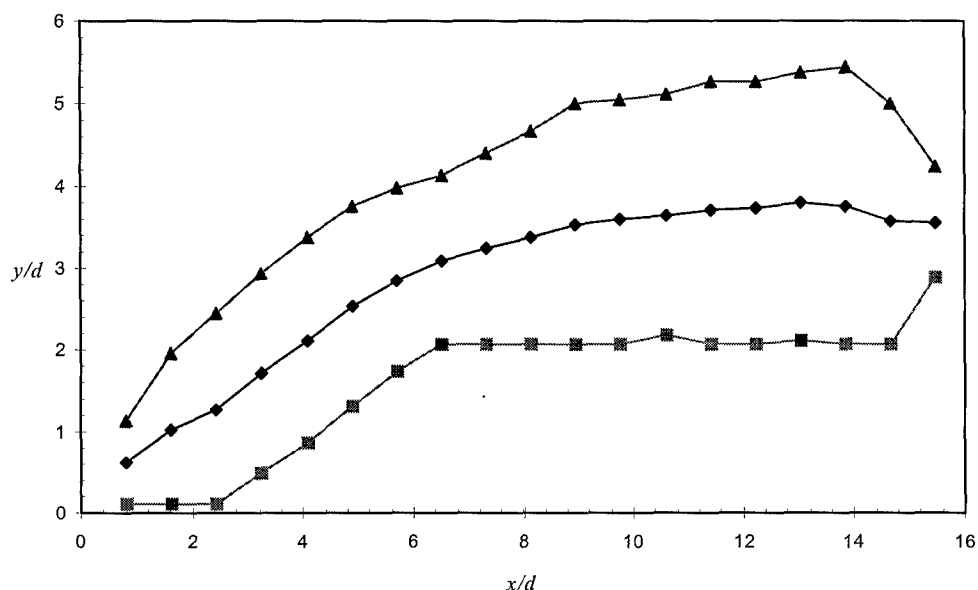


Figure 5.32: Double Ramp SR 3 Plume Centerline Trajectory

Figure 5.33 is the plume centerline average intensity decay for the double ramp, SR 3. The overall slope of the trace is -0.051. The double ramp slope is an 37% increase in decay over the simple transverse injection decay. Part of the increase in decay rate is attributable to the core vortex action on the plume centerline seed particle concentration. However, the vortex core structures as measured in the area contour plot for the double ramp, Figure 5.27, are significantly smaller than simple transverse injection. Figure 5.18, the time-averaged parallel oriented laser image for the double ramp, shows considerable seed spread between the plume inner boundary and the tunnel ceiling. Though not intense enough to affect the plume centerline trajectory, the quantity of seed in the boundary layer does reduce the overall image intensity.

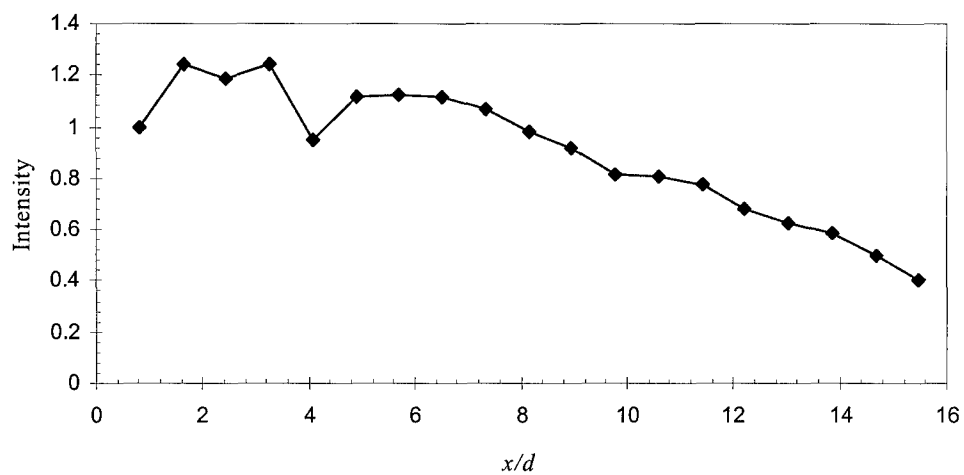


Figure 5.33: Double Ramp SR 3 Plume Centerline Average Intensity Decay

### 5.3 Injector Ramp Group #2: Extended Ramps

This PME ramp group was designed to test a modification to the simple ramp geometry by adding a tapering extension beyond the compression face, Figure 1.2. Models ER 2 and ER 3 differ in ramp sweep angle which results in a truncated trailing edge for ER 2 and a sharp trailing edge for ER 3. Model ER 1 and the double diamond ramp SR 1 share the same compression face geometry. Instead of a symmetric rear face like ramp SR 1, the extended diamond ramp ER 1 has an extension that crosses beyond the mean flow measurement plane. As should be expected for such similar geometries, the results for truncated ramp ER 2 and tapered ramp ER 3 share many features. PME ramp ER 1 provides interesting qualitative results.

#### 5.3.1 Extended Ramp Flow Visualization

The flow visualization results are presented as in section 5.2.1. For each PME ramp, the images are organized by type, starting with shadowgraph photography. The salient features of the shadowgraphs are highlighted and annotated. The parallel oriented and cross flow oriented laser planar images are next examined.

##### 5.3.1.1 Extended Ramp Shadowgraph Photography

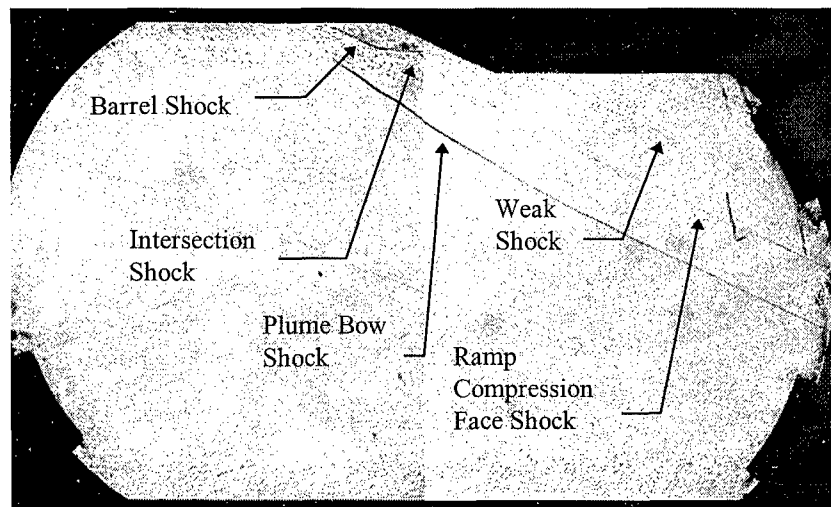


Figure 5.34: Extended Diamond Ramp ER 1 Composite Shadowgraph

In Figure 5.34, the plume bow shock is seen to start at approximately  $33^\circ$  and then turns to approximately  $25^\circ$  as it descends through the top third of the image. The angles and locations of bends in

the bow shock are nearly identical to the simple transverse case, Figure 5.1. Since the flow is fully supersonic in this region, there is no mechanism for the shape of the ramp behind the plume to be broadcasted upstream and affect the bow shock shape. It is conceivable that the bow shocks would differ further downstream as the ramp unique structure (shocks and expansions) interacted with the bow shock. The limited height of the test section prevents these effects from being observed. This image also shows several shock structures that are not seen in the simple transverse injection case, Figure 5.1. A shock can be seen emerging from the base of the compression face. There is also a shock reflection where the barrel shock and ramp compression face shock intersect. This shock is observable as a thin, weak line that appears to intersect the bottom of the ramp compression face. These shock structures will provide baroclinic torque to the plume and enhance the vorticity. A third shock annotated in Figure 5.34 as the weak shock is unique to the extended diamond shadowgraph. The exact origin of the shock is not observable because the ramp extension intersects the shock. The weak shock does not appear to be part of the barrel shock-compression face reflection. A possible source for the weak shock is a recompression of the plume. If the magnus lift-off effect is not substantial, components of the plume in the foldover region (identified in the simple transverse instantaneous parallel oriented image, Figure 5.2) that curve back up towards the tunnel ceiling would impinge upon the ramp extension creating the weak shock. The presence of this shock therefor indicates the diamond ramp compression face does not enhance penetration significantly from the simple transverse case. Another significant feature of this image is the apparent lack of a downstream plume recompression shock. The missing recompression shock is logical since the large extension prevents any area for the flow to coherently recompress around the plume, again confirming the lack of a lift-off effect from this ramp configuration.

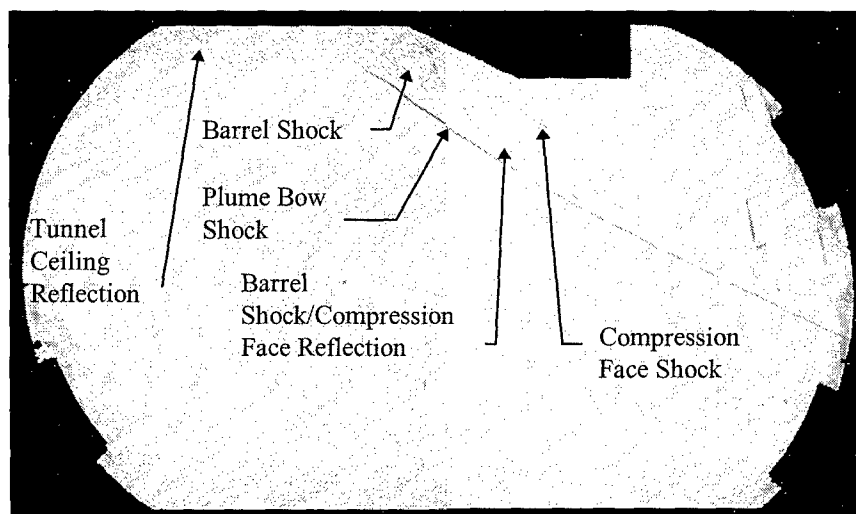


Figure 5.35: Truncated Extended Ramp ER 2 Composite Shadowgraph

Figure 5.35 is the shadowgraph for the truncated extended ramp, ER 2. The bow shock angles observed in this image are  $33^\circ$  at the origin, and  $25^\circ$  after the bend which results in an identical profile to the one observed for the simple transverse injection, Figure 5.1. The ramp compression face shock and barrel shock-compression face shock reflection are at slightly higher angles than the bow shock, which is due to the two-dimensional effect of the flat compression face. These shocks eventually run into the bow shock by the right edge of the image. Favorable baroclinic torque of some degree will be generated by the plume passage through these combined shock structures. Also of interest in this image is the lack of a flow recompression shock from the main flow passing over the rear edge of the ramp and turning towards the tunnel ceiling. In this image the shock is not visible due to the separation region behind the ramp, which disturbs the flow and obscures most flow structures. The lack of discernible flow features in the image after the end of the ramp indicate the design achieved one of its objectives. The truncated trailing edge was intended to provide a recirculation region as well as create an expansion before the flow passing around the sides of extended ramp is shocked upon rejoining. The absence of a visible shock from the side flows rejoining immediately downstream of the ramp rear face in the local region of the expansion confirms this effect. In effect the expansion delays or weakens the shock created as the side flows rejoin. Since this shock is nearly parallel to the plume, the alignment of the shock pressure gradient and the plume-air interface density gradient may not be conducive to producing baroclinic torque. The tunnel ceiling reflection was due to a minor misalignment in the shadowgraph light source.



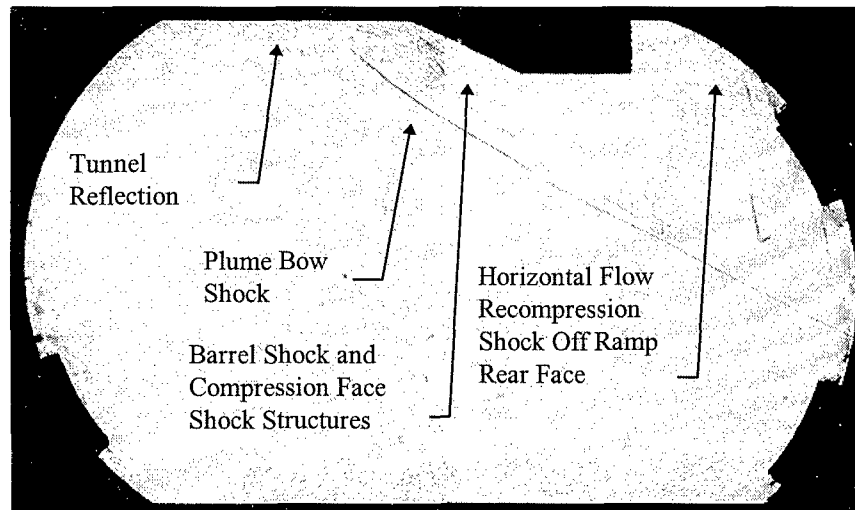


Figure 5.36: Tapered Extended Ramp ER 3 Composite Shadowgraph

Figure 5.36 is the shadowgraph for the tapered extended ramp, ER 3. The bow shock created by this image follows the  $33^{\circ}$ - $25^{\circ}$  pattern established in the previous shadowgraphs. The barrel shock and compression face shocks in this image are similar to those observed for the truncated extended ramp, ER 2 (Figure 5.35). Also similar to the ER 2 shadowgraph is the apparent lack of the recompression shock as the flow turns back towards the tunnel ceiling after clearing the ramp extension. A particular feature of the tapered ramp shadowgraph is the relatively sharp shock annotated as the flow recompression shock in Figure 5.36. The source of this shock stems from the sharp trailing ramp edge. As the air flowing along the ramp sides passes the ramp rear edge, the two airstreams with components into and out of the page collide, producing a sharp shock. This shock is observable (and noted) in the tapered ramp Mach contour plot, Figure 5.50. This shock runs nearly parallel to the plume, and in this non-intersecting orientation should not induce baroclinic torque in the plume.

### 5.3.1.2 *Extended Ramp Parallel Oriented Images*

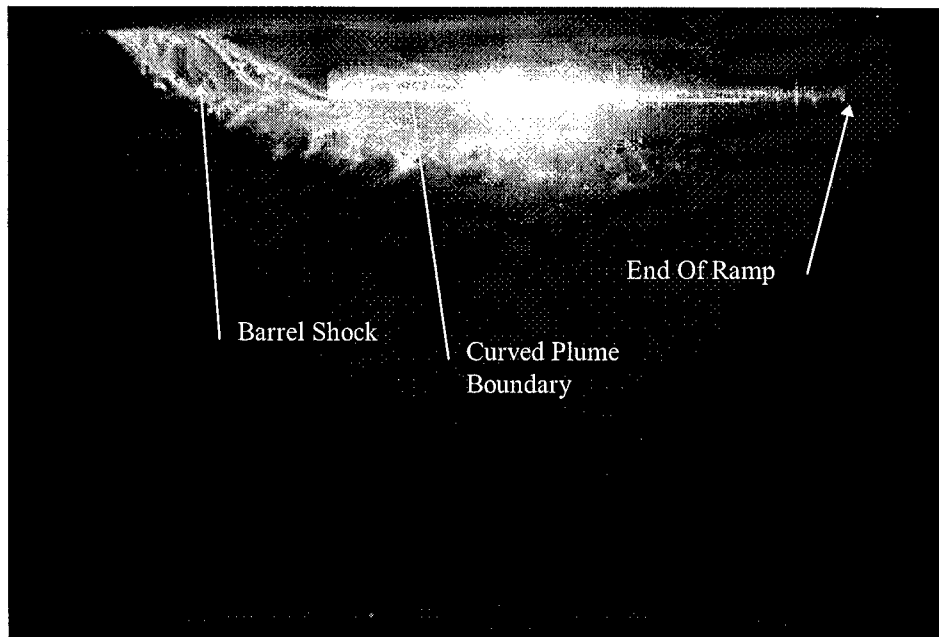


Figure 5.37: Extended Diamond Ramp ER 1, Instantaneous Parallel Oriented Laser Image

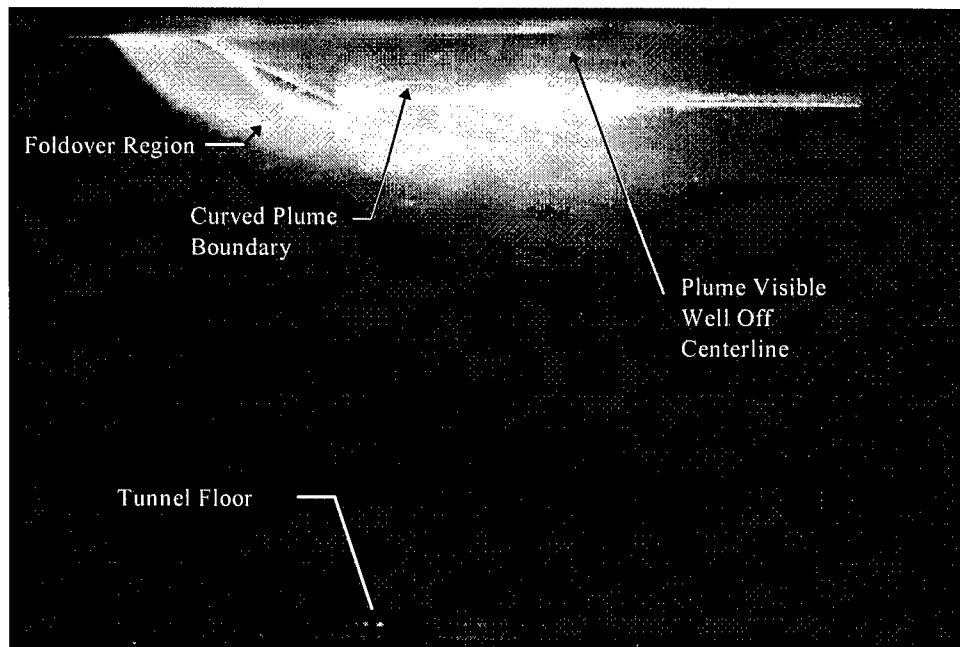


Figure 5.38: Extended Diamond Ramp ER 1, Time-Averaged Parallel Oriented Laser Image

Shown in Figures 5.37 and 5.38 are the instantaneous and time-averaged parallel oriented laser sheet images for the extended diamond ramp, ER 1. In both images, the full length of the ramp extension is illuminated. What is immediately unusual about both of these images is the amount of plume visible

below the edge of the ramp extension. For all parallel oriented images, the laser sheet was oriented along the model centerline. With such an orientation, only seed in the centerline plane should be illuminated. However, there is considerable scatter off the sharp bottom edge of the diamond ramp extension. Reflections off the sloped sides of the extension also give both images a three-dimensional aspect. This indicates the laser sheet was either slightly off center or slightly wider than the vertex edge of the ramp extension. The structure identified as the curved plume boundary is unique to ramp ER 1. The curved plume boundary is most likely the outside of the plume after the plume foldover below the Mach disk. This structure does not appear to be injectant seed surface flow on the model, as it was observed to occur during all phases of the plume seeding (i.e., the curved boundary was observable before seed surface flow could develop). The tail of the plume is seen to spread almost to the tunnel ceiling, which for this geometry means that seed particles up to  $2d$  off the tunnel ceiling centerline are illuminated. The intensity of the plume tail drops to background levels well before the illumination along the ramp bottom edge decays, indicating the majority of the seed material has been moved out of the centerline plane by vortex action.

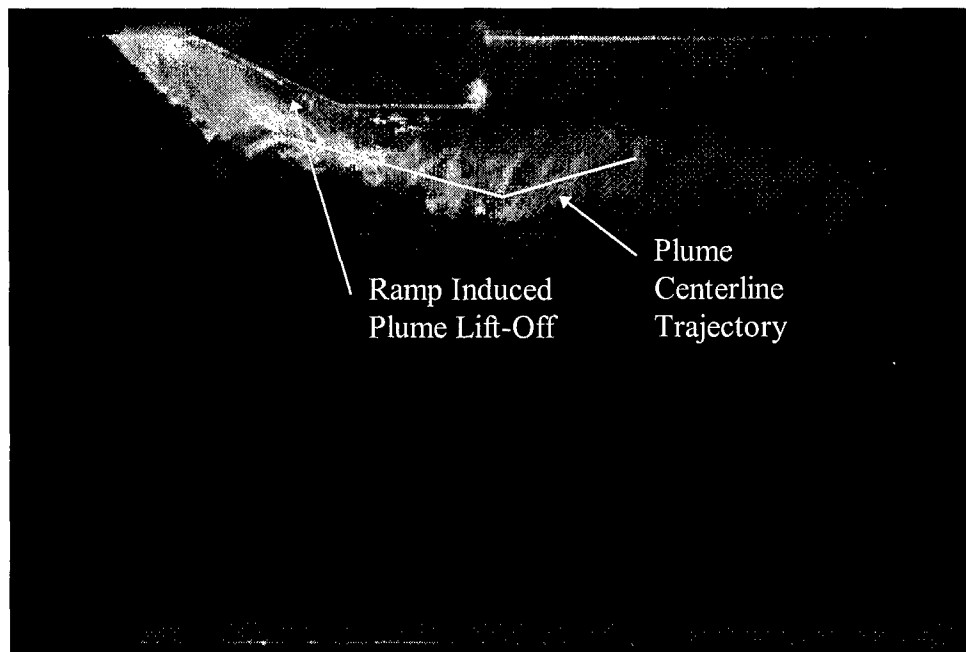


Figure 5.39: Truncated Ramp Extended ER 2, Instantaneous Parallel Oriented Laser Image

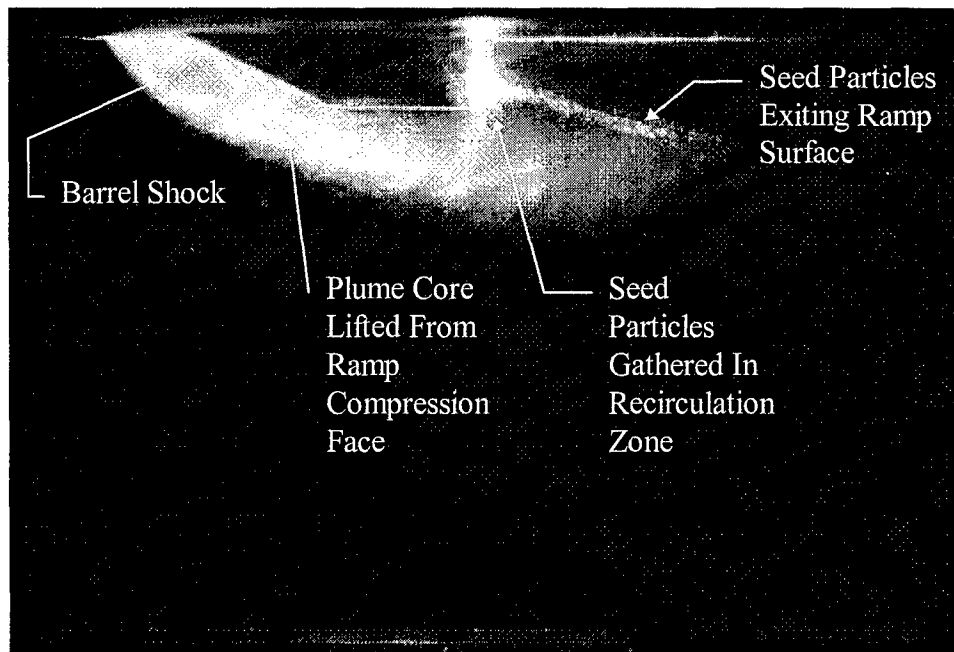


Figure 5.40: Truncated Extended Ramp ER 2, Time-Averaged Parallel Oriented Laser Image

The instantaneous and time-averaged parallel oriented images for the truncated extended ramp ER 2 are shown in Figure 5.39 and 5.40 respectively. The instantaneous image captures a substantial magnus effect lift-off away from the compression face of the ramp, which is blurred due to the exposure time and surface flows in the time-averaged image, Figure 5.40. In Figure 5.40, the effect of the lift-off is visible in the annotated core region of the plume. For either case, the magnus effect creates a local enhancement in penetration. The presence of seed particles between the plume core and the truncated ramp compression face results from surface flow on the ramp face, which accumulated during the length of the exposure. The surface flows provide a small indication of the plume vorticity where visible on the ramp vertical sides. Another exposure length related feature of the time-averaged image is the linear exiting of seed particles from the bottom rear of the ramp. The truncated rear face of this particular ramp provides a recirculation zone in which seed particles gather and shed. The seed particles are shed along a streamline that is approximately  $18^\circ$ . This streamline is located in the center of the vortex pair, which draw the ramp rear face collected seed particles out into the freestream. In the region the exiting seed particles intersect the main plume, the image intensity decreases as the bottom centerline plume injectant is distributed around the plume periphery by vortex mixing action.

In comparison to the simple transverse injection case, Figures 5.2 and 5.3, both images of the truncated extended ramp ER 2 show a significant bend of the plume centerline back towards the tunnel ceiling. In Figure 5.39, a line is fitted to the plume to indicate the bend in the plume and flow back towards the tunnel ceiling after clearing the end of the ramp. This bending indicates that the overall plume trajectory may be bending back towards the tunnel ceiling after passing through the vertically oriented expansion fan formed along the bottom rear face of the extension.

To summarize the complicated aspects of the trailing edge flow, three distinct and separate effects are visible in the time-averaged truncated extended ramp image, Figure 5.40. First, the collected seed particles on the ramp rear face are drawn into the freestream by the counter-rotating vortex pair, at an angle of  $18^\circ$ . Second, the outer bottom edge seed concentration of the plume is drawn out of the centerline plane by the vortex mixing action, resulting in a lower image intensity. Finally, the entire plume structure appears to bend back to the tunnel ceiling after passing through the expansion off the extension's bottom rear. Through the duct flow analogy presented in section 2.4, this bending should increase vorticity.

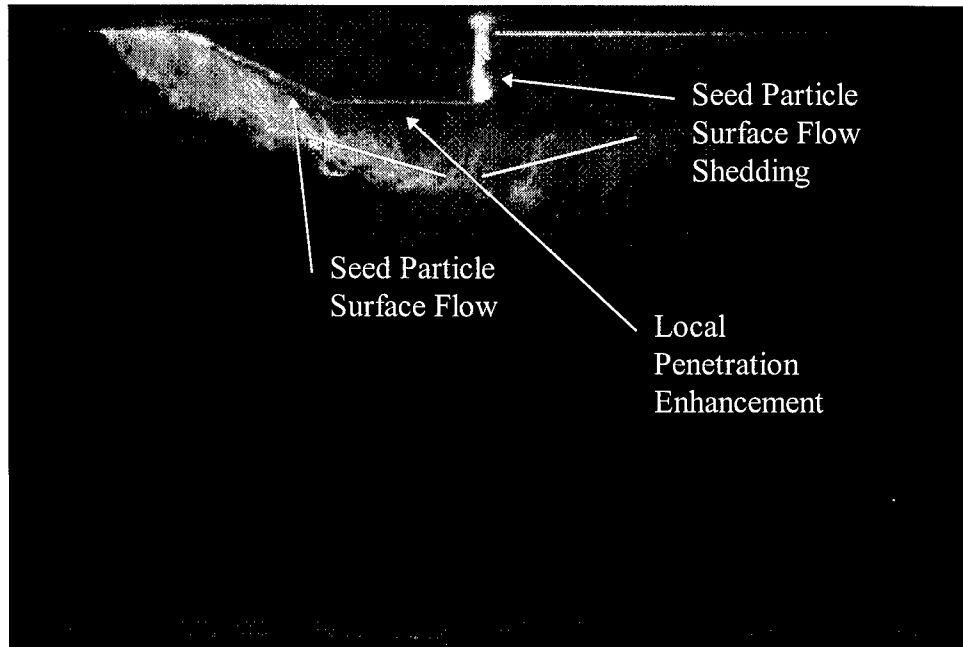


Figure 5.41: Tapered Extended Ramp ER 3, Instantaneous Parallel Oriented Laser Image

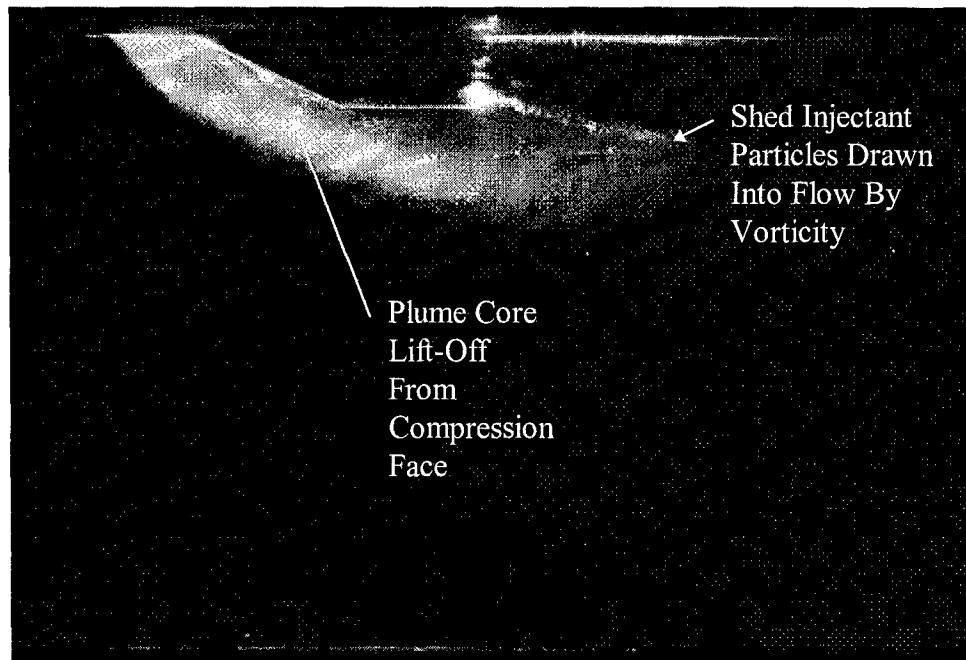


Figure 5.42: Tapered Extended Ramp ER 3, Time-Averaged Parallel Oriented Laser Image

Figures 5.41 and 5.42 show the instantaneous and time-averaged parallel oriented images for the tapered ramp. Features similar to the truncated extended ramp flow images include an early magnus effect lift-off from the ramp compression face, which results in a greater penetration than seen in the simple transverse case. Also, surface flow is visible on the compression ramp face, as well as injectant collecting along the rear edge of the ramp. The plume centerline trajectory is indicated in Figure 5.41, with a bend observable as the plume passes by the ramp rear edge. There are differences between the images that are of interest. The injectant exit angle (created by the center of the vortex pair drawing accumulated seed particles, shown in Figure 5.42) is  $11^\circ$ . The bend in the plume trajectory in this image appears less than the bend observed in the truncated extended ramp. The flow passing under the rear edge of the ramp can only expand over a thin edge instead of a broader truncated edge, which will result in a weaker expansion and less plume turning back towards the tunnel ceiling. The lesser bend incurred by the weaker expansion of the tapered extended ramp results in weaker duct flow induced vorticity, and hence a slighter injectant exit angle off of the ramp rear edge

### 5.3.1.3 Extended Ramp Cross Flow Oriented Images

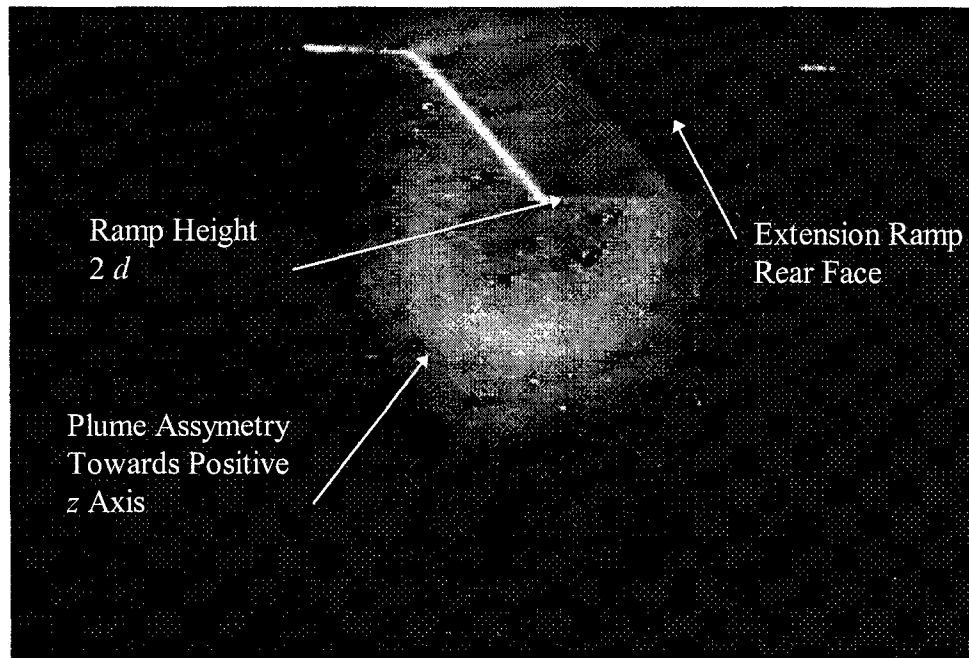


Figure 5.43: Extended Diamond Ramp ER 1, Time-Averaged Cross Flow Oriented Laser Image

Figure 5.43 depicts the time-averaged cross flow image of the diamond extended ramp. Of interest in this image is the plume asymmetry on the positive  $z$  axis side (the direction of flow is into the page and towards the left). In the parallel oriented images, Figures 5.43 and 5.44, a substantial amount of plume is visible spreading towards the tunnel ceiling. The plume asymmetry is also present in the Mach contour plot for this ramp, Figure 5.40. This asymmetry is most likely due to a minor manufacturing defect in the model forcing the unsteady vortex pair consistently to one side of the ramp. A singular feature of this image is the ramp extension passing through the plane of the laser sheet. The ramp-laser intersection furnishes a relative means to measure plume size and penetration. The ramp height is indicated to provide scale to the image.

The extension of the ramp also demonstrates why this ramp is best suited for qualitative assessment. The area of the plume in this plane is indeterminate because up to a fifth of the plume is obstructed by the ramp. It is interesting to note however that the plume vortices appear intact despite the presence of the ramp.

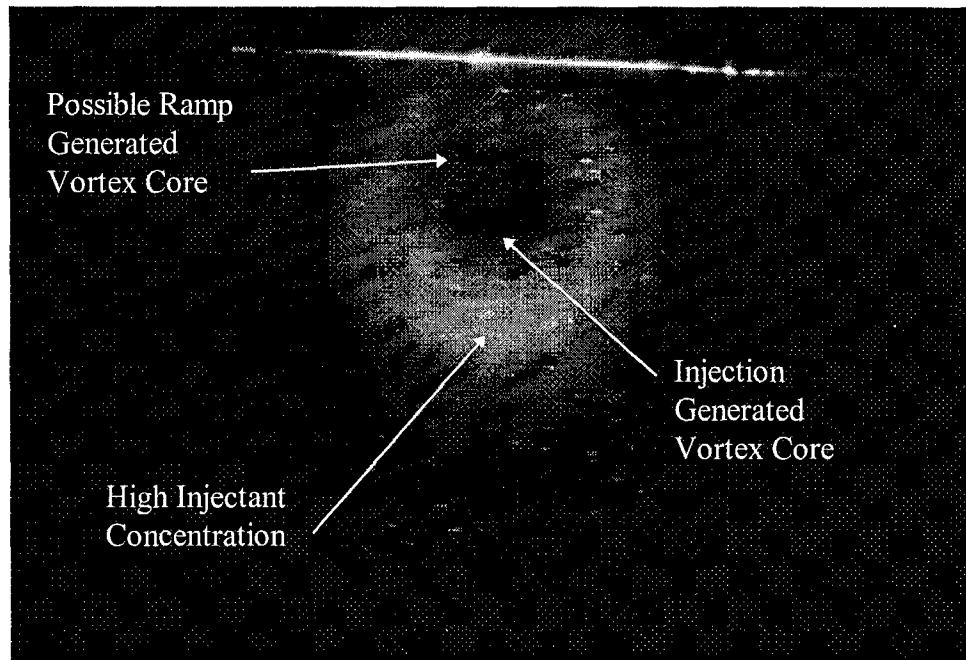


Figure 5.44: Truncated Extended Ramp ER 2, Time-Averaged Cross Flow Oriented Laser Image

Shown in Figure 5.44 is the cross flow oriented image for the truncated extended ramp, ER 2.

The plume cross section has the general crescent shape observed for the simple transverse injection case in Figure 5.5. However, two differences are observable from the simple transverse injection case. First, there is a possible second set of counter rotating vortex cores generated from the flow spillage on the ramp and extension. Instead of the uniform, evenly tapering crescent shape seen along the inside periphery of the simple transverse injection case, this plume cross section has two opposing structures that appear to be slightly drawn into the center of the plume. This would result from two vortices stacked on top of each other with the same spin direction. Directly below the arrow pointing to the possible ramp generated core is the most visible of these structures.

A second difference in the truncated extended ramp image from the simple transverse cross flow image is the relatively bright region in the plume center bottom. This bright region reflects a relatively high injectant concentration and is a result of the stream of particles exiting the ramp rear surface being convected to the bottom of the plume by the counter rotating vortices. Figure 5.40 shows the particle stream exiting the ramp rear face at approximately  $18^\circ$ , which would intersect the outer bottom of the plume by the  $x/d$  of 20 station where these images were acquired. Once the particles enter the bottom



center portion of the crescent, they would remain there until dispersed by the vortices to the plume periphery.

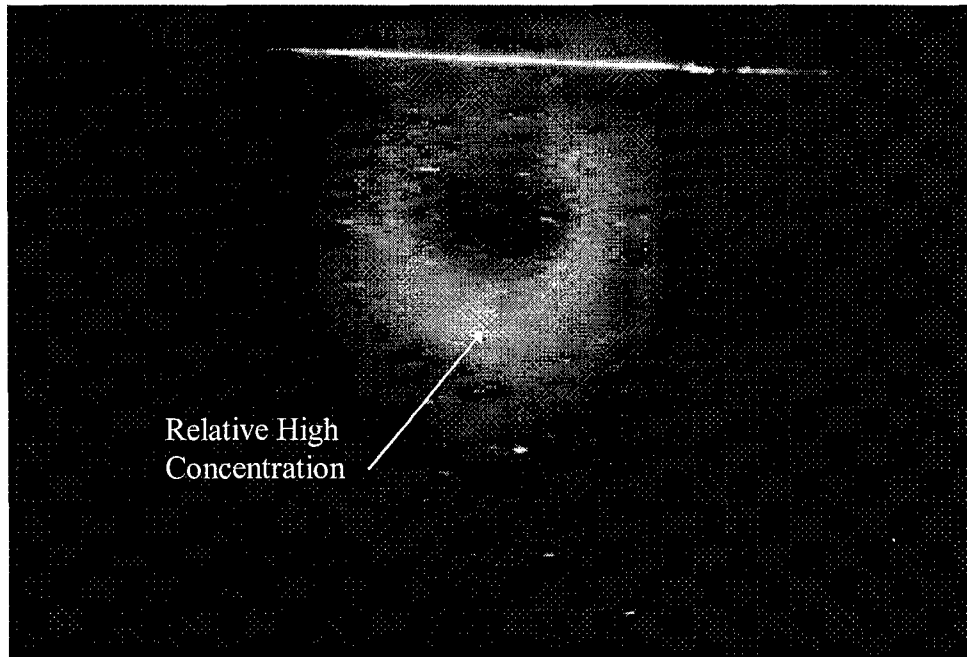


Figure 5.45: Tapered Extended Ramp ER 3, Time-Averaged Cross Flow Oriented Laser Image

Figure 5.45 shows the cross flow oriented image for the tapered extended ramp, ER 3. This image is basically identical to the simple transverse case with the exception of a slight concentration rise in the bottom center of the crescent shape. The slight increase in concentration is due to the surface flow seed particles collecting at and shedding off the tapered ramp rear edge. From Figure 5.36 the angle of the particle shedding is  $11^\circ$ , which would intersect the plume crescent boundary by the measurement plane of this image. The relative intensity of the high concentration region (in comparison to the rest of the plume intensity) is lower in the tapered ramp image than the truncated ramp image high concentration region, Figure 5.44. The reason for this is the thin trailing edge of the tapered ramp provides a much more limited area for the seed particles to collect and shed than the broader rear face of the truncated ramp.

### 5.3.2 Extended Ramp Mach Contour Plots

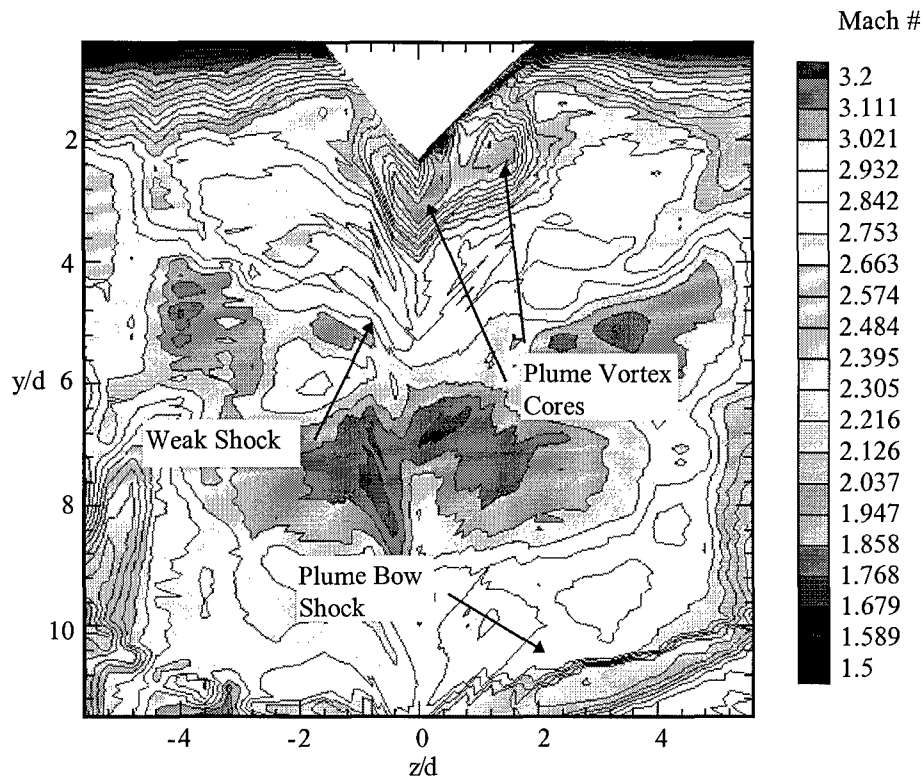


Figure 5.46: Extended Diamond Ramp ER 1 Mach Contour Plot

Figure 5.46 is the Mach contour plot generated for the diamond extended ramp, ER 1. Several interesting effects of the ramp extension are readily observable. First, the plume asymmetry noted in the cross flow image, Figure 5.43, of this ramp is confirmed. The entire plume has migrated upwards to the tunnel ceiling along the positive  $z$  axis side of the ramp. The twin vortex cores are still visible, though highly distorted as compared to the usual circular shapes seen in the other PME ramp and the simple transverse Mach contour plots. Second, a broad, flat shock is discernible, but incohesive. This is in sharp contrast to the regular and continuous (albeit relatively weak) flow recompression shock observed for simple transverse injection, Figure 5.6. This shock appears to be the weak shock identified in Figure 5.34, which would intersect the pressure probe measurement plane at the height the Mach contour shock intersects the tunnel centerline.

Another feature, or lack thereof, of interest is the ramp extension boundary layer. To capture the flow field around the extension, the pressure probes were initially placed within one half of a probe diameter from the extended ramp surface. Therefore, the probe measurements were 1/32 inches from the ramp surface, which was still not close enough to capture the developing boundary layer on the ramp extension. This provides an interesting contrast to the tunnel boundary layer, which is approximately 1/4 inches outside the region affected by the ramp.

In general, the flow field for the extended diamond ramp can best be described as disturbed. The shock and vortex structures are incoherent and distorted. The enhancement in penetration from the simple transverse injection case is solely due to the left side vortex being constrained physically by the ramp vertex. Asymmetry has been introduced to the flow field, resulting in a consistent migration of the plume. Magnus effects are not observed; to the contrary the plume-ramp extension interaction resulted in the plume moving back towards the tunnel ceiling. These effects, as well as the inability to capture the entire flow field near the ramp extension preclude the use of numerical analysis to estimate the plume size.

Shown in Figure 5.47 is the Mach contour plot of the truncated extended ramp, ER 2. This contour plot contains numerous differences from the simple transverse injection Mach contour plot, Figure 5.6. First, the bow shock appears similar, but as seen from the truncated extended ramp shadowgraph, Figure 5.35, these two shocks become collinear. This is due to the two-dimensional effect of the flat compression face increasing the compression face shock angle enough to coincide with the bow shock by  $y/d$  of 10, and is a feature common to all PME ramps with a flat compression face. The combined shock structure is not significantly stronger than the singular bow shock of the simple transverse case, therefore total pressure losses from the ramp compression face should be minimal.

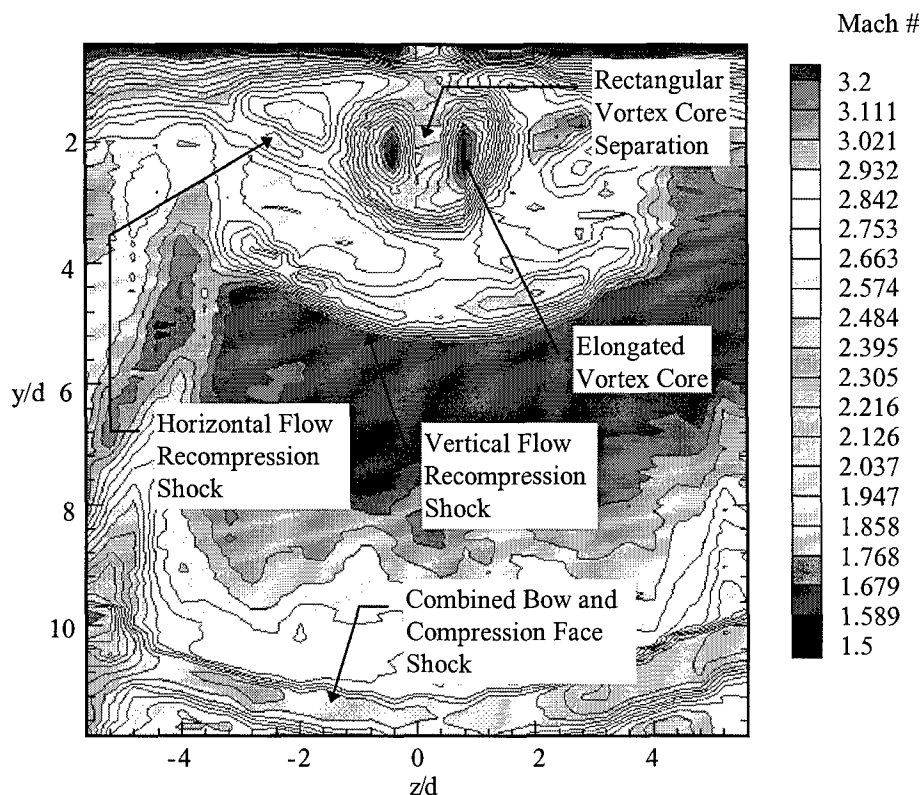


Figure 5.47: Truncated Extended Ramp ER 2 Mach Contour Plot

Second, the plume vortex cores are elongated vertically from the relatively circular vortex cores of the simple transverse case. The vortex core elongations indicate the injection generated vortices and the ramp spillage generated cores have combined into essentially one core, which meets one intended goal of this particular ramp configuration.

Third, there is a distinctly rectangular separation between the plume cores that reflects the geometry of the bottom rear edge of the truncated ramp extension. This region gives the impression that the sharp turn around the ramp bottom rear edge in effect drove the injection generated vortices to either side of the ramp and into the ramp spillage generated vortex structures. The splitting effect of the truncated ramp extension was not anticipated as part of the ramp geometric concept.

Fourth, there are two layers of shocks around the plume, one below and one passing through the plume center. The shock labeled as the vertical recompression shock is a feature common to the PME ramp contour plots and the simple transverse injection. This shock is created by the airstream turning

around the ramp in the vertical plane of the flow and impinging on the tunnel ceiling behind the ramp. The truncated extended ramp vertical recompression shock seen in Figure 5.47 is unique from the shocks created by the PME ramps in the other two groups because it does not wrap completely around the model to terminate on the tunnel ceiling. Instead, it reflects the geometry only of the front and top surfaces of the truncated extended ramp model.

The second shock layer not previously observed is the horizontal flow recompression shock. The origin of the horizontal recompression shock is the flow passing on either side of the ramp recombining supersonically beyond the truncated ramp expansion region. This shock runs nearly parallel to the plume, which would impart little baroclinic torque to enhance vorticity. The horizontal recompression shock also indicates asymmetry in the flow, as it is not as fully developed on the positive  $z$  axis side. In summary, three features distinguish the truncated extended ramp Mach contours from the other PME ramp Mach contours: vortex elongation, vortex separation, and a horizontal shock intersecting the plume.

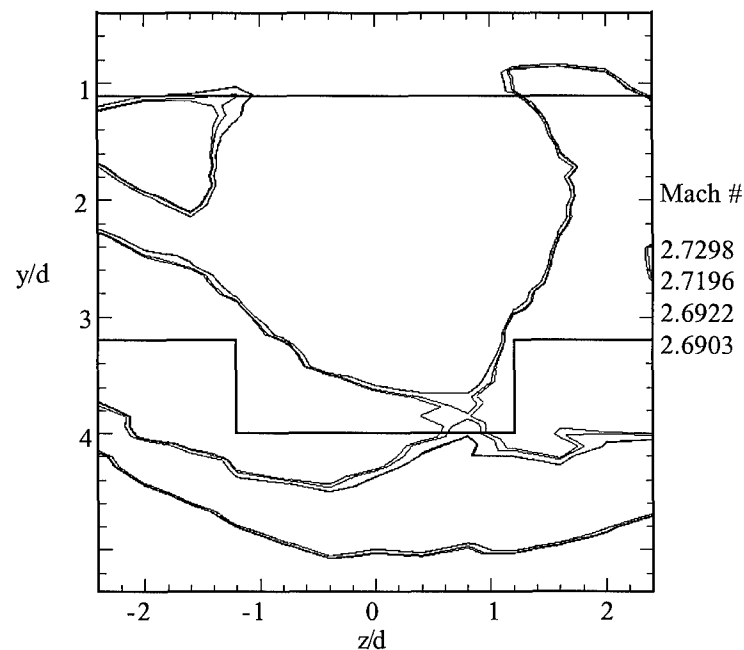


Figure 5.48: Truncated Extended Ramp ER 2 Area Contour Plot

Figure 5.48 shows the Mach contours produced through the four plume area determination methods. The upper and lower boundaries indicate the modified region used to exclude boundary layer or

shock structures from the plume area. For this particular case, the plume area includes a section of the horizontal recompression shock, which artificially inflates the area computation. Again, the Mach contours collapse into a single line for the majority of the search region, with relatively minor discrepancies in the bottom outer edge and boundary layer. Table 5.6 summarizes the area and centroid location results for the truncated extended ramp.

TABLE 5.6  
TRUNCATED EXTENDED RAMP AREA AND CENTROID RESULTS

Area Method	95% Freestream Mach	Area (cm <sup>2</sup> )	Centroid ( $y/d$ )
Graphical	2.73	1.17	2.24
Box	2.72	1.15	2.24
Modified Box, $y/d=1.2$	2.69	1.07	2.22
Modified Box, $y/d=1.6$	2.69	1.07	2.22
Average	2.71	1.11	2.23

The four methods agree approximately as well in computing the plume area and centroid as with the simple transverse case. For the truncated extended ramp, the areas vary by 9%, a 1.5% increase in the value spread from the simple transverse computations. The modified box method results are lower than the other two methods because this method does not have a Mach number rejection criteria. In computing the local freestream Mach number, the modified box methods include the relatively low Mach number of the vertical compression shock. The graphical method and box method reject the vertical compression shock, based upon the Mach gradient criteria. The centroid results show a 1% range, similar to the 1.2% variation for simple transverse injection. Comparing the capture areas used by each method, the graphical method and box method count a portion of the horizontal recompression shock as plume area, which also raises the centroid value. The modified box method in both cases returns identical results, and does not include any of the horizontal recompression shock. Therefore, for the truncated extended ramp the results from the modified box methods give the most accurate assessment of the plume geometry. The  $y/d$  value of the average centroid for the truncated extended ramp is 7.6% further into the freestream than the average simple transverse injection centroid.

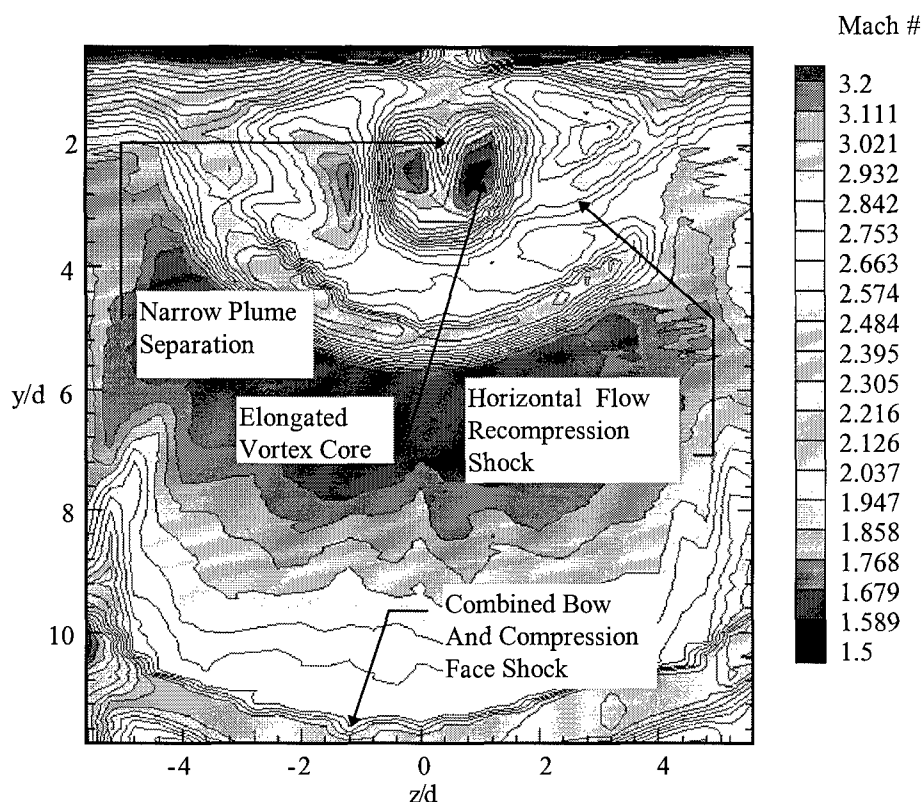


Figure 5.49: Tapered Extended Ramp ER 3 Mach Contour Plot

Figure 5.49 depicts the Mach contour plot for the tapered extended ramp, ER 3. The majority of the flow structures are identical to those seen in the truncated extended ramp Mach contour plot, Figure 5.47; differences will be highlighted. The first difference between the truncated and tapered extended ramp Mach contour plots is in the plume vortex core separation. The tapered extended ramp vortex cores are separated by a series of narrow, sharply peaked contours, which reflect the sharp trailing edge of the tapered ramp. This is in contrast to the wider, more rectangular vortex core separation in the truncated ramp Mach contour plot, reflecting the truncated rear face of the ramp. The greater compactness of the plume vortex cores is a product of the tapered edge on the ramp spillage generated vortices. As the flow travels to the end of the tapered extension, the narrow trailing edge effectively drives the two spillage generated vortices into each other resulting in a narrow separation. Again, the effect the trailing edge width would have on the plume vortex core separation was not anticipated.

The vertical recompression shock for the tapered ramp is substantially more rounded than the similar truncated ramp shock. The tapered ramp shock also connects with the tunnel ceiling boundary layer on the negative  $z$  axis side. Conversely, the truncated vertical recompression shock does not connect to the tunnel ceiling boundary layer at all. This follows from the geometry the flow must vertically maneuver around at the ramp trailing face or edge.

Figure 5.50 shows the Mach contour area plot for the tapered extended ramp and the plume area search region boundaries. The selection of boundaries for this PME ramp effectively isolate the plume core structures from other flow structures such as the tunnel ceiling boundary layer or vertical recompression shock. Table 5.7 includes the results of the four methods for determining area and centroid location.

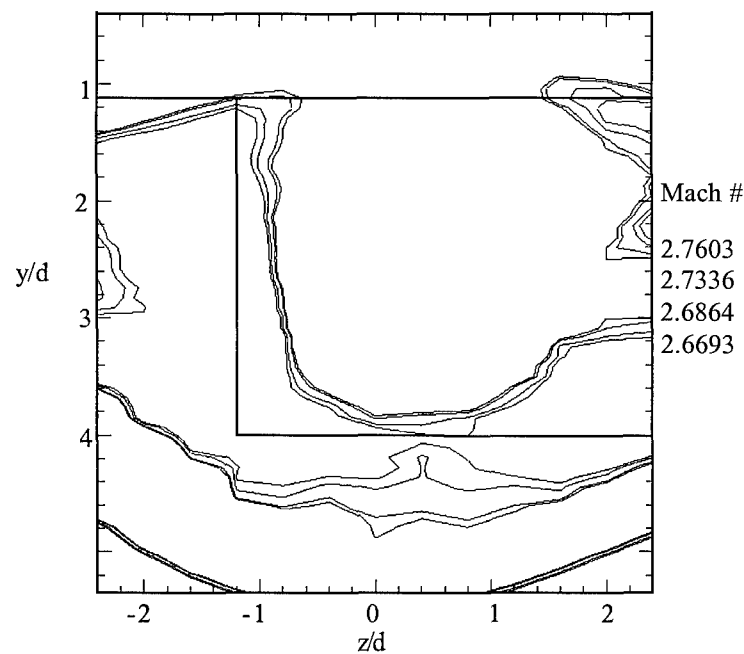


Figure 5.50: Tapered Extended Ramp ER 3 Area Contour Plot



TABLE 5.7  
TAPERED EXTENDED RAMP AREA AND CENTROID RESULTS

Area Method	95% Freestream Mach	Area (cm <sup>2</sup> )	Centroid (y/d)
Graphical	2.76	1.32	2.37
Box	2.73	1.25	2.35
Modified Box, y/d=1.2	2.68	1.17	2.35
Modified Box, y/d=1.6	2.67	1.10	2.35
Average	2.71	1.21	2.35

Agreement between the four methods of determining area is not as close as for simple transverse injection. For the tapered extended ramp, the areas have a 17% difference between top and bottom values. Several factors contribute to this spread. First, in the Mach contour plot, Figure 5.49, the tunnel ceiling boundary layer on the negative z axis side is thicker than the boundary layers on either side of the simple transverse injection Mach contour. The lower Mach number flow associated with the boundary layer would be included in the average freestream Mach number computation of both modified box methods, which do not reject any data points. Additionally, the relatively lower Mach number flow in the vertical recompression shock would also be used in the average. The graphical method and box method would reject the low Mach number regions based upon the Mach gradient criteria. The agreement in the centroid locations is excellent, since reducing the local freestream Mach number from highest to lowest strips away essentially concentric layers from the plume area plot. The centroid computed for the extended tapered ramp was 12% further into the freestream than the simple transverse case

As suggested, the expansion off of the truncated rear face of PME ramp ER 2 has a mildly detrimental effect on penetration and plume area when compared to PME ramp ER 3. Though in both cases the ramp extension appears to increase vorticity through ramp spillage, the rear face expansion of the truncated ramp noticeably decreases penetration immediately downstream of the ramp. The angle of the expansion off the ramp rear face is 90° which, barring separation effects, created an expansion fan and pulled the plume back towards the tunnel ceiling. The expansion is focused in a region of the plume

where some bending back towards the tunnel ceiling would naturally occur for simple transverse injection. The combined expansion-natural bending effect propels the plume back up towards the tunnel ceiling.

### 5.3.3 Extended Ramp Total Pressure Loss

Table 5.9 describes the total pressure losses for the extended ramp group based upon the average total pressure loss ratio. The extended diamond ramp provides an interesting result, having the second lowest total pressure loss of all the PME ramp models. This is a result of there being no downstream recompression shocks by the  $x/d$  of 20 measurement location since the ramp extension passes through the measurement plane. It is reasonable to assume that the total pressure losses incurred by the extended diamond ramp would increase noticeably if the measurement plane was behind the rear face of the ramp.

Also of interest is the effect of the truncated vs. tapered trailing edge for ramps ER 2 and ER 3. The slight frontal aspect increase of the less tapered truncated ramp is more than off set by the effect of the tapered trailing edge in total pressure loss effect. This result indicates that even a slight truncation is preferable to a sharp, flow recompression shock enhancing trailing edge when total pressure loss is to be minimized. An additional factor in the higher total pressure loss of the tapered ramp is the slightly more coherent ramp compression face shock, which appears more coherent than the truncated ramp compression face shock.

TABLE 5.8  
EXTENDED RAMP GROUP TOTAL PRESSURE LOSS

PME Ramp	Average Total Pressure Ratio	$\Pi$
Extended Diamond Ramp, ER 1	1.33	0.93
Truncated Extended Ramp, ER 2	1.35	0.92
Tapered Extended Ramp, ER 3	1.44	0.86

### 5.3.4 Extended Ramp Digital Image Quantitative Analysis

Figures 5.51 to 5.54 are plots of the plume centerline trajectories and centerline intensity decay for extended ramps ER 2 and ER 3. These plots are oriented as horizontal mirror images of the original plume images, where  $y/d$  of zero is the tunnel ceiling.

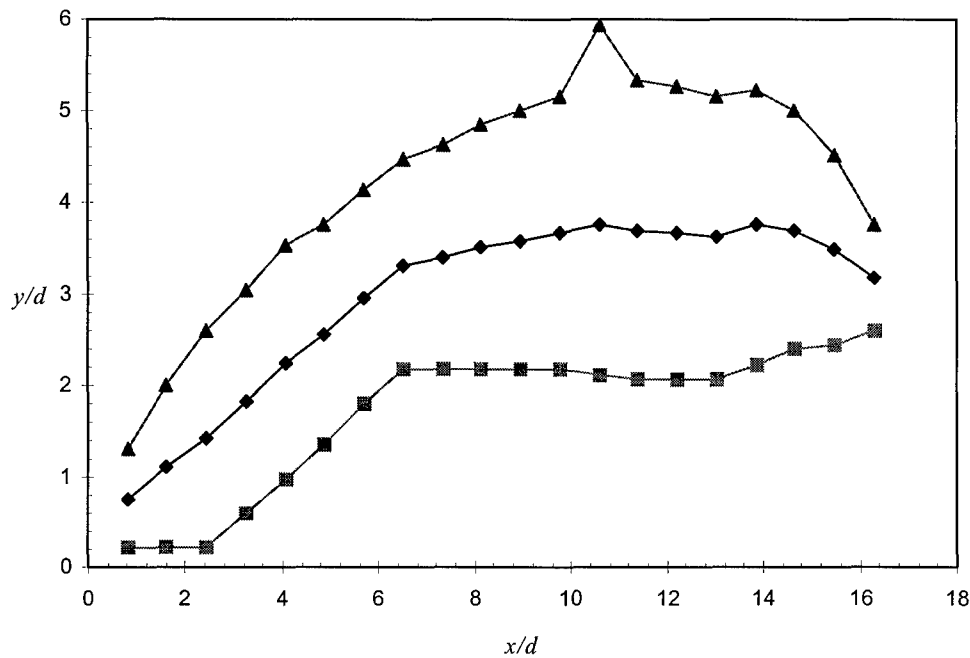


Figure 5.51: Truncated Extended Ramp ER 2 Plume Centerline Trajectory

Figure 5.51 is the centerline trajectory plot of the truncated extended ramp, ER 2. The middle line is the average centerline of the plume from Figure 5.40. The inner trace outlines the ramp to  $x/d$  of 10, then tapers up slightly as the plume is dispersed. Initially the plume centerline shows no lift-off from the ramp compression face. This is because the first three points on the inner trace map the injection port outlet, which artificially lowers the plume centerline trajectory. Additionally, surface flows on the compression face and ramp extension keep the inner trace on these surfaces, instead of capturing the magnus effect lift-off observed in the truncated ramp instantaneous parallel oriented image, Figure 5.39. From  $x/d$  of six to 11, the plume centerline is seen to separate and lift away from the ramp extension. The slope of the first eight centerline points is 0.45, nearly double the 0.23 slope for simple transverse injection, which indicates a substantial magnus effect lift-off was achieved. The maximum centerline penetration in this region is to  $y/d$  of 3.76 at  $x/d$  of 10.60. The spike in the outer trace at  $x/d$  of 10.60 is due to a single seed particle, and does not significantly alter the average of points at the  $x/d$  of 10.60 measurement location. This location is after the trailing edge for the ramp extension, therefore the centerline trajectory is no longer affected by surface flow on the ramp top. The lift-off was anticipated from the magnus effect acting on the extension.

The centerline and plume outer trace indicate a sharp turn back towards the tunnel ceiling at  $x/d$  of 14, which is a result of the plume being turned by the expansion off the truncated ramp rear face. The slope of the best fit line through the last four points in the plume centerline trace is -0.24. These observations match the centroid results for the truncated extended ramp, which indicated the truncated ramp achieves less penetration than the simple transverse case.

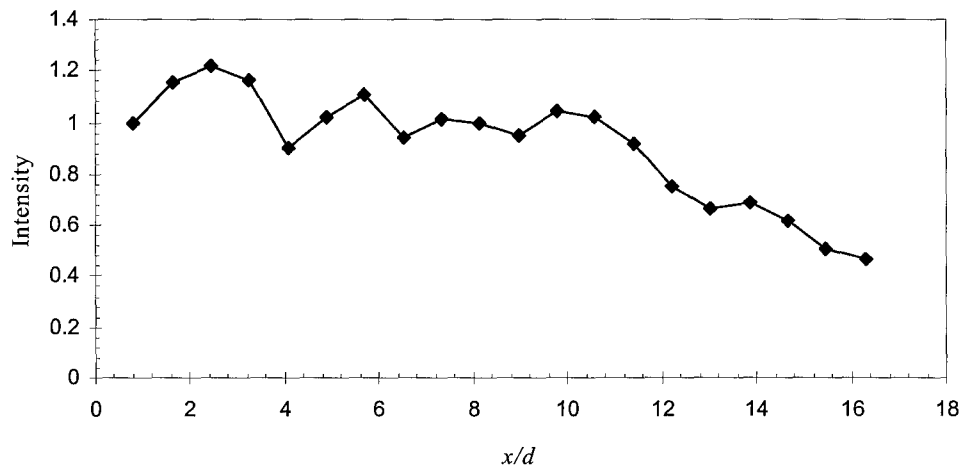


Figure 5.52: Truncated Extended Ramp ER 2 Plume Centerline Average Intensity Decay

Figure 5.52 is the truncated extended ramp ER 2 centerline intensity decay plot. The general trend in the image shows a rapid decay in image intensity after  $x/d$  of 10. This decay rate is nearly triple the overall plot decay rate observed from Figure 5.9 for simple transverse injection, -0.037. The overall decay rate of the entire truncated extended ramp plot is -0.039, which is essentially identical to the overall decay rate of the simple transverse case. The slope of a best fit line passing through the data points greater than  $x/d$  9 is -0.093. The high decay rate over the last 11 data points indicates the truncation of the ramp extension has a considerable impact on the rate at which the plume core is removed from the centerline plane to the plume periphery. The shift in the trace at  $x/d$  of 13 corresponds to the location where the more intense stream of seed particles shed from the ramp rear face intersect with the main plume, and raises the overall intensity. Scatter seen in the  $x/d$  zero to seven range is a result of the bright surface flow regions raising the average intensity in the measurement plane.

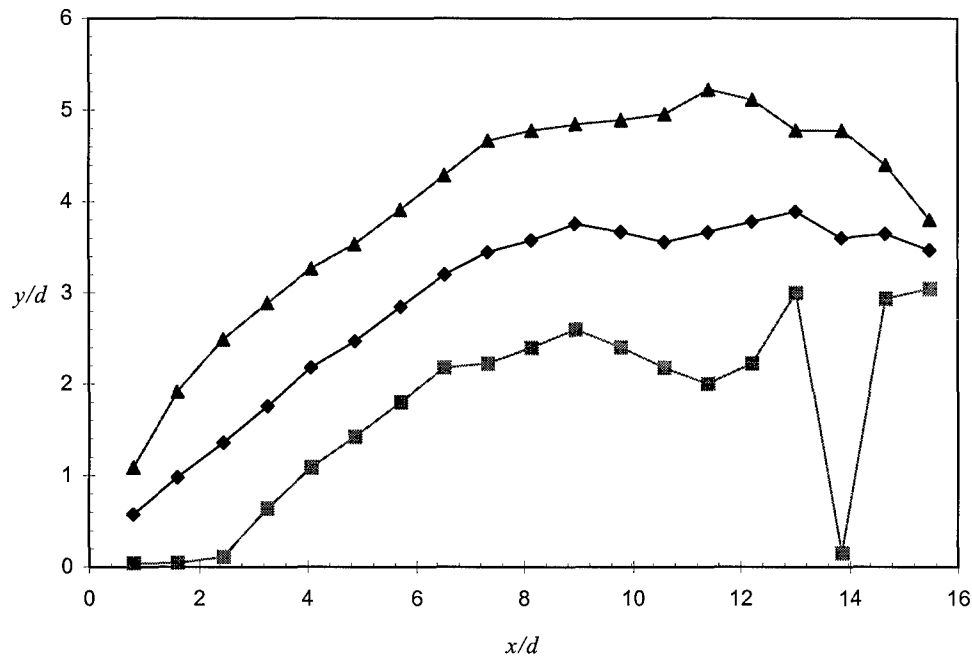


Figure 5.53: Tapered Extended Ramp ER 3 Plume Centerline Trajectory

Figure 5.53 is the plot of the plume centerline and boundaries for the tapered extended ramp, ER 3. The trends observed in this plot match those of Figure 5.51, with a few notable exceptions. The plume inner trace shows a slight lift-off from the magnus effect at  $x/d$  of three and four. The initial trajectory of the first eight centerline points is 0.46, which is double the first eight point slope of 0.23 for simple transverse injection. The inner trace also captures the effect of the stream of seed particles from the ramp extension trailing edge. A single particle trapped in the tunnel ceiling boundary layer at  $x/d$  of 14 resulted in the spike at that location. The single particle is reflected in the plume inner boundary, but does not significantly alter the average of the other 35 points at  $x/d$  of 13.85 used to determine the average plume centerline trajectory.

The plume centerline or middle trace rises nearly linearly to  $x/d$  of 8.9 and  $y/d$  of 3.75, which is the maximum penetration achieved in the truncated ramp plot, Figure 5.51. The remaining points along

the plume centerline follow a relatively flat profile, with a slight downward slope in the last four points. This pattern was observed in Figure 5.41 as a slight downturn in the plume. The best fit slope of the last four points is -0.14. This trend of a slight down turn in the plume centerline (which again reflects the middle of the crescent downstream of  $x/d$  of 10) does not appear to significantly reduce the tapered ramp plume penetration, as the average centroid location for the tapered extended ramp exceeds the simple transverse average centroid values by about 12%.

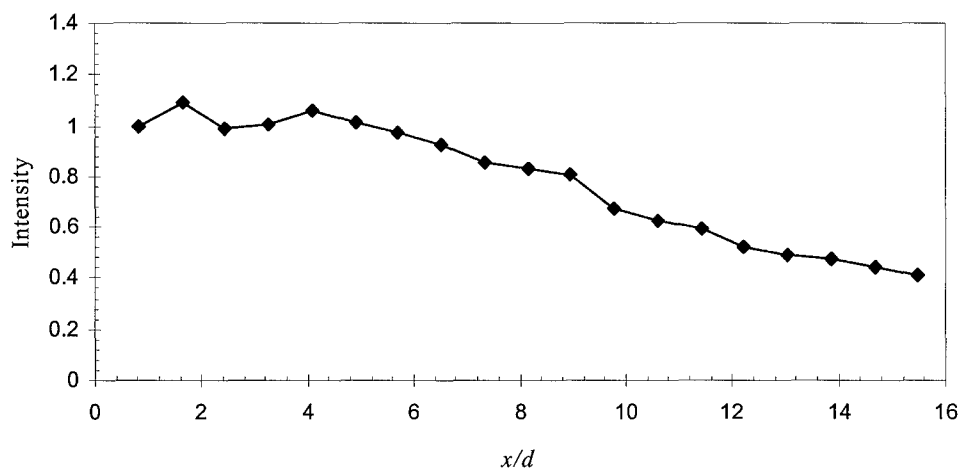


Figure 5.54: Tapered Extended Ramp ER 3 Plume Centerline Average Intensity Decay

Figure 5.54 shows the extended tapered ramp ER 3 decay of centerline intensity. The profile of the intensity decay rate is nearly identical to the plot observed in Figure 5.9 for the simple transverse case. However, the slope of the best fit line is -0.05, which is a 34% increase over the simple transverse injection decay rate. The greater intensity decay rate indicates the rate at which the ramp enhanced vortex pair strips away the plume centerline injectant seed to the plume periphery. The addition of the relatively weaker particle stream from the ramp rear edge (in comparison to the stronger stream observed in Figure 5.40) does not significantly alter the average plume intensity.

## 5.4 Injector Ramp Group #3: Asymmetric Ramps

This PME ramp group is intended to combine the two primary vorticity generation mechanism studied to date. The first is the vorticity inherent in transverse injection. The second is the vortex generation created by ramp spillover. These ramps are identical with the exception of the taper ratio. The wide ramp AR 1 tapers from  $4d$  to  $2d$  at the top of the compression surface. The narrow ramp AR 2 tapers from  $4d$  to  $1d$  at the top of the compression surface. Increasing the ramp sweep angle has been demonstrated to increase vorticity generation (described in detail in section 2.3). Both ramps in this group have a noticeable effect on the flow structures.

### 5.4.1 Asymmetric Ramp Flow Visualization

The flow visualization results are presented in the format of previous sections. For each PME ramp, the images are organized by type, starting with shadowgraph photography. The salient features of the shadowgraphs are highlighted and annotated. Analysis of the parallel oriented and cross flow oriented laser planar images follows.

#### 5.4.1.1 Asymmetric Ramp Shadowgraph Photography

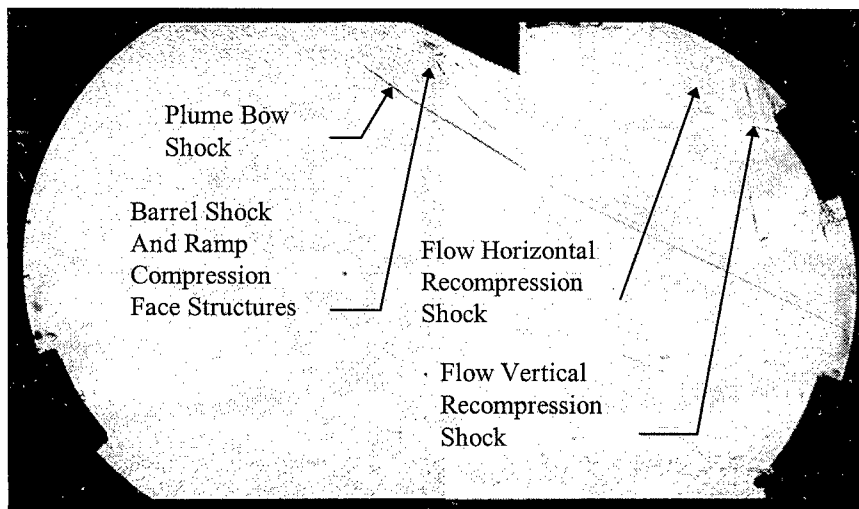


Figure 5.55: Wide Ramp AR 1 Composite Shadowgraph

Figure 5.55 is the wide ramp AR 1 shadowgraph image. The flow structures before the ramp trailing face are similar to the structures observed in previous shadowgraphs. The plume bow shock follows the established  $33^{\circ}$ - $25^{\circ}$  angle patterns. The ramp compression face presents a two-dimensional aspect to the flow, resulting in a greater compression shock angle than the bow shock. The compression

face shock passes directly through the barrel shock, which should enhance the developing vorticity with baroclinic torque. The bow shock and compression face shock appear to combine by the vertical middle of the image. Features unique to swept ramp geometries are the horizontal and vertical recompression shocks. Similar to the truncated extended ramp ER 2 and tapered extended ramp ER 3, the flow off the rear face experiences two compressions. The vertical shock is created by the flow passing under the ramp turning towards the tunnel ceiling. This ramp has a relatively wide top rear surface, which should result in a strong vertical shock structure. The horizontal shock results from the side flows recombining at the taper angle of the ramp. Since this ramp is relatively wide at the rear surface, the strength of the recombination shock should be attendant weak. The vertical recompression shock exits the image further into the freestream than previously observed in the PME ramp shadowgraphs. This is because the wide ramp is half the total length of the other PME models, which moves the origin of the shock forward approximately three cm. The movement forward impacts the second baroclinic torque effect, since the shock intersects the plume at a further upstream point. This translates into a region of the plume where vorticity should be stronger than the further downstream location because viscous effects will not have worked as long to dissipate the plume.

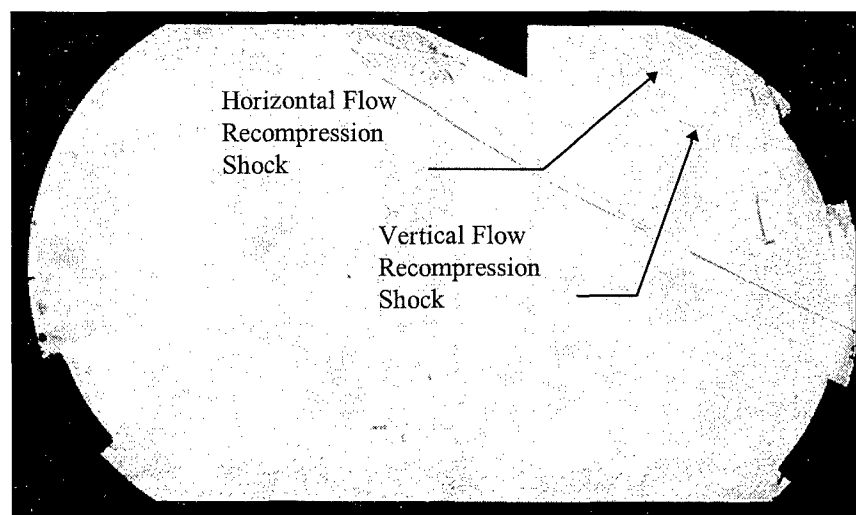


Figure 5.56: Narrow Ramp AR 2 Composite Shadowgraph

Figure 5.56 is the narrow ramp AR 2 shadowgraph. The majority of features, including the plume bow shock angles, barrel shock and compression face structures are identical to those observed for



the wide ramp, Figure 5.55. Also similar to the wide ramp, the relative shortness of the narrow ramp will move the vertical flow recompression shock forward relative to the other groups of PME ramps, with a resulting change in the baroclinic torque. However, ramp AR 2 is narrower than ramp AR 1 in respect to the top rear faces. The narrow trailing edge should effectively reverse the magnitudes of the vertical and horizontal shocks. With less surface for the flow to turn vertically back towards the tunnel ceiling, the vertical shock for the narrow ramp should be lessened compared to the wide ramp. Conversely, with a greater sweep angle, the side flow components should be greater than the narrow ramp, resulting in a stronger collision and horizontal shock.

#### ***5.4.1.2 Asymmetric Ramp Parallel Oriented Images***

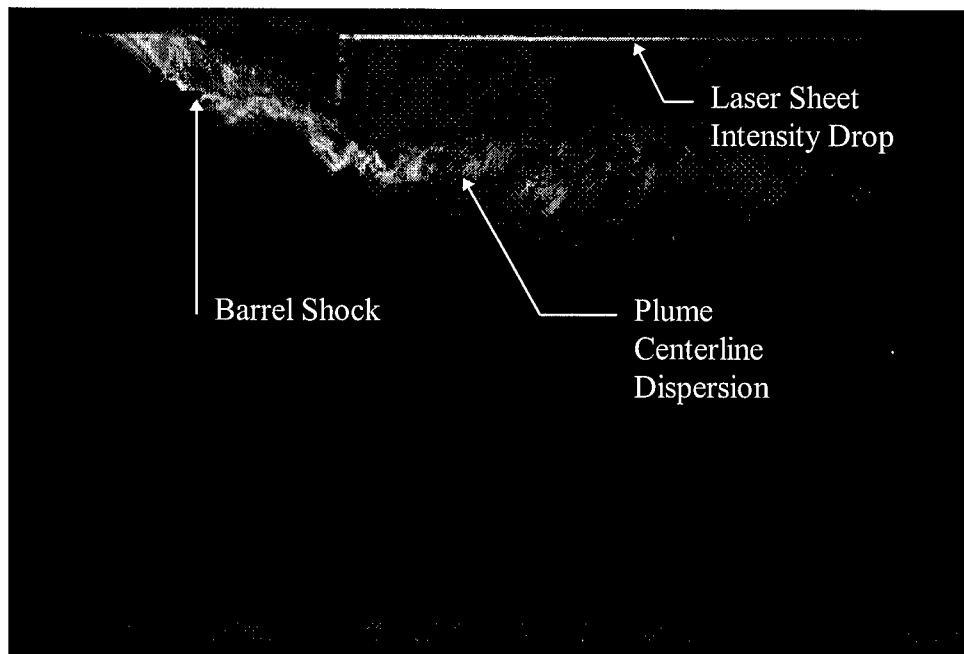


Figure 5.57: Wide Ramp AR 1, Instantaneous Parallel Oriented Laser Image

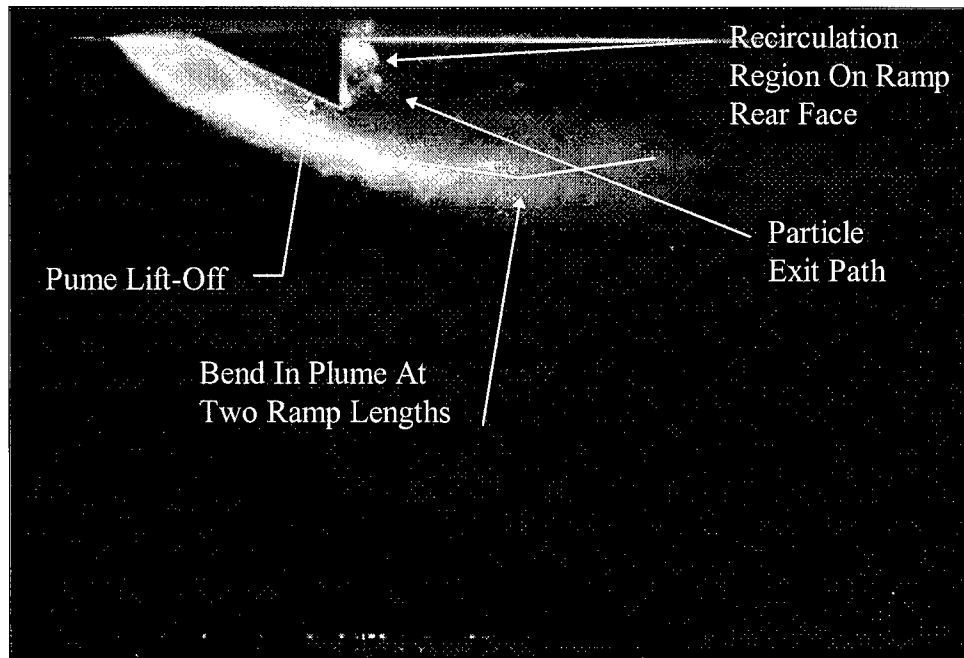


Figure 5.58: Wide Ramp AR 1, Time-Averaged Parallel Oriented Laser Image

Figures 5.57 and 5.58 show the instantaneous and time-averaged parallel oriented laser images for the wide ramp, AR 1. For Figure 5.57, the injection was seeded relatively lightly compared to the other PME instantaneous parallel oriented images. Heavier seeding or time-averaging tends to push the plume dispersion point farther downstream, where it is almost coincidental with the laser sheet intensity decline. The light seeding clearly highlights the rapid decrease in plume intensity well before an intensity decrease is observed for the laser sheet from its reflection off the tunnel ceiling. Lighter seeding also helps define the plume barrel shock edges, since fewer particles are present to obscure the barrel shock center.

Figure 5.58, the time-averaged parallel oriented image for the wide ramp, has several features not captured in the instantaneous image. First, the plume shows an immediate magnus effect lift-off from the ramp compression face, which is traceable almost to the front edge of the compression face. Second, some surface flow is visible on the ramp compression face. Third, the surface flow is seen to accumulate in a recirculation region that is almost  $1/2 d$  at the widest, and cover the entire vertical height of the ramp rear face. The recirculation region was anticipated for this design, and could prove useful as a flameholder in a supersonic combustor. Unlike the similar extended ramp images, Figures 5.40 and 5.42, there is no

clear, coherent stream of particles exiting the rear face recirculation zone. There is an indication of a particle exit path, but this may also be a temporary structure due to the ramp base effects.

The bend observed in the plume centerplane path for the wide ramp occurs at approximately two ramp lengths from the injector exit. This is the area that the centerplane plume bend occurs for all previous ramps (excluding the extended diamond ramp, ER 1). Unlike the truncated extended ramp, ER 2, the expansion over the rear edge of the wide ramp does not increase the bend in the plume. The explanation for these effects is geometric scaling. The truncated extended ramp induces a strong expansion in a region where the plume would naturally turn slightly back towards the tunnel ceiling (as evinced by the weak flow recompression shock observed for simple transverse injection in section 5.1), in effect enhancing the natural turn. The wide ramp, AR 1, ends just after the plume foldover region. At the end of the wide ramp, the plume vortices are still aligning with the main flow direction. The strong expansion off the wide ramp rear face also coincides with the generation or enhancement of plume vorticity from ramp spillage. Therefore, the expansion interacts with the plume while a substantial amount of the injected momentum is directed out into the freestream and the developing vorticity is being enhanced. The combination of these effects result in a steeper centerline penetration trajectory than observed for the simple transverse injection case.

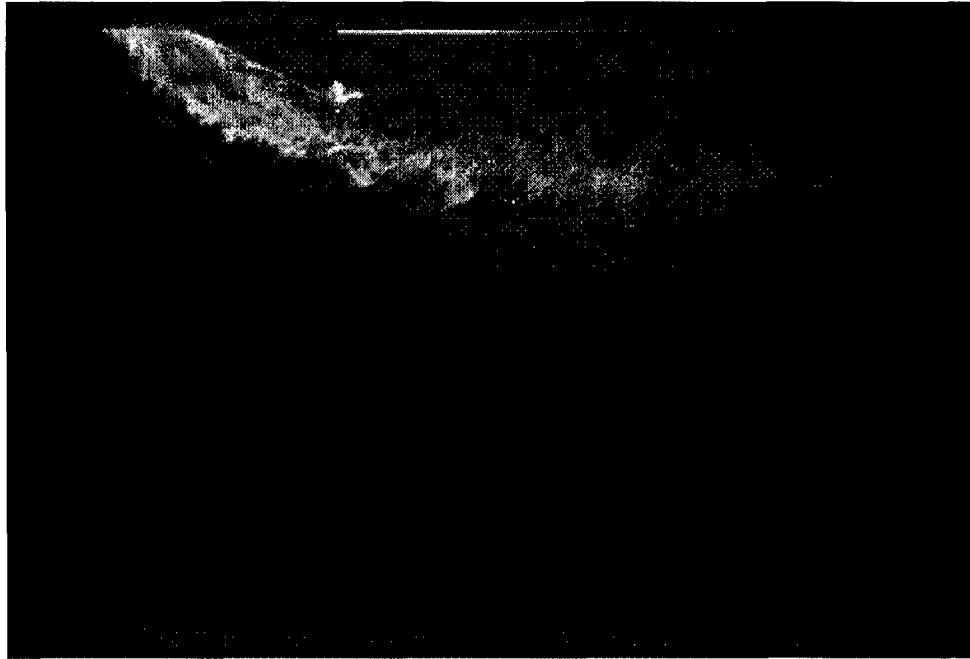


Figure 5.59: Narrow Ramp AR 2, Instantaneous Parallel Oriented Laser Image

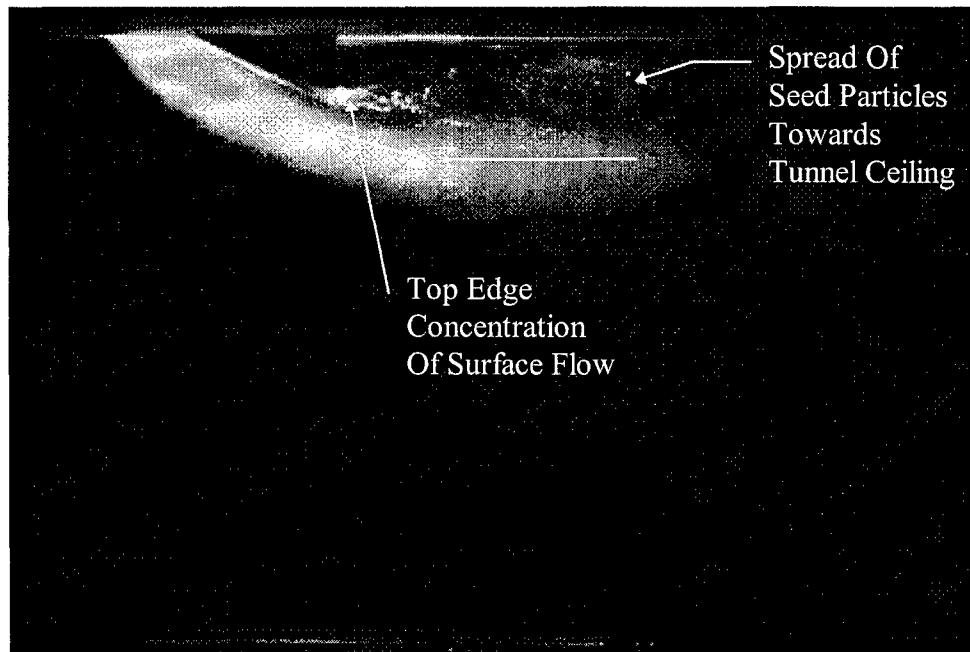


Figure 5.60: Narrow Ramp AR 2, Time-Averaged Parallel Oriented Laser Image

Figure 5.59 and 5.60 show the instantaneous and time-averaged laser sheet images for the narrow ramp, AR 2. The majority of the observed flow is similar to the wide ramp, AR 1, which is to be expected from their similar geometries. In both Figure 5.59 and 5.60, however, several differences from the wide ramp are visible. First, the recirculation region on the narrower rear face of the narrow ramp is concentrated to the bottom of the ramp rear face. Second, the concentrated seed particles can be seen

coherently exiting the ramp rear face almost parallel to the tunnel ceiling. The coherent ramp rear face exit stream begins to disintegrate by one half a ramp length from the ramp rear face, and rapidly disperses in the region between the tunnel ceiling and the visible plume core. Third, the surface flow from the ramp compression face that feeds the seed particle accumulation on the rear face is visible on the side of the ramp bottom. For the straight sided PME ramps, the surface flows are normally observed as thin, high intensity lines on the ramp compression surface which clearly delineate the solid ramp boundary. For the narrow ramp, the flow has swept some of the surface flow material into the vortex spillage off the ramp compression face. Clear observation of this wrapping effect is somewhat fortuitous; the effect was noted where visible for the other straight sided PME ramps, but the vortex wrapping was not as distinctly defined as the narrow ramp. This is due to the extra width of the other straight sided PME ramps diffusing the laser sheet intensity out of the centerline plane.

Similar to the simple transverse injection case, the narrow ramp plume centerline trajectory undergoes a slight bend approximately two ramp lengths downstream from the injection. The final visible trajectory of the plume centerline is essentially horizontal, which also matches the trajectories seen for the simple transverse case. The overall degree of the downstream bending is less than the bending at the same location for the wide ramp. This reflects the weaker effect of the narrow ramp rear edge expansion than the expansion over the wide ramp rear edge.

#### ***5.4.1.3 Asymmetric Ramp Cross Flow Oriented Images***

Figure 5.61 is the time-averaged cross flow oriented laser image for the wide ramp, AR 1. The vortex core in this image is relatively clear in comparison the cross flow image of the simple transverse case, Figure 5.5. The seed particles observed in the core region are large and distinct from the core background. Around the inside periphery of the crescent shaped seed structure, a further collection of relatively large seed particles is visible. The large seed particles are the result of shedding surface flow from the wide ramp rear face. This indicates a different mechanism for surface flow shedding than the method explained in section 5.3.1.2 for the extended ramps ER 2 and ER 3. In this case, instead of the

shed seed particles traveling linearly in between the plume vortex cores, the shed seed appears to be immediately entrained along the inner region of the vortex cores. Since the inside of the vortex cores rotate slower than the outer vortex periphery, mixing will occur at a slower rate, allowing the large seed particles to remain intact.

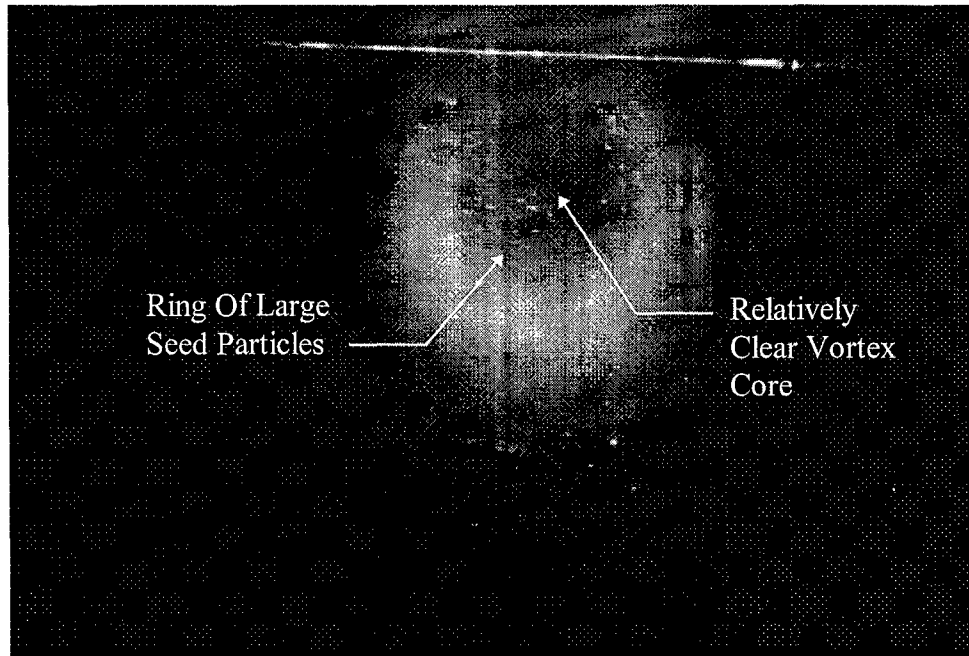


Figure 5.61: Wide Ramp AR 1, Time-Averaged Cross Flow Oriented Laser Image

The seeded plume crescent differs from the simple transverse injection by remaining at the same relative intensity from the bottom to the tops of the crescent. This indicates the ramp spillover enhanced vortices have distributed the seed more evenly throughout the entire crescent, instead of a high concentration remaining in the bottom of the crescent. Overall, the crescent structure is coherent, with little spreading to the bottom, sides, or interior. This indicates the wide ramp can provide even mixing concentration, which would allow for more even combustion of fuel than simple transverse injection if used in a combustor.

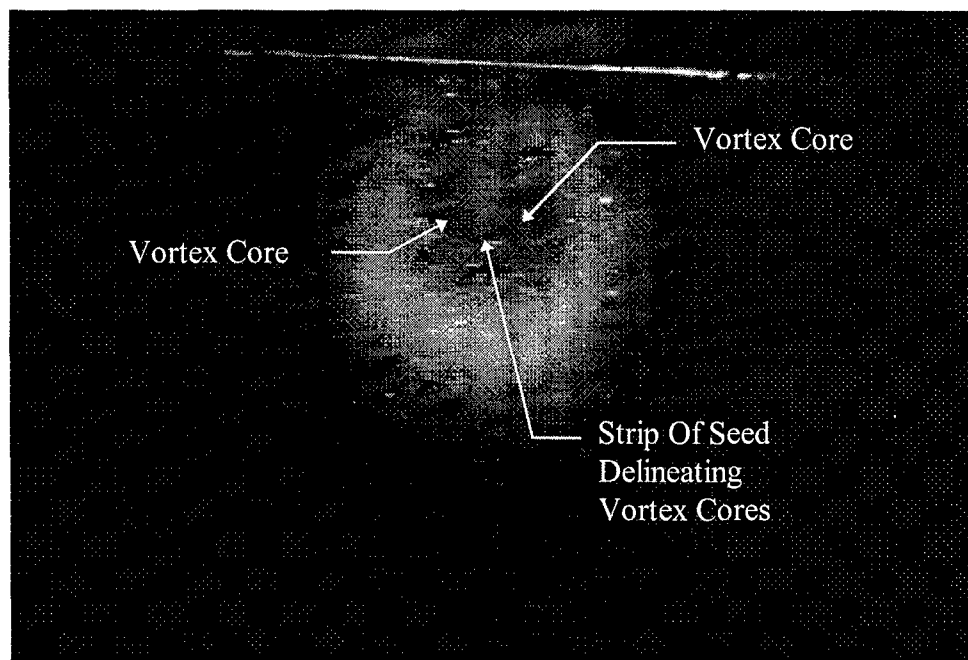


Figure 5.62: Narrow Ramp AR 2, Time-Averaged Cross Flow Oriented Laser Image

Figure 5.62 is the time-averaged cross flow oriented laser image for the narrow ramp, AR 2. The narrow ramp cross flow image has a steady intensity throughout the crescent, which depicts a more even seed spreading through the crescent than the simple transverse injection case. The more even spreading of the narrow ramp crescent intensity is a consequence of the enhanced vorticity generated by ramp spillover effects. In the center of the vortex core region, a vertically oriented strip of low intensity seed particles is visible. The seed strip provides a demarcation between the two counter rotating vortex cores. This feature is not visible in the simple transverse injection, which has a more even spread of seed particles across the plume core region. The centers of the vortex core are distinguishable for the narrow ramp image as two darker circular regions on either side of the demarcation strip.

### 5.4.2 Asymmetric Ramp Mach Contour Plots

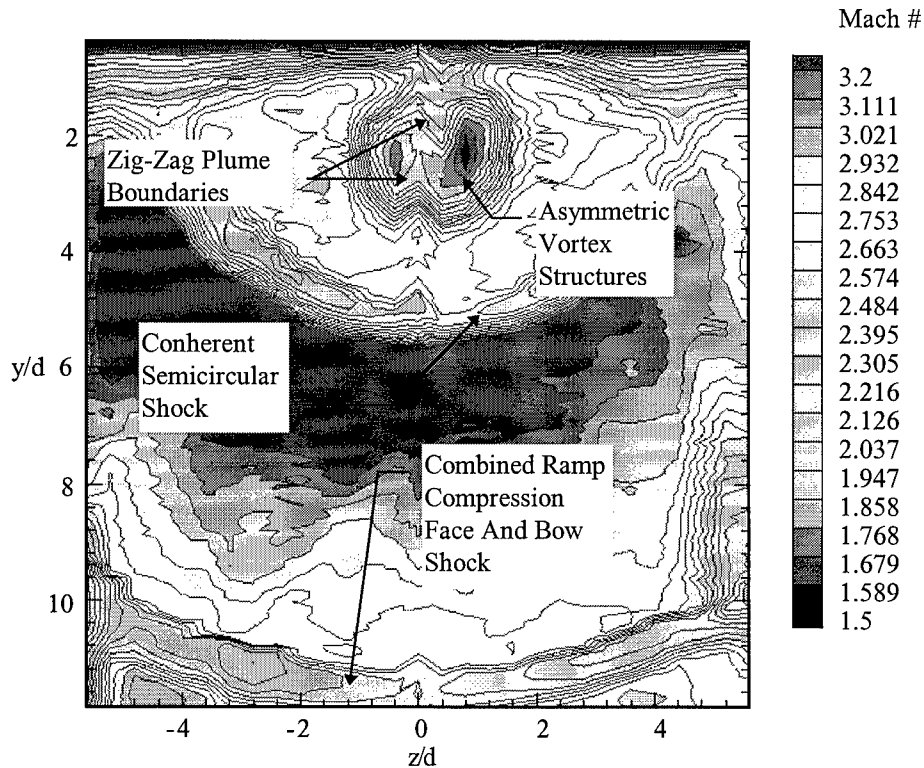


Figure 5.63: Wide Ramp AR 1 Mach Contour Plot

Figure 5.63 depicts the Mach contour plot for the wide ramp, AR 1. The effect of the wide ramp on the flow field and plume is evident when compared to the simple transverse injection, Figure 5.6. The flow recompression shock created as the injected plume turns slightly back towards the tunnel ceiling is substantially more pronounced for the wide ramp than for simple transverse injection. This stronger shock is created from the flow passage through the ramp compression face-rear face expansion fan. The expansion accelerates the flow and intensifies the resulting shock as the flow turns away from the tunnel ceiling. At  $y/d$  of 5.6, the peak height into the freestream of the wide ramp flow recompression shock is slightly less than the simple transverse injection, which peaks at  $y/d$  of six.

The wide ramp plume bow shock does not appear to be substantially stronger than the simple transverse shock, though the wide ramp bow shock is coincidental with the ramp compression face shock. An objective of masking the ramp partially with the plume bow shock appears to be achieved. The wide



ramp Mach contour does not reflect any additional shock structures beyond the three observed, though an additional weak shock was observed in the wide ramp shadowgraph, Figure 5.46. This was interpreted as a shock produced as the two ramp side flows rejoin and turn with the tunnel flow, similar to the effects observed in section 5.3 for extended ramps ER 2 and ER 3. It is possible that the weak shock observed in the wide ramp shadowgraph was too weak to produce an effect in the Mach contours.

An interesting feature of the wide ramp Mach contour plot is the unusual asymmetry in the plume shape. In the simple transverse and PME ramp Mach contour plots where the twin vortex cores are distinct (i. e., for ramps ER 2, ER 3, AR 1 and AR 2), a trend for a larger core in the positive  $z/d$  side vortex is present. The asymmetry appears to be the result of a slight injector misalignment, as noted by McCann<sup>26</sup>. However, the plume for the wide ramp appears on the whole to have rotated clockwise, relative to the Mach contour plot. The zigzag plume boundaries identified in Figure 5.63 appear to reflect the bottom edge of the wide ramp rear, rotated clockwise. A similar effect to the vortex core separation was noted for the truncated extended ramp, ER 2. There are no discernible defects in the manufacturing of the wide ramp, or any other physical cause in the shape of the wide ramp to suggest a cause for the apparent rotation.

Figure 5.64 presents the Mach contours generated by the four area determination methods. In general, the Mach contours (and hence the local freestream) are lower than the area contours for simple transverse injection, Figure 5.7. The contours essentially collapse into a single line for the majority of the plume; indicating the plume vortex structure Mach contours are tightly packed. The plume areas and centroids by method are summarized in Table 5.9.

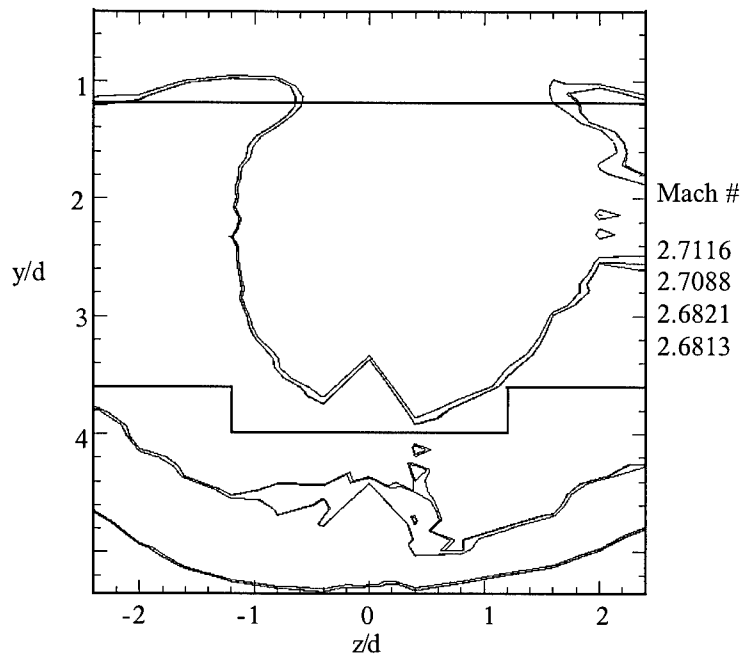


Figure 5.64: Wide Ramp AR 1 Area Contour Plot

TABLE 5.9  
WIDE RAMP AREA AND CENTROID RESULTS

Area Method	95% Freestream Mach	Area (cm <sup>2</sup> )	Centroid (y/d)
Graphical	2.71	1.09	2.33
Box	2.71	1.10	2.33
Modified Box, y/d=1.2	2.68	1.04	2.32
Modified Box, y/d=1.6	2.68	1.04	2.32
Average	2.69	1.07	2.33

The results for the wide ramp plume area vary 5% from largest to smallest. The variations in plume centroid locations are in essence insignificant. The excellent agreement for centroid location indicates the plume center was found, and that the area determination methods are in agreement as to the fundamental shape of the plume. The average area results for the wide ramp show an increase of 6% over the simple transverse injection average area result, Table 5.1. Area expansion is most likely due to the additional vorticity generated by the ramp spillover. The average centroid for the wide ramp is a 13% increase in penetration over the simple transverse injection. The increase in penetration can be tied directly to the

magnus effect lift-off from the ramp compression face, which initially propels the plume further into the freestream than the simple transverse injection.

Figure 5.65 shows the Mach contour plot for the narrow ramp, AR 2. The plume core for the narrow ramp is rotated in a similar fashion to the wide ramp, except in the opposite direction. There are no physical defects observed with the narrow ramp model to account for the rotation. As with the wide ramp, the data to create the narrow ramp plume region of the Mach contour plot was collected over a series of tests. This indicates the plume rotation phenomena for both ramps is repeatable.

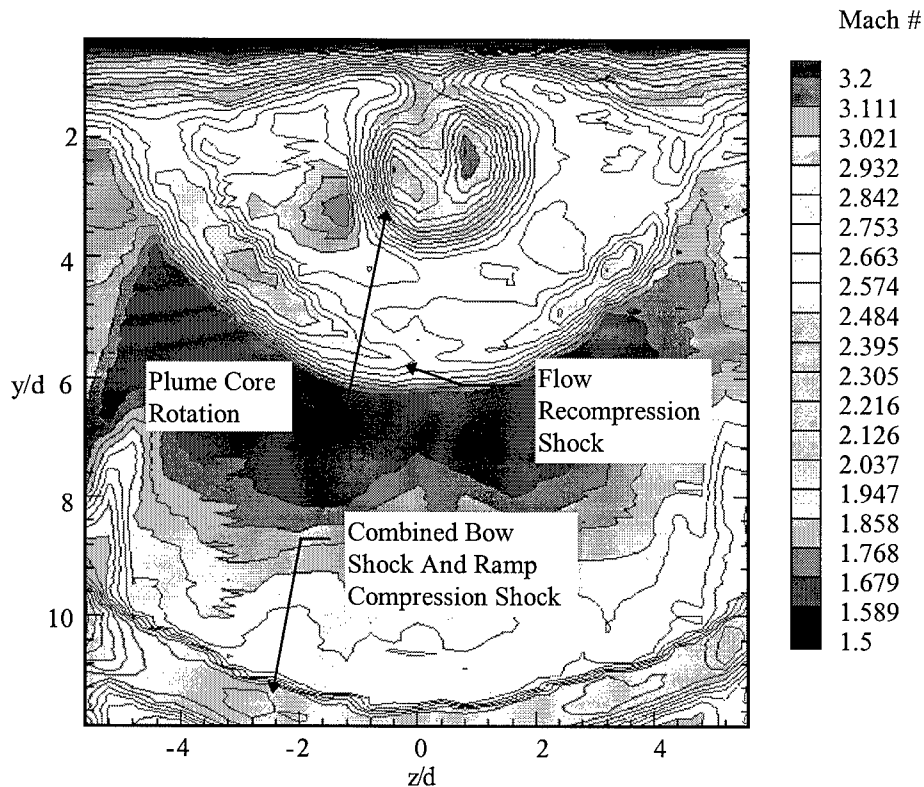


Figure 5.65: Narrow Ramp AR 2 Mach Contour Plot

The flow recompression shock for the narrow ramp is similar in strength to the simple transverse injection flow recompression shock, Figure 5.6. The narrow ramp flow recompression shock is located nearly identically into the freestream, peaking at  $y/d$  of six, as the simple transverse injection flow recompression shock. The primary difference between the narrow ramp flow recompression shock and the

simple transverse injection flow recompression shock is the coherence of the narrow ramp flow recompression shock.

The bow shock for the narrow ramp has combined with the ramp face compression shock, which appears as a single shock in the Mach contour plot. This again indicates the goal of reducing the ramp shock by placing the ramp compression face behind the plume has been achieved. Similar to the wide ramp Mach contour plot, the weak horizontal shock identified in Figure 5.47 is not manifested in the narrow ramp Mach contour plot.

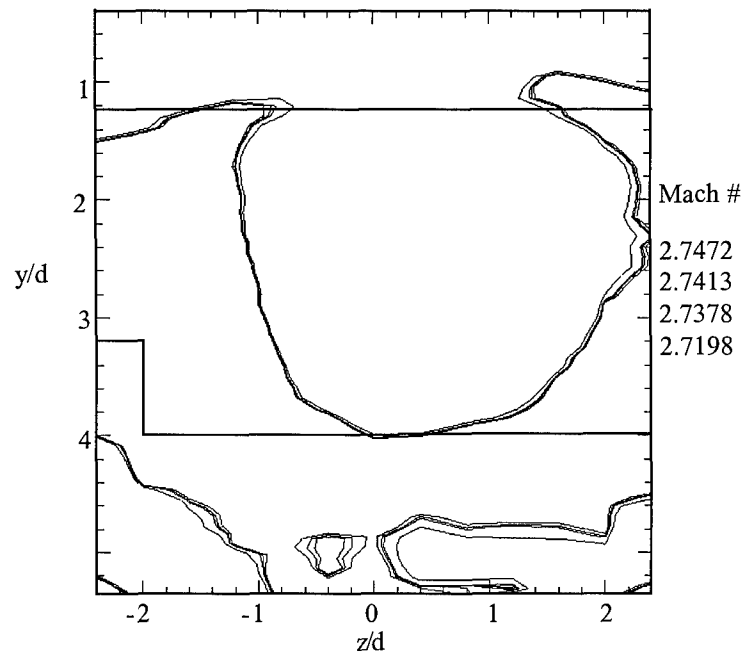


Figure 5.66: Narrow Ramp AR 2 Area Contour Plot

Figure 5.66 shows the area Mach contour plot generated for the narrow ramp, AR 2 from the four area determination methods. As can be seen in Figure 5.66, three of the four methods are in practically exact agreement. The dissenting Mach contour is from the modified box method using  $y/d$  of 1.2 as the bottom of the local freestream search region. This  $y/d$  is well into the tunnel ceiling boundary layer, which results in an overall lower local freestream Mach number and plume area. Table 5.10 summarizes the results of the area and centroid computed for each method.

TABLE 5.10  
NARROW RAMP AREA AND CENTROID RESULTS

Area Method	95% Freestream Mach	Area (cm <sup>2</sup> )	Centroid (y/d)
Graphical	2.74	1.21	2.43
Box	2.75	1.21	2.43
Modified Box, y/d=1.2	2.72	1.16	2.45
Modified Box, y/d=1.6	2.74	1.21	2.43
Average	2.73	1.20	2.44

The presence of the ramp on the plume is readily apparent in comparison to the area and centroid for the simple transverse injection. The average local freestream Mach number for the narrow ramp is not significantly faster than the simple transverse injection local freestream Mach number. The average area for the narrow ramp plume however is 19% larger than the simple transverse injection average area. The average centroid for the narrow ramp plume is also 19% larger than the simple transverse injection average centroid.

#### 5.4.3 Asymmetric Ramp Total Pressure Loss

Table 5.9 describes the total pressure losses for the asymmetric ramp group based upon the average total pressure loss ratio.

TABLE 5.11  
ASYMMETRIC RAMP GROUP TOTAL PRESSURE LOSS

PME Ramp	Average Total	$\Pi$
	Pressure Ratio	
Wide Ramp, AR 1	1.40	0.88
Narrow Ramp, AR 2	1.40	0.88

As seen in Table 5.11, the total pressure losses incurred by placing either of the two asymmetric ramps into the post plume flow field is 12%. The first difference between the two ramps for the value of average total pressure ratio is to three decimal points, which is not considered significant.

#### 5.4.4 Asymmetric Ramp Digital Image Quantitative Analysis

Figures 5.67 to 5.70 are plots of the plume centerline trajectories and centerline intensity decay for extended ramps AR 1 and AR 2. These plots are oriented as horizontal mirror images of the original plume images, where  $y/d$  of zero is the tunnel ceiling.

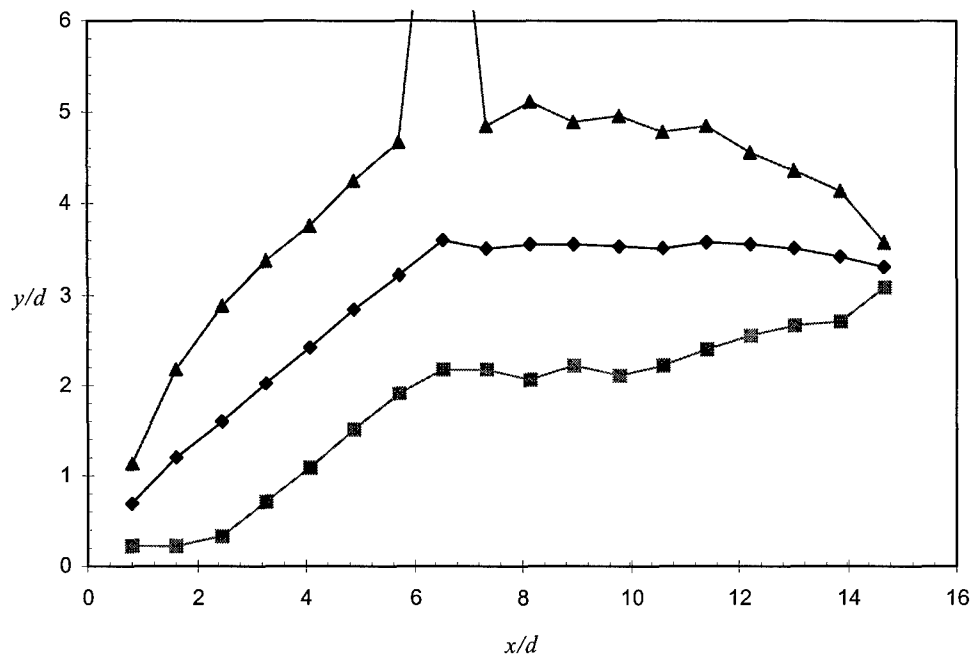


Figure 5.67: Wide Ramp AR 1 Plume Centerline Trajectory

Figure 5.67 is the plot of plume centerline trajectory for the wide ramp, AR 1. The wide ramp plume centerline trajectory depicted by the center trace shows a steep linear rise along the compression face of the ramp. The slope of the first eight centerline points is 0.51, which is over double the slope of 0.23 for first eight points of the simple transverse injection centerline, Figure 5.8. The centerline trajectory for the wide ramp peaks at  $x/d$  of 6.5 and  $y/d$  of 3.60, compared to a maximum height of 3.32 for simple transverse injection, a 9% increase. After the peak, and through the region of the post ramp expansion fan, the plume centerline is relatively flat, following a similar profile to the simple transverse injection plume centerline trajectory. The primary enhancement in penetration for the wide ramp is

clearly achieved from a magnus effect lift-off of the plume from the ramp compression face. After the rapid rise, the wide ramp plume undergoes a decay in centerline position associated with the vortices stripping the injectant away from the plume centerline to the plume periphery. The expansion fan associated with the ramp rear face also appears to create a slight downward trend in the plume centerline trajectory.

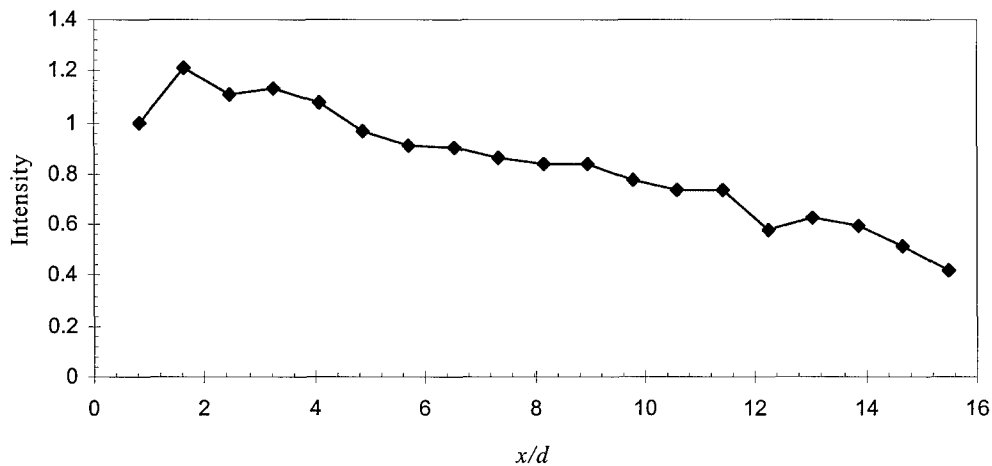


Figure 5.68: Wide Ramp AR 1 Plume Centerline Average Intensity Decay

Figure 5.68 is the plot of centerline intensity decay for the wide ramp, AR 1. The slope of the decay line is -0.047, a 26% increase in decay from simple transverse injection. The increased decay rate is a direct result of the ramp spillage enhanced vorticity spreading the concentrated plume centerline core seed to the outer plume periphery. The slight dip in the trace at  $x/d$  of 12.2 is the result of a streak in the tunnel window through which the image was acquired, and not indicative of any unusual flow behavior.

Figure 5.69 is the narrow ramp AR 2 plume centerline trajectory plot. The narrow ramp plume centerline trajectory shows a linear rise along the compression face of the ramp. The slope of the first eight centerline points is 0.40, which is almost double the slope of 0.23 for first eight points of the simple transverse injection centerline, Figure 5.8. Unlike the previously examined wide ramp, the linear rise at the 0.40 slope in the centerline plume trajectory continues to  $x/d$  of 9.8 before significantly tapering off.

The maximum centerline height achieved is  $y/d$  of 3.69 at  $x/d$  of 10.6, an 11% increase over simple transverse injection maximum centerline  $y/d$ . After the maximum height is achieved, the plume centerline has a slight decrease in the slope of the remaining points, similar to the simple transverse injection.

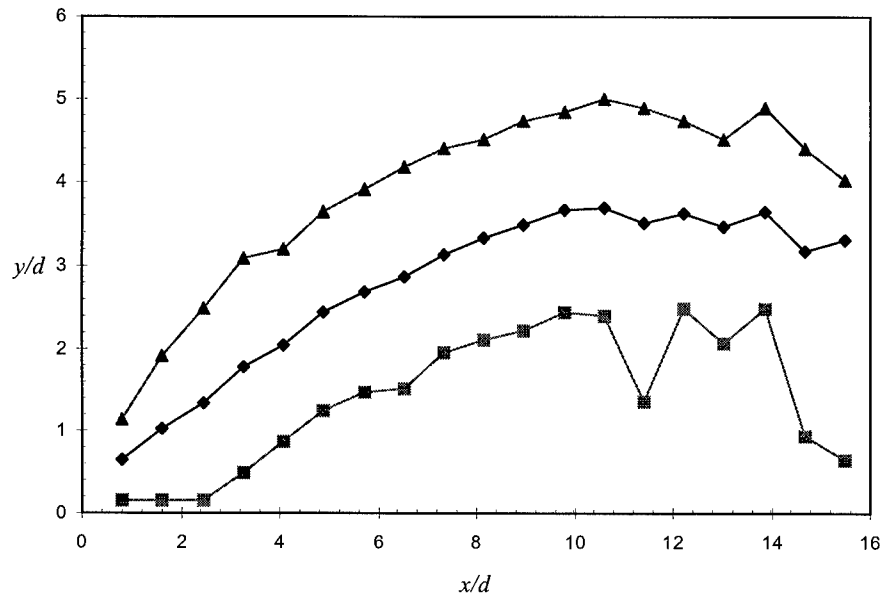


Figure 5.69: Narrow Ramp AR 2 Plume Centerline Trajectory

Figure 5.70 is the plume centerline average intensity decay plot. The overall slope of the plot is - 0.042, which is a 13% increase in decay over simple transverse injection. Similar to the wide ramp plume centerline average intensity decay plot, the higher decay rate for the narrow ramp over simple transverse injection can be attributed to the ramp induced vorticity enhancement. The narrow ramp plume centerline intensity decay plot does reflect the geometry of the ramp, i. e., there is a spike or discontinuity to indicate the ramp location or shape. The discontinuity occurs at  $x/d$  of 4.07, which is the location of the high concentration of surface flow seed particles accumulating on the ramp vertical surfaces from the vortex wrapping effect, Figure 5.51.



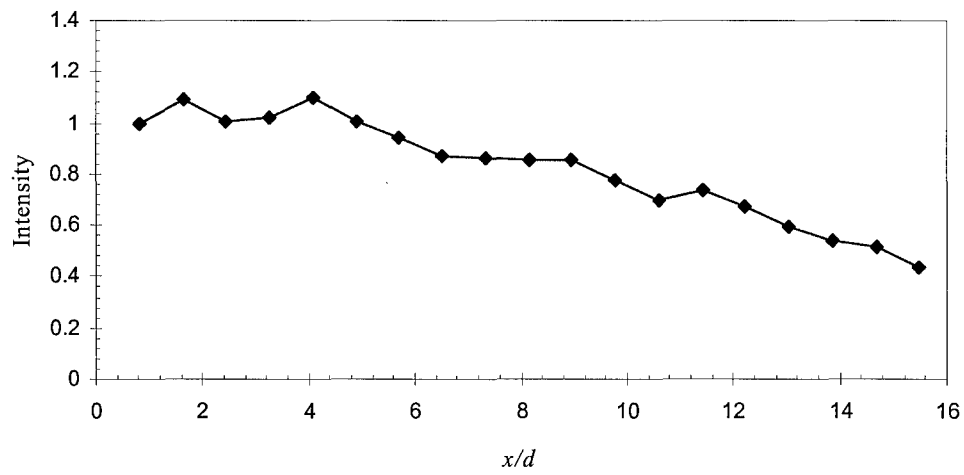


Figure 5.70: Narrow Ramp AR 2 Plume Centerline Average Intensity Decay

## **5.5 Summary of Results**

This section summarizes the results presented earlier in Chapter Five. The total pressure loss ratios for each model are presented. The mean flow data based plume areas and centroid heights of all PME ramps are plotted against total pressure loss. The digital image based plume initial trajectories and centerline decay rates for each PME ramp are also plotted against total pressure loss. Effects of comparative geometric features (such as truncated vs. tapered extensions) are provided.

### **5.5.1 Total Pressure Loss Evaluations**

Table 5.12 summarizes the total pressure loss ratios by injector configuration.

TABLE 5.12  
INJECTOR TOTAL PRESSURE LOSS RATIO,  $\Pi$

Blank	1
Double Diamond Ramp SR 1	0.95
Double Cone Ramp SR 2	0.91
Double Ramp SR 3	0.83
Truncated Extended Ramp ER 2	0.92
Tapered Extended Ramp ER 3	0.86
Asymmetric Wide Ramp AR 1	0.88
Asymmetric Narrow Ramp AR 2	0.88

### **5.5.2 Mean Flow Data Based Evaluations**

Figures 5.71 and 5.72 are plots of the two primary quantitative measures derived from the Mach contour plots: average plume area and average plume centroid. A detailed analysis by PME ramp of each quantity can be found in the previous sections of Chapter Five.

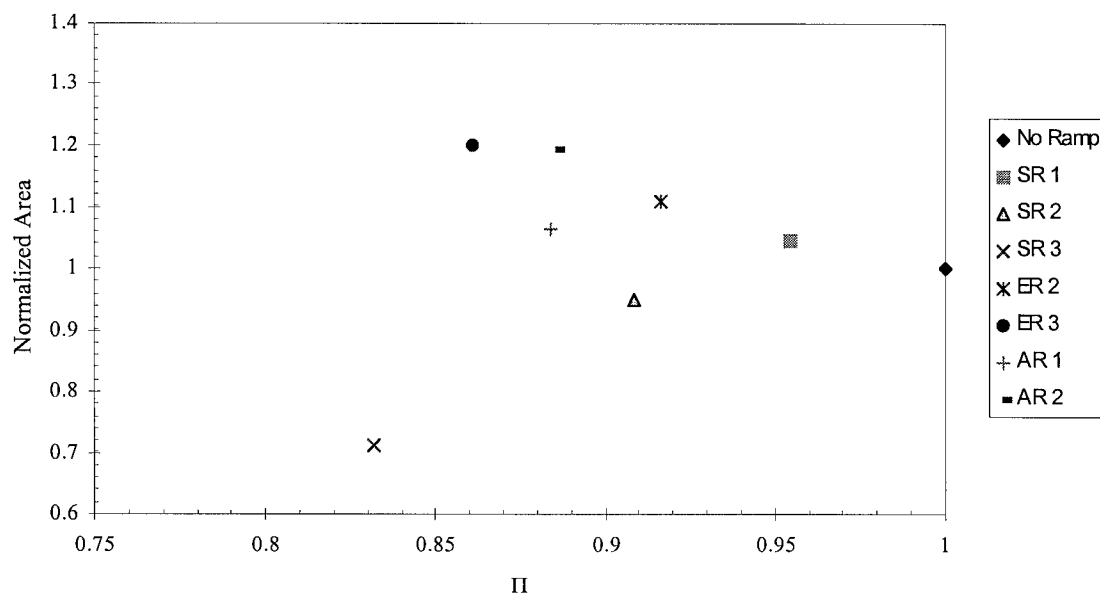


Figure 5.71: Normalized Average Plume Area vs.  $\Pi$

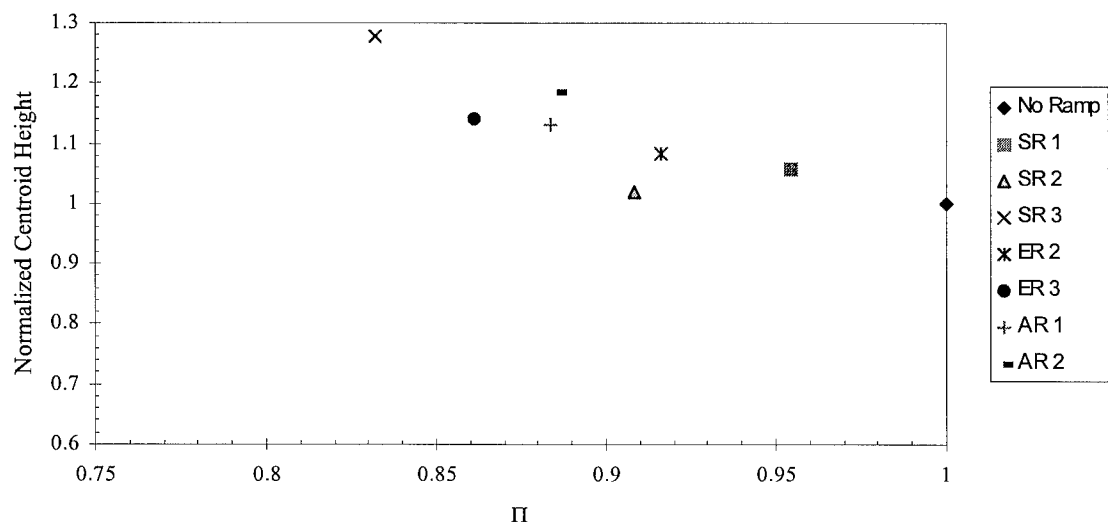


Figure 5.72: Normalized Average Plume Centroid vs.  $\Pi$

In Figure 5.71, the average plume areas as measured by Mach contours are plotted against  $\Pi$ . In this figure as well as the three following, all results are normalized with the simple transverse injection results. With the exception of the double ramp SR 3, there is a declining trend in  $\Pi$  as the area is

increased. This is logical, since large plume mixing structures will result in regions of relatively high pressure loss. However, two ramps perform worse in measured average plume area than the simple transverse injection, the double cone ramp SR 2 and the double ramp SR 3. Both of these ramps generate an expansion that has a detrimental effect on vortex strength. In contrast, the wide ramp AR 1, narrow ramp AR 2 and truncated extended ramp ER 2 also produce a vortex reducing expansion, but this is offset by strong vortex enhancement from ramp or extension spillage. Moving across the chart horizontally, the results for ramps SR 3, SR 2, SR 1, AR 1, ER 2, AR 2 and ER 3 can be seen in order of increasing plume area. This order of the ramps is also the order for decreasing expansion strength, with ramp SR 3 having the most focused expansion in the cross sectional plane of the plume. Ramp ER 3, which should not have any appreciable expansion across the plume, has the highest average plume area. In comparison, Ramp ER 2 has an expansion across the ramp rear face which results in an 8% area reduction from ramp ER 3. Therefore, an expansion has been demonstrated to adversely affect vortex structures. The 8% increase in plume structure area of ER 3 over ER 2 was incurred at a 6% total pressure loss penalty due to the sharp convergence of the tapered extended model.

In Figure 5.72, the normalized average centroids of the plumes are plotted against  $\Pi$ . An interesting result is the double ramp, SR 3, has a significantly greater penetration than all other configurations. This appears to be a product of the two-dimensional frontal aspect of the double ramp, which effectively blocks the flow from turning back towards the tunnel ceiling. Aside from the unique results for the double ramp SR 3, a general trend observed for Figure 5.71 is repeated. Those ramps with weaker expansion generating geometries penetrate further than similar geometries that produce strong expansions. An example can be seen between ramp ER 2 and ER 3, AR 1 and AR 2, and SR 1 and SR 2. Ramps ER 2, AR 1 and SR 1 produce greater expansions than the similar geometries of ramps ER 3, AR 2 and SR 2. Another interesting feature to note is the extended ramp group does not improve penetration over the asymmetric ramp group. This result indicates that the main enhancement to penetration occurs on the ramp compression face, and that the extension does not enhance penetration. Further evidence to support this conclusion comes from the Mach contour plots for the extended ramps, Figures 5.47 and

5.49. In both cases, the trailing profile of the extension (i. e., the truncated or tapered rear of the ramp) is clearly reflected in the plume. Figure 5.47, the Mach contour plot for the truncated extended ramp ER 2, has a wide, nearly rectangular separation between the vertically elongated vortex cores. This separation, as well as the vortex degrading rear edge expansion of the truncated ramp, could have impeded the convective interaction between the counter rotating vortex pair and lead to lesser penetration than the tapered configuration, ER 3. Figure 5.49, the Mach contour plot for the tapered extended ramp has closely packed elongated vortex cores with tapered contour separation. The closely packed vortex pair was able to interact and convect into the freestream to a similar depth of the asymmetric ramps.

### 5.5.3 Digital Image Data Based Evaluations

Figures 5.73 and 5.74 are plots of the two primary quantitative measures derived from the parallel oriented time-averaged laser images: the plume initial trajectory and centerline decay rate. A detailed analysis by PME ramp of each quantity can be found in the previous sections of Chapter Five.

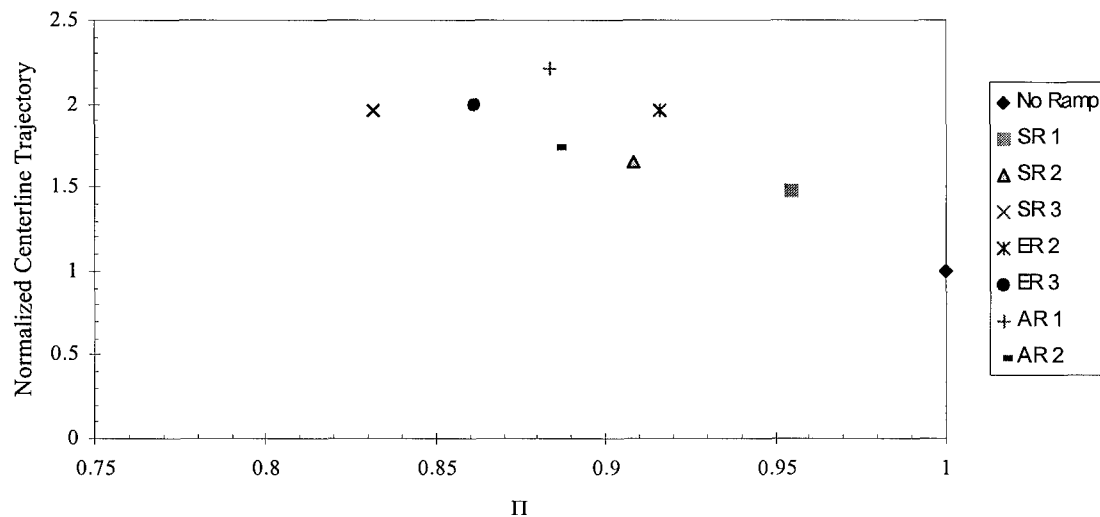


Figure 5.73: Normalized Average Plume Centerline Trajectory vs. II

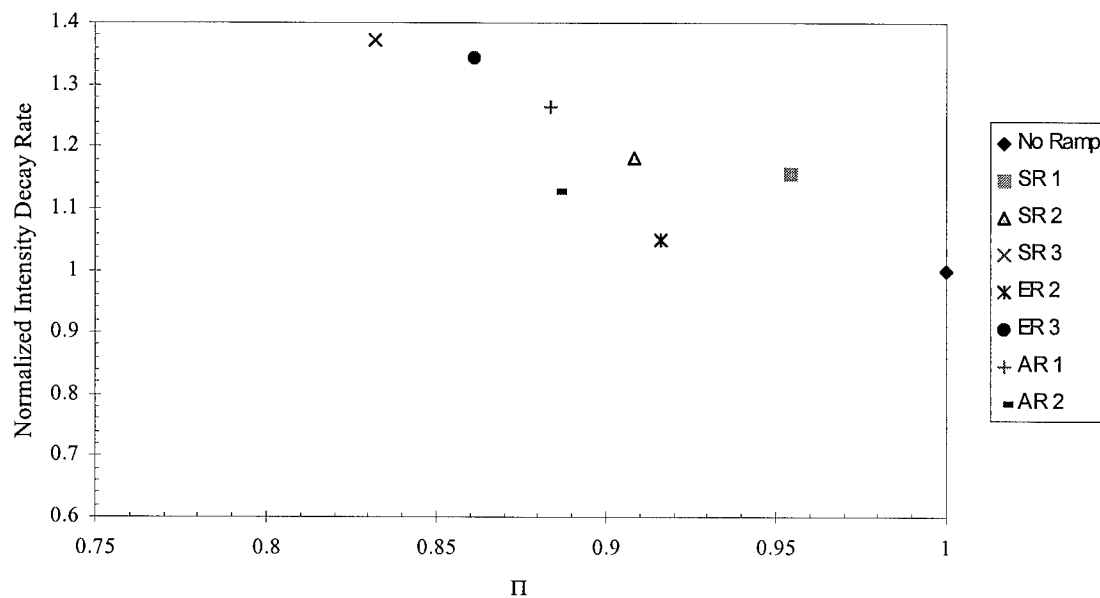


Figure 5.74: Normalized Average Plume Intensity Decay Rate vs.  $\Pi$

Figure 5.73 is a plot of the normalized plume centerline initial trajectory, or the slope of the first eight data points correlating to the length of the ramp compression surface, vs.  $\Pi$ . In all PME ramp cases, an appreciable gain in initial plume trajectory is achieved over the simple transverse injection. Another general trend is that the broader the ramp face, the better the initial penetration. The double diamond ramp SR 1 and double cone ramp SR 2 both present the narrowest frontal profile to the oncoming plume, which results in less surface for plume interaction to occur. In the region where the plume is observed to lift-off of the ramp compression faces, vorticity is still developing from the freestream impacting the plume stream tube. Whether enough vorticity is created to generate a magnus effect lift-off, or the plume simply impinges on and reflects from the ramp compression face is indeterminate. Support for a magnus effect lift-off comes from the widest profile ramp, the double ramp SR 3. Flow passing around the injectant plume is obstructed by the broad compression face of the double ramp, which may reduce the amount of spin imparted by shear on the plume. If less spin is initially imparted on the plume, less of a magnus effect would be initially observed. Overall, the symmetric ramp group shows a nearly linear trend between initial plume centerline trajectory and  $\Pi$ . As the symmetric ramp compression faces are progressively enlarged, the initial trajectory as well as total pressure loss increase. Another feature of

interest in Figure 5.73 is the difference between the wide ramp AR 1 and the narrow ramp AR 2. Here the trend of a broader face increasing the initial trajectory is followed, but there is no attendant total pressure loss.

Figure 5.74 is a plot of the normalized average digital image intensity decay vs  $\Pi$ . This plot shows a negative trend of increasing pressure loss with increasing intensity decay rate. One exception is ramp ER 2, the truncated extended ramp, which has a low decay rate relative to the other PME ramps. This lower centerline decay rate is most likely a result of the vortex cores for the truncated ramp being split apart by the ramp trailing edge, which weakens the vortex pair centerline interactions and mixing effect. Overall, this plot shows considerable scatter, which may be due to an inappropriate choice of scaling factor. The image intensity can also be impacted by factors such as the quantity of seed injected, PME ramp surfaces flows extracting seed from the measured portion of the plume image or seed particles collecting on the tunnel glass sides, obscuring and diffusing the image.

## ***VI. Conclusions and Recommendations***

This chapter outlines the primary conclusions drawn from the analysis of Chapter Five. The optimum geometric configurations based upon a set of design criteria are presented. Recommendations for further study are submitted.

### ***6.1 Conclusions***

As previously stated, the primary objectives of this investigation were to enhance the penetration and mixing of an injected gaseous jet into a supersonic freestream without adversely impacting total pressure losses. The measures developed in conducting this investigation have a clear trend: increases to any of the mixing and penetration parameters over simple transverse injection will result in a relative total pressure loss.

In general the summary plots (Figures 5.71 through 5.74) show fair agreement with expected trends. The results for comparable geometries, such as simple asymmetric ramps and extended ramps are coherent enough to draw reasonable conclusions about the nature of the flow and plume dynamics. Overall, there is considerable scatter amongst the PME ramp results (the highest least squares regression correlation for any of the plots was below 0.30). This is to be expected, though, considering the spectrum of geometric features tested and the range of expected results. However, for specific geometric features and effects, such as expansion creating geometries, the results correlate well between the similar models.

In conclusion, the best gains in penetration and mixing enhancement as defined throughout this study with the relative least total pressure detriment are achieved by the swept sided ramps with the greatest side sweep. The two ramps that have this geometry are PME ramps ER 3 and AR 2. The tapered extended ramp ER 3 and narrow ramp AR 2 have the best increases in the penetration and mixing parameters considered. Both ramps incur a total pressure loss in the 10 to 15% range, but both produce 15 to 20% gains in plume structure area and centroid penetration. The effect of the ramp extension appears to be negligible; most likely because the ramp extensions are either too low or too narrow for the plume to interact with. The frontal aspect of the ramp is crucial for its effect on the plume as seen with the double ramp SR 3, but also for the impact on total pressure loss. Finally, the total pressure loss incurred by the PME ramp rear surface can be substantial, as observed in the 6% greater total pressure loss from the truncated extended ramp ER 2 to the tapered extended ramp ER 3.



## 6.2 Recommendations

Results have been established which clearly indicate the potential of transverse injection over a ramp. The next step in conducting this experiment is to further explore the geometric features shown to enhance penetration, i. e., swept ramps with high degrees of sweep. Another consideration is to further examine the PME ramps that occupy both ends of the performance spectrum simultaneously, such as the double ramp, SR 3. Along a similar vein, the relative gains in penetration and mixing must be weighed against the total pressure loss purely from a combustion standpoint to establish whether any of these configurations are usable or produce an unacceptable detriment to thrust production.

The methods used in this investigation provide a complete picture of the flow structures. The mean flow data presents an excellent means of capturing the relative size and strength of the injection flow field. The laser imagery captured in this investigation also provides flow visualization from which to interpret the mean flow data. There are three routes, however, to enhance future exploration.

First, hot wire or hot film anemometer has been used to directly measure the strength of vorticity<sup>20,22,26</sup> and turbulent properties, both essential for any successful mixing scheme. Though the results observed correlate well with the various techniques employed in this experiment, direct measurement of vortex strength is required to ensure the flow has been properly characterized. For example, the single vortex core observed in the Mach contour plots for the double cone ramp SR 2 and double ramp SR 3, Figures 5.24 and 5.26, may still have vestiges of the twin vortices that mean flow probes can not resolve. Hot wire anemometry presents a means to directly measure cause and effect relations on vorticity.

Second, plume concentration data is required to measure the near field mixing enhancements directly. Correlations exist between mixing and the flow structures observed in the Mach contour plots and flow visualization. However, some of the flow structures have contradictory effects, such as shocks inducing baroclinic torque to enhance vorticity and expansions weakening vorticity. In order to determine the absolute effects of the flow structures, as opposed to the relative effects observed here, concentration data can provide the final assessment of mixing enhancement. The difficulty with such measurements now is that AFIT resources currently do not include concentration measurement equipment, though this is not an insurmountable problem. A relatively simple modification to the injector gas supply would enable

helium injection for binary gas mixtures. The majority of the hardware for concentration measurements is easily fabricated or obtained. Future efforts in injection should be aimed toward developing concentration measuring capabilities.

Third, the data collected has unused potential. Specifically, the planar laser images were acquired using a particle imaging velocimeter (PIV) setup. Since both red and green laser sheet information are in each of the parallel oriented images, the image data could be resolved into local velocity vector fields. Once a mean flow velocity in the plume is established the rotation rate of the plume vortices would be a function of the frequency between vortex helix peaks, similar to measuring frequency from a sine wave output. PIV measurements would allow direct non-intrusive velocity and vorticity measurements in a plane at any downstream location. An examination of the relative differences by downstream location could determine the full development of ramp geometry flow effects.

A final recommendation for future research is to continue using the techniques employed in this investigation. A fairly broad assortment of geometries have been tested and preliminary evaluations of geometric features that enhance and hurt penetration and mixing made. Future research can be focused on broadening the basic understanding of such complex flow fields. Once a suitable base of knowledge exists, refinement of the designs can lead to an optimum configuration.

## Appendix A: Total Pressure Contour Plots

These figures are the total pressure ratio contour plots generated during the course of the investigation. As should be expected, the contour profiles closely match those of the Mach contour plots in Chapter Five. The final contour plot in this series is that of the wind tunnel cross section with neither injection nor PME ramps in the flow.

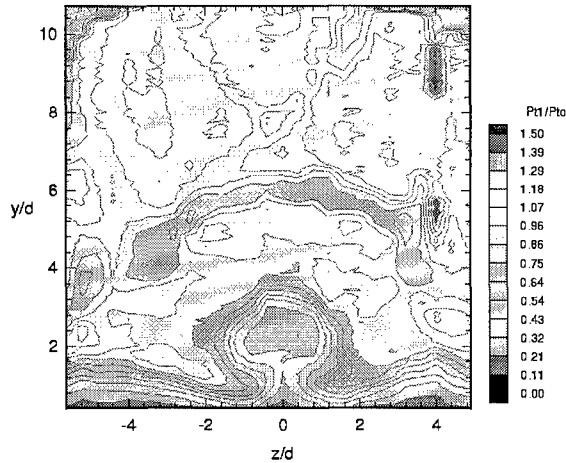


Figure A.1: Simple Transverse Injection

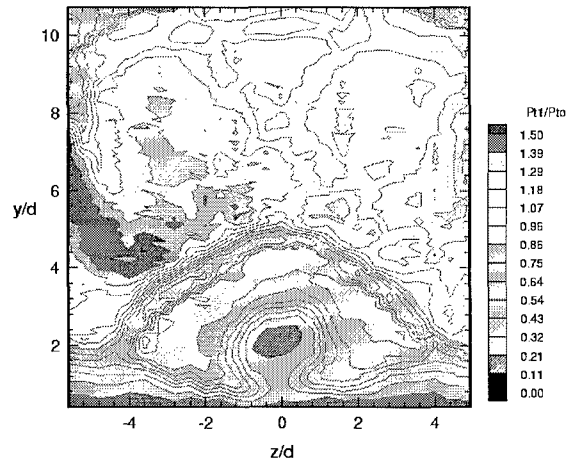


Figure A.3: Double Cone Ramp SR 2

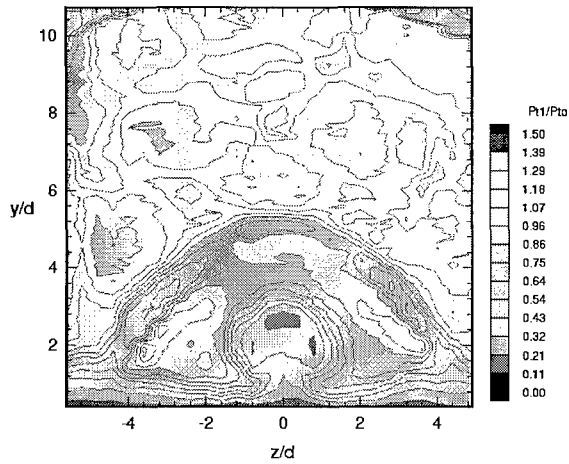


Figure A.2: Double Diamond Ramp SR 1

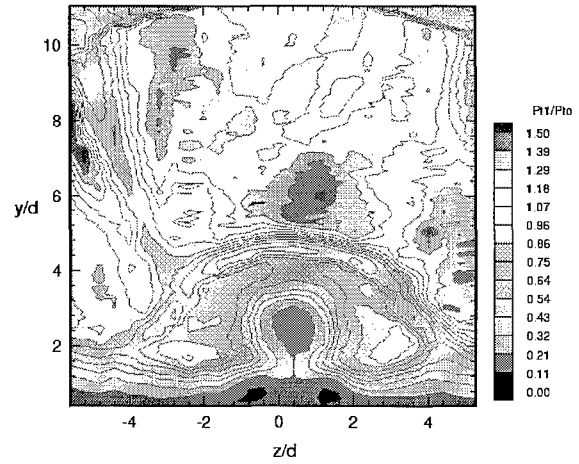


Figure A.4: Double Ramp SR 3

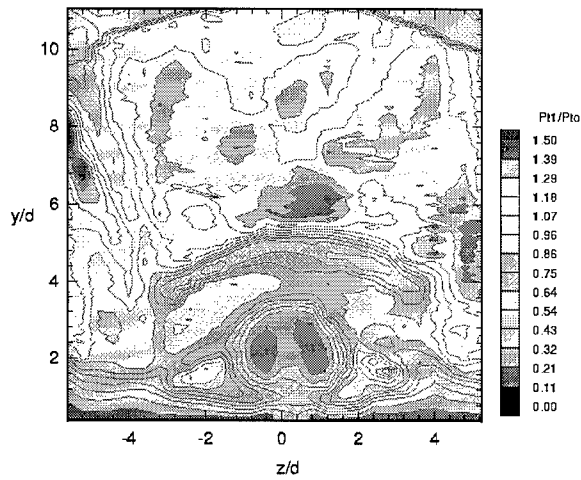


Figure A.5: Truncated Extended Ramp ER 2

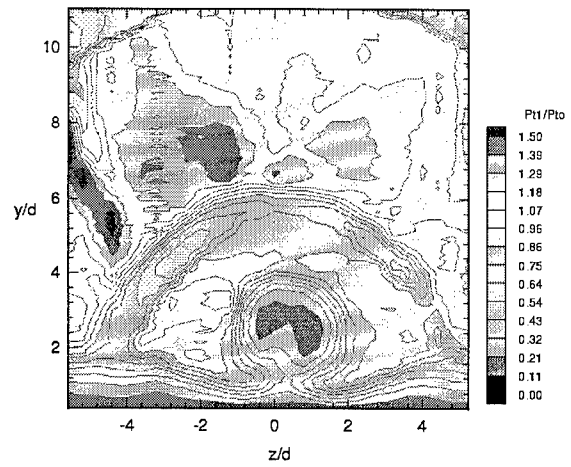


Figure A.8: Narrow Ramp AR 2

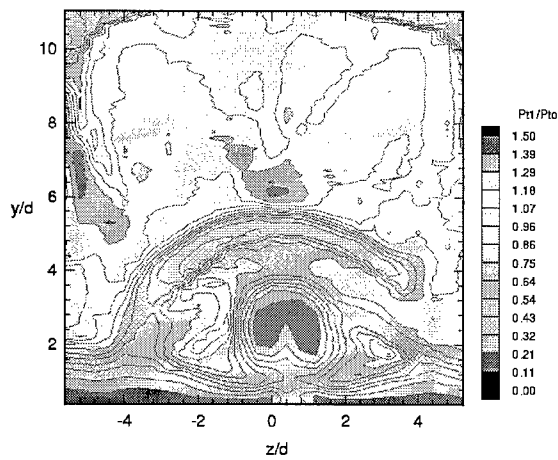


Figure A.6: Tapered Extended Ramp ER 3

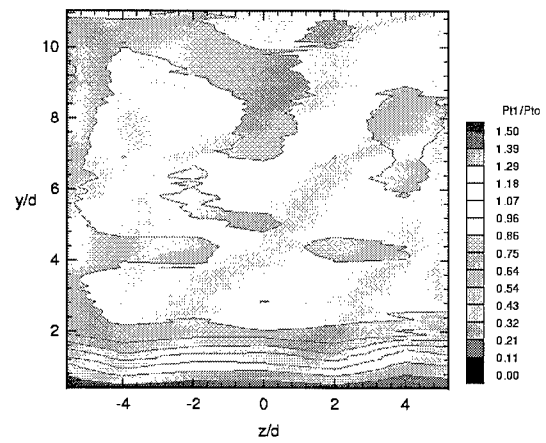


Figure A.9: Test Section, No Injection or PME Ramp

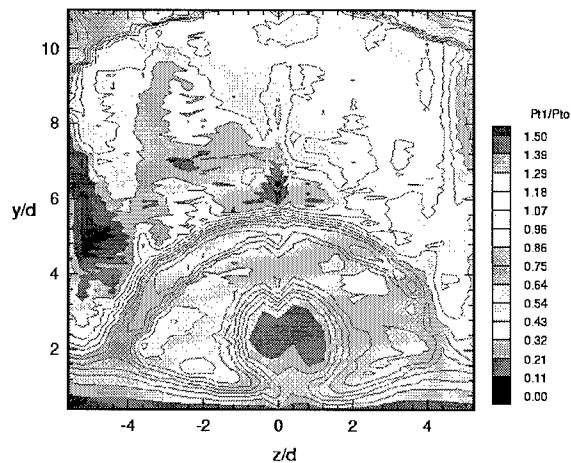


Figure A.7: Wide Ramp AR 1

### Appendix B: Instantaneous Cross Flow Oriented Images

These figures are the cross flow oriented instantaneous images. In general, the level of detail and resolution of these images suffers from the off-centerline angle these images were acquired at. The time averaged images did not suffer this resolution problem, being blurred anyway.

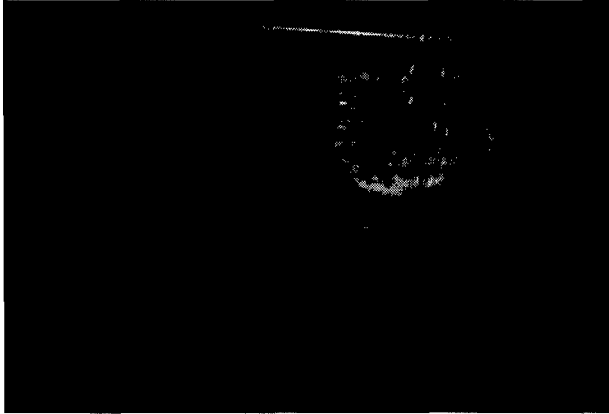


Figure B.1: Simple Transverse Injection

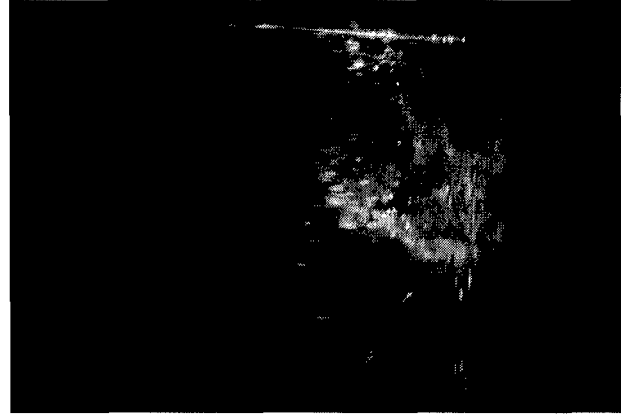


Figure B.4: Double Ramp SR 3

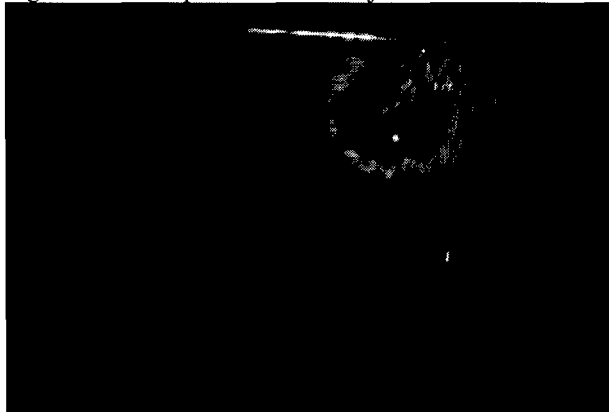


Figure B.2: Double Diamond Ramp SR 1



Figure B.5: Extended Diamond Ramp ER 1



Figure B.3: Double Cone Ramp SR 2

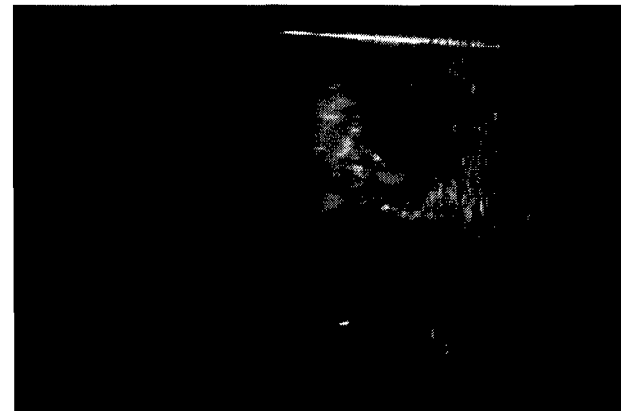


Figure B.6: Truncated Extended Ramp ER 2

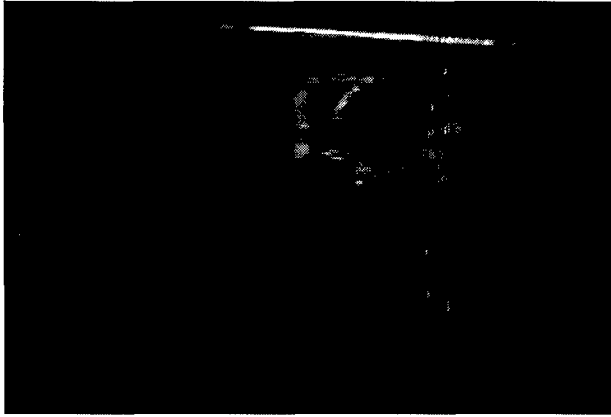


Figure B.7: Tapered Extended Ramp ER 3

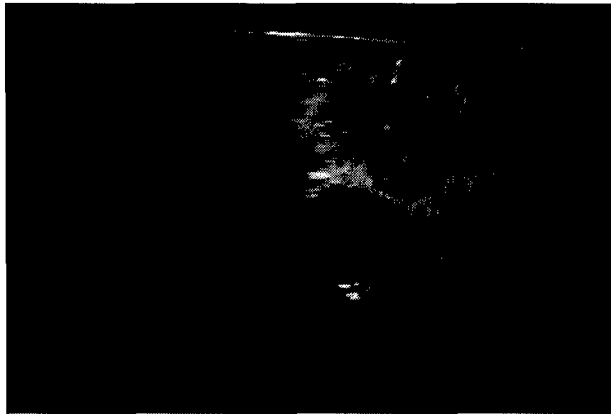


Figure B.7: Wide Ramp AR 1

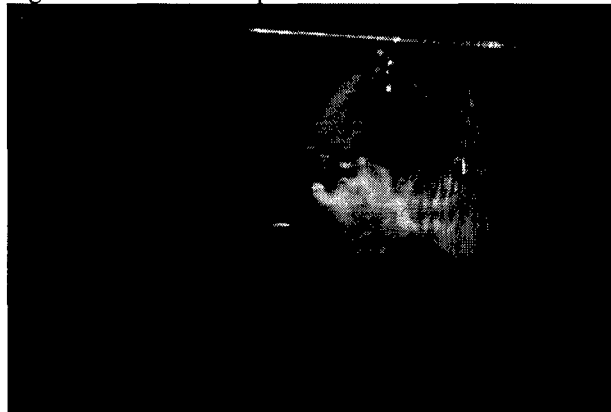


Figure B.9: Narrow Ramp AR 2

## Appendix C: Uncertainty Analysis

Several types of uncertainty are present in this investigation. This appendix details the sources of uncertainty, estimates the potential effect of uncertainty present in the investigation on the experimental results.

### ***C.1 Position Uncertainty***

The measurements conducted in this experiment were made in two dimensions. In the horizontal direction, the mean flow data was collected across 4.60 cm of the  $z$  axis divided into 29 stations separated by 0.16423 cm. A steel ruler was mounted to the mean flow probe holder, which was used to position the mean flow probes at the correct  $z$  axis location relative to a fixed mark on the tunnel floor. The ruler was graduated into 0.07938 cm divisions. A maximum misalignment of  $1/2$  of the axial station separation distance would be possible based upon the ruler graduation. This translates into a maximum  $z$  axis position uncertainty of  $\pm 0.2 d$ .

For each  $z$  axis station, a probe sweep of 5.08 cm of the tunnel cross section was made by the traverse system. The vertical position of the probe was tracked by the LVDT system described in section 3.5.2. The position indicated by the LVDT voltage had a recorded variance of  $\pm 0.13\%$ . This error is two orders of magnitude lower than the horizontal position error, and is considered insignificant.

Position uncertainty of the digital images is considered insignificant as well. The resolution of the images resulted in a pixel grid of 28.6 pixels per cm. Converting to  $d$  scaling this results in 11.4 pixels per  $d$ . The maximum error in position from a one pixel misalignment therefor is  $\pm 0.8 d$ . However, all images were processed with exactly the same station spacing, so the relative uncertainty between images is zero.

### ***C.4 Data Uncertainty***

The mean flow data acquired has two associated uncertainties, related to gain uncertainty and gain stability across the measurement range. The gain uncertainty was 0.5% and the stability uncertainty was 0.2%. Including digital conversion effects, Huffman<sup>27</sup> found the overall pressure uncertainty was 0.54%. McCann<sup>26</sup> found the Mach number error for similar measurements to be 0.2, or 7%.

### ***C.4 Calculated Uncertainty***

Table C.1 summarizes the uncertainties of the various assumed or acquired properties

TABLE C.1  
UNCERTAINTIES IN CALCULATIONS

Property	Uncertainty	Equations	Figures
Mach Number	7%	4.5	5.6, 5.7, 5.22-5.27, 5.46-5.50, 5.63-5.66, 6.1, 6.2
Pressure	0.54%	4.1, 4.6	6.1-6.4, A.1-A.9
z Position	0.2d		5.6, 5.7, 5.22-5.27, 5.46-5.50, 5.63-5.66, 6.1, 6.2, A.1-A.9
y Position	0.13%	4.7	5.6, 5.7, 5.22-5.27, 5.46-5.50, 5.63-5.66, 6.1, 6.2
Pixel Position	0.8 d		5.8, 5.9, 5.28-5.33, 5.51-5.54, 5.67-5.70, 6.3, 6.4



### Bibliography

1. Anderson, John D. Jr., Hypersonic and High Temperature Gas Dynamics, McGraw-Hill, Inc., New York, 1989.
2. Heiser, W. H., and D. T. Pratt, Hypersonic Airbreathing Propulsion, American Institute of Aeronautics and Astronautics, Washington, DC, 1994.
3. Billig, F. S., R. C. Orth, and M. Lasky, "A Unified Analysis of Gaseous Jet Penetration", *AIAA Journal*, Vol. 9, No. 6, June 1971, 1048-1057.
4. Schetz J. A. and F. S. Billig, "Penetration of Gaseous Jets Injected into a Supersonic Stream", *Journal of Spacecraft and Rockets*, Vol. 3, No. 11, November 1966, 1658-1665.
5. Hollo, S. D., J. C. McDaniel and R. J. Harfield, "Quantitative Investigation of Compressible Mixing: Staged Transverse Injection into Mach 2 Flow", *AIAA Journal*, Vol. 32, No. 3, March 1994, 528-534.
6. Waitz, Ian A., F. E. Marble and E.E. Zukoski, "Investigation of a Contoured Wall Injector for Hypervelocity Mixing Augmentation", *AIAA Journal*, Vol. 31, No. 6, June 1993, 1014-1021.
7. Schetz, J. A., R. H. Thomas, and F. S. Billig, Mixing of Transverse Jets and Wall Jets in Supersonic Flow, Springer-Verlag, Berlin, 1991.
8. Ramakrishnan, R. and D. J. Singh, "Modeling Scramjet Combustor Flowfields with a Grid Adaptation Scheme", *AIAA Journal*, Vol. 32, No. 5, May 1994, pp. 930-935.
9. Grasso, F., and V. Magi, "Simulation of Transverse Gas Injection in Turbulent Supersonic Air Flows", *AIAA Journal*, Vol. 33, No. 1, January 1995, pp. 56-62.
10. Riggins, D. W., and P. H. Vitt, "Vortex Generation and mixing in Three-dimensional Supersonic Combustors", *Journal of Propulsion and Power*, Vol. 11, No.3, May-June 1995, pp. 419-425.
11. Harfield, R. J. Jr., S. D. Hollo, J. C. McDaniel, "Experimental Investigation of a Supersonic Swept Ramp Injector Using Laser-Induced Iodine Fluorescence", *Journal of Propulsion and Power*, Vol. 10, No. 1, Jan- Feb 1994, 129-135.
12. Donohue, J. M., J. C. McDaniel Jr., and Hossein Haj-Hariri, "Experimental and Numerical Study of Swept Ramp Injection into a Supersonic Flowfield", *AIAA Journal*, Vol. 32, No. 9, September 1994, pp. 1860-1867.
13. Fuller, R. P., P.-K. Wu, A.S. Nejad, and J. A. Schetz, "Fuel-Vortex Interaction for Enhanced Mixing in Supersonic Flow", *AIAA 96-2661*, 1996, .
14. Donohue, J. M. and J. C. McDaniel Jr., "Complete Three-Dimensional Multiparameter Mapping of a Supersonic Ramp Fuel Injector Flowfield", *AIAA Journal*, Vol. 34, No. 3, March 1996, pp. 455-462.
15. Cary, A. M., Jr. and J. N. Hefner, "Film Cooling Effectiveness in Hypersonic Turbulent Flow", *AIAA Journal*, Vol. 8, No. 11, November 1970, 2090-2091.
16. Northam, G. B., I. Greenberg, C. S. Byington and D. P. Capriotti, "Evaluation of Parallel Configurations for Mach 2 Combustion", *Journal of Propulsion and Power*, Vol. 8, No. 2, March-April 1992, 491-498.

17. Ahuja, J. K., S. N. Tiwari, and D.J. Singh, "Hypersonic Shock-Induced Combustion in a Hydrogen-Air System", *AIAA Journal*, Vol. 33, No. 1, January 1995, pp. 173-176.
18. Schetz, J. A., R. H. Thomas, and F. S. Billig, Mixing of Transverse Jets and Wall Jets in Supersonic Flow, Springer-Verlag, Berlin, 1991.
19. Billig, F. S., and J.A Schetz, "Penetration and Mixing of Gas Jets in Supersonic Cross flow", *AIAA Journal*, Vol. 32, No. 7, July 1994, pp. 1533-1535.
20. Bowersox, R. D. W., "Turbulent Flow Structure Characterization of Angled Transverse Injection into a Supersonic Cross Flow", *Journal of Spacecraft and Rockets*, In Print.
21. Riggins, D. W., C.R. McClinton, R. C. Rogers, and R. D. Bittner, "Investigation of Scramjet Injection Strategies for High Mach Number Flows", *Journal of Propulsion and Power*, Vol. 11, No. 3, May-June
22. McCann, G. J., and R. D. W. Bowersox, "Experimental Investigation of Supersonic Gaseous Injection into a Supersonic Freestream", *AIAA Journal*, Vol. 34, No. 2, February 1996, pp. 317-323.
23. Brescianini, C. P., and R. G. Morgan, "Numerical Modeling of Wall-Injected Scramjet Experiments", *Journal of Propulsion and Power*, Vol. 9, No. 2, March-April 1993, pp. 169-174.
24. Gerlinger, P., J. Algermissen, and D. Brüggemann, "Numerical Simulation of Mixing for Turbulent Slot Injection", *AIAA Journal*, Vol. 34, No. 1, January 1996, pp. 73-78.
25. Billig, F. and J. A. Schetz, "Analysis of Penetration and Mixing of Gas Jets in Supersonic Cross Flow", *AIAA Fourth International Aerospace Planes Conference, AIAA Paper AIAA-92-506*, December 1992, 1-10.
26. McCann, G. J., Compressible Turbulence Measurements in Low Angle Injection Into Supersonic Flow, AFIT/GAE/ENY95M-03, School of Engineering, Air Force Institute of Technology (AU), Wright-Patterson AFB OH, March 1995, 1995.
27. Huffman, R. AFIT MACH 2.9 Manual, 1995.
28. Anderson, John D., Fundamentals of Aerodynamics, McGraw-Hill, New York, 1984.
29. Bowersox, R. D. W., Compressible Turbulence in a High-Speed High-Reynolds Number Mixing Layer, PhD dissertation, Virginia Polytechnic Institute and State University, Department of Aerospace Engineering, Blacksburg, VA, 1992.
30. Liepmann, H.W. and A Roshko, Elements of Gasdynamics, John Wiley & Sons, New York, 1957.
31. Amtec, Tecplot Version 6 User's Manual, Amtec Engineering Inc., Bellevue, Wa, 1994.

Vita

Capt Mark P. Wilson was born [REDACTED] 1966 in [REDACTED] to [REDACTED] and [REDACTED]. He graduated from Monmouth Academy in the spring of 1986, and enrolled in the Aeronautical Engineering program of Embry-Riddle Aeronautical University under a four year ROTC scholarship. He was commissioned and graduated Cum Laude with a Bachelor of Science degree in Aeronautical Engineering in April of 1990.

Capt Wilson's first assignment was to the United States Air Force Academy, Colorado Springs Colorado, as a Manpower Officer. He entered the engineering career field in April of 1993 by accepting an operational test and evaluation reliability and maintainability assignment with the B-2 Spirit Combined Task Force, Edwards Air Force Base, California. In May of 1995 Capt Wilson entered the School of Engineering, Air Force Institute of Technology.

[REDACTED]  
[REDACTED] North Monmouth, Mo 64266